Fabrication and Measurement of a Niobium Persistent Current Qubit

by

Daniel Yuki Nakada

Submitted to the Department of Electrical Engineering and Computer Science
in partial fulfillment of the requirements for the degree of

Doctor of Philosophy in Electrical Engineering

at the

MASSACHUSETTS INSTITUTE OF TECHNOLOGY

June 2004

Author .....
Department of Electrical Engineering and Computer Science
May 20, 2004

Certified by .....
Terry P. Orlando
Professor of Electrical Engineering
Thesis Supervisor

Accepted by .....
Arthur C. Smith
Chairman, Department Committee on Graduate Students

Fabrication and Measurement of a Niobium Persistent Current Qubit

by

Daniel Yuki Nakada

Submitted to the Department of Electrical Engineering and Computer Science
on May 20, 2004, in partial fulfillment of the
requirements for the degree of
Doctor of Philosophy in Electrical Engineering

Abstract

Recent successes with superconducting Josephson junction qubits make them prime candidates for the implementation of quantum computing. This doctoral thesis details the study of a niobium Josephson junction circuit for quantum computing applications. The thesis covers two main areas: 1) the fabrication of sub-micron niobium Josephson junction devices using a Nb/Al/AlO_x/Nb trilayer process and 2) measurements of unique quantum properties of a superconducting device proposed as a quantum bit - the Persistent Current (PC) qubit. The thesis discusses the fabrication of niobium Josephson junction devices which is integral to the design and measurement of the circuit. The devices were fabricated at MIT Lincoln Laboratory using optical projection lithography to define features. A technique to produce more uniform critical-current densities across a wafer is developed within the scope of the thesis. We also introduce experimental work on the PC qubit performed at dilution refrigerator temperatures ($T \simeq 12\,mK$). Microwave spectroscopy was used to map the energy level separation between macroscopic quantum states of the qubit system. We measured the intrawell energy relaxation time τ_d between quantum levels in this particular device. The intrawell relaxation measurements are important in determining whether a promising decoherence time can be achieved in Nb-based Josephson devices, which has a more mature fabrication process compared to other superconducting fabrication processes.

Thesis Supervisor: Terry P. Orlando
Title: Professor of Electrical Engineering

Acknowledgments

My doctoral thesis derived from the collective guidance and contribution of many people. I've been fortunate to work with professors, postdocs, graduate students, technicians, and undergraduates who have educated, stimulated, pushed and supported me during my time at MIT. As a graduate student, I grew both academically and personally and I am grateful to have had such a challenging experience.

I would like to first thank my research advisor Prof. Terry P. Orlando for the opportunity to be a part of his research group. He is truly a generous advisor and educator. I've gained a tremendous amount from his deep understanding of solid state physics, particularly superconducting Josephson junction devices. I value his kind nature and positive attitude that he has provided within the research group as well as in the MIT graduate community. My experience in his group has providing me with a lasting education in academic research and beyond.

Prof. Karl K. Berggren has been a second advisor to me in my graduate career. During my first few years in the group he mentored me in the superconductive fabrication process at MIT Lincoln Laboratory. Most importantly, I learned from him the value of solid organization (although the usual state of my desk would say otherwise) and careful attention to detail. I hope I've adapted his critical thinking approach and analytical ways.

I thank Prof. Henry I. Smith for being on my doctoral committee as well as for being my academic advisor. I appreciate his time in discussing the Josephson Junction fabrication process with me and providing feedback on my presentations and reports.

MIT Lincoln Laboratory has been a stimulating environment for me to work in and I'm honored to have gained a valuable experience at a distinguished government research laboratory. In particular, I would like to acknowledge the Analog Device Technology group (Group 86). I always felt welcome to participate in their group meetings and discussions. To Dr. William D. Oliver, I owe many thanks. I've gained tremendous insight from his intuitive knowledge and laboratory experience. I've ad-

mired his strength and vision to pursue difficult experimental challenges and his advice in research (and many other things) will never be forgotten. I would like to thank Dr. Jay Sage. I greatly appreciate his input and suggestions on the design layouts. I thank Terence J. Weir for his help in my understanding of experimental cryogenics and low temperature measurements of Josephson junctions. I enjoyed his stories of fishing, bluegrass music, cooking, and Ireland. His humor and friendly disposition made the low T_c lab a great place to work. The fabrication of junctions could not be possible without the dedication and hard work of Earle Macedo. I appreciate his enormous patience in training me (sorry about the wafer I broke) and helping me to understand the fabrication process, most notably the trilayer deposition and plasmatherm. I'm still amazed at how many cups of coffee he drinks per day. Through the work of Richard Slattery, I've learned of the complexities of the microwave packaging. His advice and suggestions made me carefully think through a proper design. I'm also grateful for his work on the TEM images. I'd also like acknowledge Dan Baker for his discussions of the trilayer formation and liftoff process. I've appreciated the help of George Fitch for his help with computer software. I thank Dr. Vladimir Liberman for work on obtaining the optical constant values for the Nb/NbO_x thin films. I'm grateful to Dr. Daniel Oates for discussions on the microwave environment. And I'd like to thank Robert Konieczka for his assistance in the d-lab (I always appreciate the warm hello). I would like to acknowledge the leadership of the group leaders: Mark A. Gouker and Assistant Group Leader Leonard M. Johnson and former Group Leader Gerhard Sollner. And recognition goes to the group secretary Joanne Rantz for assistance in securing clearance forms and other laboratory documents. And of course, I won't forget who helped initiate me into Group 86, Michael O'Hara. I've gained a great amount of insight into the fabrication process and circuit layout from him. A large component of my time at Lincoln Laboratory was spent in the MIT Microelectronics Laboratory (MEL). The fabrication of the Nb devices relies on the combined efforts of many skilled technicians. I would like to especially recognize and thank the following people in the MEL: Cindy Costa, Bruce Wheeler, Al Kaplan, Scott Ladd, and Dolly Shibles.

Throughout graduate school, my education has been mainly shaped by the discussions and collaborations with the postdocs and graduate students at MIT. I'm glad to have been under the guidance and mentorship of previous Orlando research group members. When Prof. Kenneth Segall joined our group as a postdoc, he showed leadership and initiative that is greatly admired. I've had the opportunity to talk with him concerning low-temperature measurements of Josephson junction circuits and his analysis of the thermal activation data were instrumental in moving the research forward. I would like to thank Dr. Donald Crankshaw. His expertise in simulations and low-noise experimental techniques were valuable components of my research. I thank Dr. Lin Tian, who provided me with helpful discussions concerning the theoretical work involved with the PC qubit. I'm glad she could help answer many of the questions I had. I'd like to thank Dr. Enrique Trias for his mentorship and advice. I've enjoyed his quick wit and sense of humor. He will always be the best salsa dancer the group ever produced. I also appreciate my fruitful discussions with Prof. Juan Mazo. I thank Dr. Yang Yu who I learned a tremendous amount about setting up the dilution refrigerator and I enjoyed working with him on the PC qubit spectroscopy/relaxation time experiments. His expertise in Josephson junctions was a valuable asset to the group. Dr. Jonathan Habif has provided me with knowledge on RSFQ circuitry first as a graduate student at Rochester and now as a postdoc in the Orlando group.

I've gained knowledge from both the graduate students who have come before me as well as the graduate students who have come after me. I'm glad that they are not only coworkers but friends and I only hope I have helped them through graduate school as much as they have helped me. I truly thank Bhuwan Singh, my friend and colleague. I will always remember the late night talks in my office or his. I admire his incredible intelligence and unique sense of humor. His giving nature will certainly live on through me as well as many others. My good buddy Janice C. Lee, I am grateful for your enthusiasm and hard work. I've learned a great deal about the microwave aspect of our research and thank you for your assistance with the setup of the microwave cables. I'll never have a better (or sweeter) snack time friend. I

thank David Berns who has made the group a much more enjoyable place to work. I also thank him for providing work in setting up the dilution refrigerator. I am in gratitude to Kota Murali who helped me to better understand quantum computing as well as the dissipation in our PC qubit system. I've also admired his strong conviction and perspective and he will always be the "young genius" in the group. I also thank William Kaminsky for our fruitful discussions. And I thank Bryan Cord for his contribution to the measurement electronics.

Special assistance came from Dr. Maxim Vavilov in Prof. Levitov's group. Through our discussions, I've gained a better understanding of the dynamics of the PC qubit system.

Part of my research involved collaborations with Harvard University, the Delft University of Technology and the University of Rochester. I would like to thank Dr. Sergio Valenzuela and Prof. Nina Markovic for their expertise in the dilution refrigerator measurements at Harvard and Prof. Michael Tinkham for his helpful meetings concerning the qubit system. At Delft University, I would like to thank Prof. Hans Mooij for his intuitive insight into the PC qubit, Prof. Caspar van der Wal for his assistance in our dilution refrigerator unit and stimulating discussions of mesoscopic devices, and Alexander ter Haar for his constructive visit and informative e-mails. From the University of Rochester, I'd like to thank Prof. Mark Bocko and Dr. Marc Feldman for their input.

I'd like to give a special thank you to Lisa L. Huang. Her support and caring nature made graduate school an easier time for me at MIT. I am glad you encouraged me to apply here and I will not forget your courage to carve your own path in life.

And last but certainly not least I'd like to acknowledge the support and love of my family back home in Los Angeles. My father and mother who have always instilled the value of an education. My "favorite" sister Grace who provided strength and encouragement throughout my life. She will always be the toughest one in the family but hopefully through my graduate experience, I have caught up with her just a little bit.

Contents

List of Figures

List of Tables

Chapter 1

Introduction

1.1 Motivation

Presently, there are two fundamental approaches to increase the computational speed of a physical computing system. The traditional approach has been to push microelectronic transistor sizes to smaller and smaller gate length scales. Intel Chairman Gordon Moore predicted shortly after the advent of the integrated circuit that the number of transistors on a chip would double approximately every two years. Since the introduction of "Moore's Law", there have been two constants: predictions that the end of Moore's Law is just around the corner, and the semiconductor industry proving those predictions wrong by producing ever smaller transistors. Next generation Si CMOS (Complementary Metal-Oxide-Semiconductor) n-gate lengths will soon migrate to less than 120 nm. None the less, few would argue that the present astonishing rate of progress in computer speed and power can continue forever without major enhancements in fabrication technology. Multiple revolutionary developments in integrated circuit technology will be needed to maintain the present rate of growth of computational power. The microelectronics industry faces several engineering obstacles as it continues to minimize device dimensions. Most importantly, reducing feature sizes presents an obstacle of a fundamental nature; classical physics can not correctly describe the behavior of a system as device lengths shrink to near atomic scales. At these dimensions, the world of quantum mechanics begins to emerge. The

radical approach to increasing computational speed relies inherently on the principles of quantum mechanics - this unique form of computing is appropriately called quantum computing.

Quantum computing does not accelerate digital computation using quantum effects nor is its computational power connected with the density of qubits. Quantum mechanics allows one to operate with a superposition of states, simultaneously representing many different numbers. The main advantage then of quantum computing is the parallel execution of logic operations using these superposition (entangled) states. At present, quantum computing offers new efficient methods to solve only a select number of computational problems. Classical computers can efficiently solve "easy problems" in polynomial time - the number of steps required to solve these problems are bounded by a polynomial function of the input size. Such easy problems include addition, subtraction, multiplying, word processing, etc. Quantum algorithms offers the ability to solve "hard" problems efficiently such as the factoring of a large number. The most potentially useful quantum algorithms discovered include Shor's algorithm [1] for factorization and Grover's algorithm for a database search [2].

1.2 Overview

1.2.1 Quantum Bit: Two-Level Quantum System

The basic building block of a quantum computer is the quantum bit. The quantum bit or qubit can be described as a two-level quantum system whose state is restricted to being in an arbitrary superposition of two "basis" states [3, 4]. A classical bit can only have states 0 or 1 whereas a qubit can be in any *linear combination* (or superposition) of states 0 and 1 described by the following wavefunction $|\Psi\rangle$:

$$|\Psi\rangle = \alpha|0\rangle + \beta|1\rangle \tag{1.1}$$

The numbers α and β are complex numbers which satisfy the normalization condition:

$$\langle \Psi | \Psi \rangle = |\alpha|^2 + |\beta|^2 = 1 \tag{1.2}$$

It is convenient to introduce two parameters θ and φ defined by,

$$\alpha = \cos \frac{\theta}{2} \tag{1.3}$$

$$\beta = e^{i\varphi} \sin \frac{\theta}{2} \tag{1.4}$$

The parameters θ and φ define a point on a unit three-dimensional Bloch sphere as shown in Fig. 1-1. In our discussion of the qubit, the Bloch sphere representation will be helpful in describing the time evolution of our two-level quantum system.

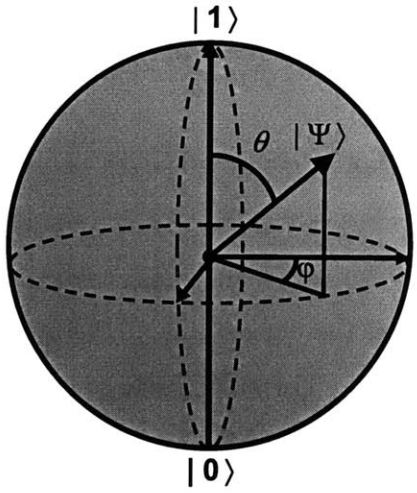

Figure 1-1: Bloch sphere representation of a qubit with state vector $|\Psi\rangle$. Parameters θ and φ define a point on the unit-three-dimensional sphere.

Our two-state system has corresponding eigenenergies E_0 and E_1. The eigenstates $|\Psi_i\rangle$ satisfy the time-independent Hamiltonian of the system described by the time-independent Schrödinger equation

$$H|\Psi_i\rangle = E_i|\Psi_i\rangle \tag{1.5}$$

It is often convenient to represent such a two-level quantum system as a "particle"

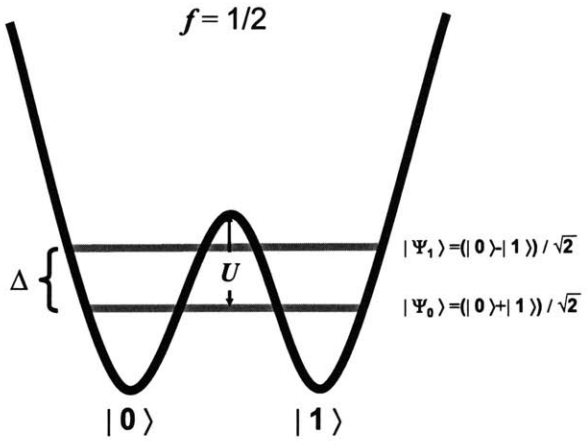

Figure 1-2: The symmetric double well potential configuration at external parameter $f = 1/2$. The eigenstates are then the symmetric and antisymmetric combinations of the single well wavefunctions $|0\rangle$ and $|1\rangle$ with energy difference $E_1 - E_0 = \Delta$.

of spin 1/2, subject to a fictitious "magnetic field" whose direction we conventionally take to define the z axis. For our qubit system, let us consider the double well potential shown in Fig. 1-2. For sufficiently high energy barrier U between wells, the wells are highly localized and the eigenstates of the system correspond to localized states in each well $|0\rangle$ and $|1\rangle$. For sufficiently low barrier U we obtain coupling between the two wells. The two-level system can then be described by a Hamiltonian of the form,

$$\hat{H} = -\frac{1}{2}(\varepsilon\sigma_z + \Delta\sigma_x) \tag{1.6}$$

where the Pauli spin matrices are defined as

$$\sigma_x = \begin{pmatrix} 0 & 1 \\ 1 & 0 \end{pmatrix} \tag{1.7}$$

$$\sigma_y = \begin{pmatrix} 0 & -i \\ i & 0 \end{pmatrix} \tag{1.8}$$

$$\sigma_z = \begin{pmatrix} 1 & 0 \\ 0 & -1 \end{pmatrix} \tag{1.9}$$

and Δ is defined as the matrix element for tunnel coupling between the two wells. The energy $\varepsilon = (f - 1/2)$ is the "detuning" parameter or the difference in the ground state energies of the two wells in the absence of tunnelling. We let f be an external parameter of our system. The eigenvectors of this Hamiltonian $|\Psi_0\rangle$ and $|\Psi_1\rangle$ are then

$$|\Psi_0\rangle = \begin{pmatrix} \cos(\vartheta/2) \\ \sin(\vartheta/2) \end{pmatrix} \tag{1.10}$$

$$|\Psi_1\rangle = \begin{pmatrix} -\sin(\vartheta/2) \\ \cos(\vartheta/2) \end{pmatrix} \tag{1.11}$$

where $\vartheta = \arctan(\Delta/\varepsilon)$. The corresponding eigenenergies $E_{0,1}$ of the system are

$$E_{0,1} = \mp\sqrt{\epsilon^2 + \Delta^2} \tag{1.12}$$

Fig. 1-3 shows the eigenenergies of the system as a function of the external parameter f. If the ratio Δ/ε is small (for $f \ll 1/2$ or $f \gg 1/2$), the eigenstates of H are nearly eigenstates of σ_z, corresponding to states,

$$|\Psi_0\rangle = \begin{pmatrix} 1 \\ 0 \end{pmatrix} \tag{1.13}$$

$$|\Psi_1\rangle = \begin{pmatrix} 0 \\ 1 \end{pmatrix} \tag{1.14}$$

The eigenstates then correspond to the system being localized on either side of the barrier (in the left or right well). At $f = 1/2$, $\Delta/\varepsilon \gg 1$ and the eigenstates of the system are

$$|\Psi_0\rangle = \begin{pmatrix} 1/\sqrt{2} \\ 1/\sqrt{2} \end{pmatrix} \tag{1.15}$$

$$|\Psi_1\rangle = \begin{pmatrix} -1/\sqrt{2} \\ 1/\sqrt{2} \end{pmatrix} \tag{1.16}$$

with corresponding energy splitting $E_1 - E_0 = \Delta$. The eigenstates are then the symmetric and antisymmetric combinations of the single well wavefunctions $|0\rangle$ and $|1\rangle$.

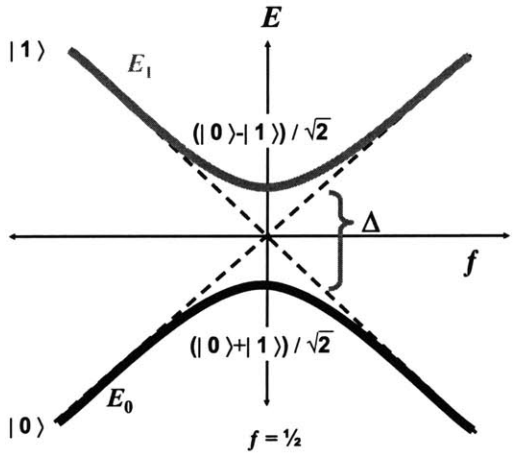

Figure 1-3: The two state quantum system as a function of parameter f. The ground state (black) of the system has energy E_0 and the first excited state (gray) has energy E_1. For zero coupling between the two states, the energy of the two level system is degenerate at $f = 1/2$ (indicated by dashed line). Due to quantum tunnelling, at $f = 1/2$, the eigenstates of the system are the symmetric and antisymmetric superposition of the localized well states with energy difference $E_1 - E_0 = \Delta$.

We next consider the time evolution of our two-state system. Solving the time-dependent Schrödinger equation gives the time evolution of the system

$$i\hbar\frac{\partial}{\partial t}|\Psi(t)\rangle = \hat{H}|\Psi(t)\rangle \tag{1.17}$$

Let us determine the time-dependent state of the system with initial state

$$|\Psi(t=0)\rangle = \alpha_0|0\rangle + \beta_0|1\rangle \tag{1.18}$$

The time dependent state of the system is found to be

$$|\Psi(t)\rangle = \alpha_0 \exp[-\frac{1}{i\hbar}E_0(t-t_0)]|0\rangle + \beta_0 \exp[-\frac{1}{i\hbar}E_1(t-t_0)]|1\rangle \tag{1.19}$$

in our Bloch sphere representation, θ remains constant and the phase φ evolves linearly with time. The state of the system will precess at a constant height (constant θ) within the Bloch sphere at a rate given by the Larmor frequency

$$\omega_{Larmor} = \frac{E_1 - E_0}{\hbar} \tag{1.20}$$

If resonant microwave radiation is applied to the two-level system the state vector will oscillate between the two eigenstates $|0\rangle$ and $|1\rangle$. If the system is initially in the ground state $|\psi(t=0)\rangle = |0\rangle$, the time-dependent transition probability $P_1(t)$ of finding the system completely in the excited state is described by the Rabi formula

$$P_1(t) = \frac{\omega_1^2}{\omega_1^2 + (\Delta\omega)^2} \sin^2(\frac{t}{2}\sqrt{\omega_1^2 + (\Delta\omega)^2}) \tag{1.21}$$

where we define ω_{Rabi} as the Rabi frequency

$$\omega_{Rabi} = \sqrt{\omega_1^2 + (\Delta\omega)^2} \tag{1.22}$$

Here ω_1 is proportional to the amplitude of the microwaves driving the system and $\Delta\omega$ is the frequency difference between the Larmor frequency and the applied radiation. Far from resonance$|\ \Delta\omega\ | \gg |\ \omega_1\ |$, the transition probability is nearly zero. Near resonance, the oscillation amplitude is maximal and the transition probability will oscillate between $|0\rangle$ and $|1\rangle$ with frequency ω_1.

1.3 Physical Systems for Quantum Computing

What system is a feasible candidate for a physical quantum bit? Currently, there is no clear front runner as a viable large scale quantum computing system. A physical quantum computer must at least satisfy the few basic requirements outlined by DiVincenzo [4, 5]: 1) ability to prepare qubits in a desired initial state, 2) coherently manipulate superposition of a qubit's two states, 3) couple qubits together, 4) measure the state of the qubit, and 5) it has to be well isolated from its environment thereby relatively free from interactions that induce noise. Essentially any two-state quantum system that can be addressed, controlled, measured and coupled to its neighbors is a potential quantum computer.

Many of the physical systems considered for quantum computing are of atomic or near-atomic dimensions. Each physical system considered has its inherent advantages and disadvantages. Few macroscopic objects are considered due to the large number of internal degrees of freedom, therefore making it difficult to preserve coherence of the quantum system. A partial list of the physical systems actively considered for quantum computing are:

- Liquid Nuclear Magnetic Resonance (NMR)
- Linear ion-trap
- Cavity QED
- Linear optics with single photons
- Electron spins in quantum dots
- **Josephson junction devices**

One of the greatest technical challenges to be overcome in realizing a quantum computer is the preservation of quantum coherence during the computation process; interaction with any external system or environment destroys this coherence. The major problem in large scale quantum circuits is the interaction of the surrounding

environment with the quantum components, leading to irreversible loss and transfer of information - this process is called decoherence. It is generally accepted that at least 10^4 gate operations must be completed before the effects of decoherence become significant for an error-free quantum computer [6]. This constraint is driving research efforts in Josephson junction devices to increasing the coherence times by investigating the environmental noise on the quantum system. Although the time over which coherence can be maintained is measured to be relatively short ($\sim 100\,\text{ns}$ - $1\,\mu\text{s}$) for such devices, current research in the area shows promise for longer coherence times.

1.3.1 Quantum Computing with Superconductors

Superconducting tunnel junction devices are regarded as one of the most promising approaches for the development of quantum computing [7, 8]. Over the past twenty years, superconducting Josephson junction circuits have exhibited macroscopic quantum phenomena such as Macroscopic Quantum Tunnelling (MQT) [9, 10], energy level quantization [11], and resonant and photon assisted [12] tunnelling between quantum states. Recent successes with superconducting qubits have enhanced the feasibility of implementing quantum computing with Josephson devices. Within the past few years, the observation of a superposition of macroscopic quantum states [13, 14] and time domain coherent oscillations between quantum states [15]-[20] have been reported in such devices. Recently, capacitive coupling of superconducting qubits spaced at large distances ($\sim 0.7\,\text{mm}$) and conditional gate operations have been demonstrated in these devices [21, 22].

The major advantages to using Josephson junction devices as qubits are:

- Relatively easy to measure due to inherent macroscopic quantum nature of superconductivity
- Employ current lithographic technology to fabricate identical qubits
- Scalable to large number of qubits

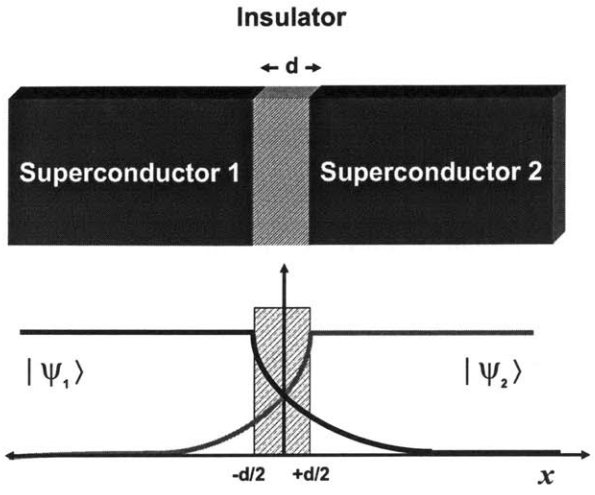

Figure 1-4: Superconducting tunnel junction consists of a thin insulating barrier sandwiched between two superconductors. For sufficiently thin barrier thickness d, the macroscopic wavefunctions $|\psi_1\rangle$ and $|\psi_2\rangle$ of the superconductors interact.

- Ability to combine with on-chip, control electronics (microwave oscillators, Rapid Single Flux Quantum circuitry)

The basic component of all superconducting devices considered for quantum computing is the Josephson junction. The superconducting tunnel junction consists of two superconductors separated by a thin insulating barrier, often a metal-oxide layer (shown in Fig.1-4). With a sufficiently thin ($d \sim 10\,\text{Å}$) barrier, coherent tunnelling of Cooper pairs can occur and the macroscopic wavefunctions of the two superconductors $|\psi_1\rangle$ and $|\psi_2\rangle$ will interact. The devices considered for qubits generally have of order 10^9 Cooper pair electrons whose collective motion produces a relatively large flux ($10^{-3}\Phi_0$ where $\Phi_0 = h/2e$) or voltage ($\sim 1\,\text{mV}$) signals. Indeed, Josephson junctions have been shown to be ideal structures for the observation of macroscopic quantum effects.

Modern lithographic techniques have made submicron and nano-scale size Josephson junctions a reality. The superconducting devices studied were fabricated using a doubly planarized all-refractory technology for superconductive electronics (DPARTS) process at MIT Lincoln Laboratory [23]. The process is used to produce sub-micron

junctions using optical projection lithography using an i-line stepper. Starting with the Nb/Al/AlO_x/Nb trilayer formation, the devices are defined using standard deposition and etching techniques of the various metal and insulating layers. Understanding the fabrication process is vital to knowing limitations on the circuit parameters and more importantly, quantifying possible mechanisms for decoherence or dissipation in these devices.

Superconducting quantum systems may also be scalable up to the minimum number of qubits that would make a real-life quantum computer useful. Each qubit can be individually addressed by conventional techniques of electrical engineering. A wide variety of potential designs and their couplings is available to scale to a large array of qubits. Capacitive and mutual inductive coupling of these devices have already been demonstrated in such devices.

Another major advantage to using Nb Josephson junction technology for quantum computing applications is the ability to integrate classical electronic circuits for qubit control and measurement. Multiple-qubit experiments will ultimately require several rf control signals and DC bias lines. This, however, presents a cryogenic engineering challenge if the control electronics are not also in the ultra-cold environment: high-speed coaxial connections carry a burdensome heat load and noise from the warmer control circuits to the low-temperature quantum circuits. Fortunately, there exists a classical electronics family based on superconductive electronics-rapid single-flux quantum (RSFQ) electronics - that is well suited to integration with analog field sensors, and to precise digital synthesis of voltages [24]. RSFQ circuitry is a well-established superconducting classical electronics technology that relies on the storage and transmission of quantized magnetic flux for information processing with picosecond switching times, allowing many accurately timed control cycles during a computation. Control at ultra-high speeds should allow successful observation of quantum phenomena before coherence is lost. RSFQ circuits operate at low temperatures ($\leq 4.2\,\mathrm{K}$)and low powers ($\sim 1 - 100\,\mu\mathrm{W}$), both of which will be necessary for qubit control. Integrating RSFQ and qubit technologies onto a single chip alleviates the need for high-speed lines and will help enable scaling of the quantum computer

to hundreds or thousands of qubits. Superconductivity therefore provides an optimal technology for quantum computing: a scalable qubit with sufficient long coherence times and an ultra-fast and ultra-precise classical electronics family (RSFQ), both of which can be integrated into a single circuit (schematic representation shown in Fig. 1-5). Together these technologies offer a unified solution to the challenges posed in the development of large-scale quantum computers.

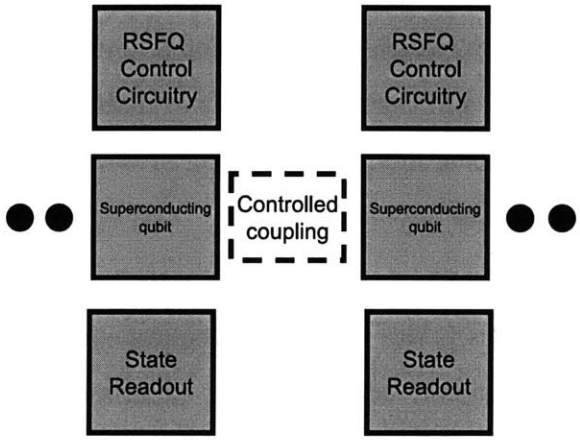

Figure 1-5: A representation of an all superconducting quantum computer. Qubits are magnetically coupled, controlled using superconducting rapid single flux quantum (RSFQ) circuitry and readout using a superconducting flux magnetometer.

Niobium Persistent Current (PC) Qubit

Several groups have proposed superconducting tunnel junction circuits as quantum bits (qubits) for quantum computation (for overview see [8]). The persistent current (PC) quantum bit proposed by Mooij, Orlando *et al.* [25, 26] consists of a $\sim 10\,\mu$m sized loop interrupted by three Josephson junctions (shown in Fig. 1-6). One of the junctions in the loop is smaller by factor α. The two stable states of the PC qubit have persistent currents of opposite direction when an applied magnetic field threading the loop is near a half integer value of a flux quanta Φ_0. A DC Superconducting Quantum Interference Device (SQUID) magnetometer is inductively coupled

to the PC qubit and used to measure the circulating flux states of the qubit. The SQUID employs unshunted, extremely underdamped junctions in order to minimize decoherence. The overall flux signal of the qubit is determined by averaging over many repeated switching current measurements on the meter.

At the appropriate magnetic field bias, the PC qubit under investigation has a double potential well configuration shown in Fig. 1-7. The system has a continuous degree of freedom (the phase across the junctions φ) associated with a potential energy function with two nearly symmetric minima separated by an energy barrier. Using externally applied microwaves, one can induce resonant transitions between macroscopic quantum levels in the system. A major focus of the thesis has been the experimental determination of the time to relax (denoted by τ_d) between quantum levels within the same well of this double well potential.

1.4 Outline

The doctoral thesis presents studies on the design, fabrication, and measurement of the Nb persistent current (PC) qubit. The first two sections describe work encompassing the Nb superconductive fabrication process. The final sections discuss the PC qubit and experimental work performed at dilution refrigerator temperatures.

Chapter 2 begins with an overview of the MIT Lincoln Laboratory Superconducting Device Fabrication Process. The fabrication process is based on a trilayer process, whereby a Nb/Al/AlO_x/Nb sandwich structure is formed in a continuous process step. Optical projection lithography is used to pattern devices containing submicron junction structures. The devices are subsequently defined using standard deposition and etching techniques of the various metal and insulating layers. The fabrication process is critical to the design of the circuits and its characterization is vital to understanding possible mechanisms for decoherence or dissipation.

Fabricating highly uniform Josephson junctions for quantum computing applications and RSFQ circuitry is an essential requirement in the fabrication process. Chapter 3 presents an anodization technique for the Nb superconductive electronics

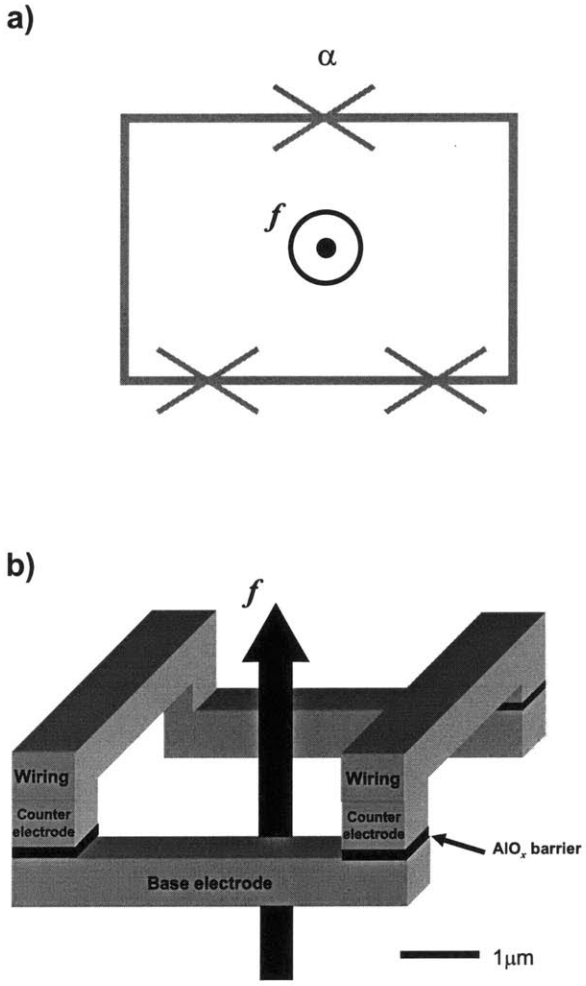

Figure 1-6: a) Circuit representation of the Persistent Current (PC) qubit. The PC qubit consists of a superconducting loop interrupted by three Josephson junctions denoted by an $\times$, one junction is smaller by factor α. The double well potential of the PC qubit system is controlled by the external magnetic field f through the qubit loop. b) Three-dimensional representation of the PC qubit within the Nb trilayer fabrication process. The three corners of the structure contain a Josephson junction while the fourth (upper left) contains a via.

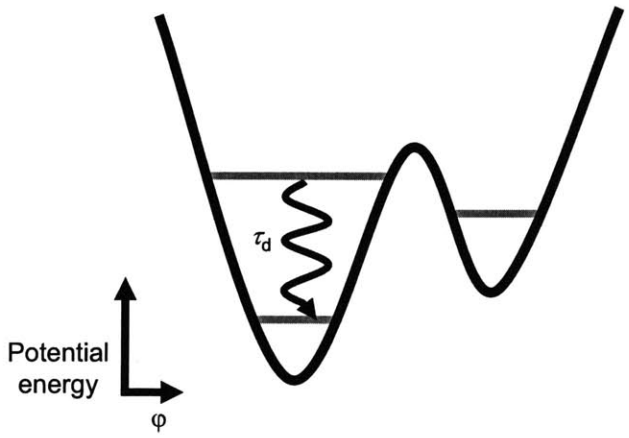

Figure 1-7: The double well potential configuration of the PC qubit near one-half flux quantum ($\Phi_0/2$) magnetic field bias through the loop. The intrawell energy relaxation time τ_d between macroscopic quantum levels has been experimentally determined in a Nb PC qubit.

fabrication process that results in an improvement in critical-current density J_c uniformity across a 150-mm-diameter wafer. The anodization process is outlined and metrology techniques to determine the NbO_x thickness is discussed. Critical current measurements were performed on Josephson junctions distributed across the wafer. The J_c uniformity of wafer pairs, fabricated together and differing only in the presence or absence of the anodization step, was then compared. The cross-wafer standard deviation of the J_c was typically $\times 3$ for unanodized wafers compared to the anodized wafers. The difference in uniformity is suggestive of an in-process modification from an unknown cause that is blocked by the anodic oxide. We discuss possible causes for the difference in J_c uniformity.

The superconducting Josephson junction is the basic element of the qubit and readout device discussed within the thesis. In Chapter 4, we begin with a general discussion of the Josephson junction. The classical electrical behavior is presented and under appropriate environmental conditions, we can describe the Josephson junction circuit using quantum mechanics. From our framework of the basic Josephson

junction, we describe the Persistent Current (PC) qubit. Under suitable device parameters, the three-junction PC qubit loop will have two stable energy states corresponding to persistent currents of opposite direction when an applied magnetic field or frustration f (in units of Φ/Φ_0) is near a half integer value of a flux quanta Φ_0. Near $f = \frac{1}{2}$, theoretical results show that one can approximate the Hamiltonian of our circuit as a two level system. The state readout device is another important component of our qubit system. For our system, a DC SQUID (Superconducting Quantum Interference Device) magnetometer is used to measure the magnetic flux produced by the circulating current in the PC qubit. The final section of the chapter will discuss readout of magnetic flux using a SQUID.

The central work performed within the scope of the thesis is the experimental realization of the Nb PC qubit. Chapter 5 encompasses the entire experimental process - the setup of the dilution refrigerator unit and low-noise electronics measurement system, description of the measurement process, and an analysis of experimental data. One major focus of the experiments on the Nb PC qubit involves microwave spectroscopy measurements. We can induce transitions between the two states of the system by applying low-amplitude microwaves to the PC qubit. We have observed a change in the averaged flux when the microwaves are resonant with the energy level separation of the system. By applying a select range of microwave frequencies, one can map the level separation of the quantum system near given tunnel splittings.

Another main focus of the doctoral research discussed in Chapter 5 is determining the intrawell relaxation time τ_d between macroscopic quantum states within the Nb PC qubit system. Quantifying the dissipation or relaxation mechanism is extremely useful in the design of qubits from various new materials, because it indicates whether the dissipation is at least low enough to make error-tolerant computation feasible. It is important to know whether a promising decoherence time can be achieved in Nb-based Josephson devices, which has a more mature fabrication process compared to other superconducting fabrication processes. The systematic experimental investigation of decoherence, which is a key issue for superconducting qubits, is sparse due to the challenge of the time resolution of the measurement. Long decoherence times have

been demonstrated in some special configurations, however, the limiting sources of decoherence in the superconducting qubits remain unidentified. The decoherence time for superconducting qubits, including energy and phase relaxation times, is predicted to be proportional to the level of energy dissipation, which results from the coupling between the qubits and its environment. All long decoherence times ($\sim 1 - 10\mu$s) reported have been obtained in NbN and Al Josephson devices. For our Nb PC qubit system, a simple three-level classical system was employed to model the dynamic behavior of the PC qubit and determine the energy relaxation time τ_d between macroscopic quantum levels. It was experimentally determined that the intrawell energy relaxation times were of order $\sim 24\mu$sec, in agreement with previous theoretical predictions. These long relaxation times suggest a strong potential for quantum computing employing Nb-based superconducting circuits.

In Chapter 6, we conclude with a summary of major results presented and a brief discussion of the future direction for Nb qubits. The doctoral thesis involves initial measurements showing macroscopic quantum behavior within the Nb PC qubit system. Further work is needed in both material/process engineering research coupled with low temperature coherence measurements to produce reliable, high quality (low dissipation) qubits with long coherence times. Progress to observe coherent oscillations between macroscopic quantum states within this PC qubit system requires improvements in sample isolation and readout. The observation of driven oscillations between levels requires engineering a microwave cavity and a method to rapidly readout the state of the qubit.

Chapter 2

Superconducting Device Fabrication

2.1 Introduction - Superconducting Planar Processing

The fabrication process of a superconducting circuit has important effects and limitations on the device's overall performance. The successful measurement of a device first depends on how well the process technology produces the desired geometry and electrical/physical characteristics [27]. One can easily discuss a submicron Josephson junction at low current densities J_c but in reality how closely can we achieve these results? One also requires a durable circuit which maintains its characteristics through repeated thermal cyclings between room temperature and liquid Helium temperatures and through long durations of time in storage. These considerations show the importance of a well defined, robust process technology. The successful design, fabrication and measurement of a device requires active cooperation between circuit designers, process engineers and low temperature experimentalists.

The superconducting devices discussed within the scope of this thesis are made in a planar processing or planar technology [28]. Planar processing requires creating patterned thin layers of materials with various electrical and material properties on

a supporting substrate. The patterned layers are created, one on top of the other, thereby forming a complete integrated circuit (IC) on each chip. An important aspect of planar technology is that each step of the fabrication is applied to the **entire** wafer. By adding (deposition) or subtracting (etching or lift-off), one obtains the desired geometrical structure of the circuit. Planar processing also contributes to the economic volume production of circuit chips - a 150 diameter wafer can yield several hundred chips, each 5 mm on a side.

The superconducting trilayer fabrication process is a sophisticated and mature technology in development since the early 1980s in the IBM computer project. The trilayer was innovative in that the Josephson junction sandwich was produced in the same continuous operation, without intermediate patterning of the films [29]. The development of the Nb trilayer process with the AlO_x tunnelling barrier has brought Josephson junction technology to a level where complex superconducting circuits can be fabricated reliably [30]. The trilayer fabrication process is continuing to evolve and new techniques are developed to improve tunnel junction quality, hasten production of devices, produce smaller feature sizes, increase the yield of working junctions per chip, etc.

The superconducting devices discussed within the scope of the thesis were fabricated in the Microelectronics Laboratory (MEL) at MIT Lincoln Laboratory, under the supervision of Prof. Karl K. Berggren. The MEL is a class 10 clean room facility, defined as less than 10 particles greater than 0.5 μm in diameter size per cubic foot in the air. We use a doubly planarized all-refractory technology for superconductive electronics (DPARTS) process to fabricate circuits utilizing submicron junctions [23]. The DPARTS process uses optical projection lithography using an i-line stepper, chemical mechanical planarization(CMP) of two silicon-oxide layers, a self-aligned via process and dry reactive ion etching(RIE) of the Nb layers and via etching steps. The circuits are fabricated in a clean room facility in which silicon devices are produced, thereby the Nb superconducting technology is able to collaboratively exploit technological advances within the standard silicon toolset. The following sections briefly discuss the major components of the DPARTS process. We also describe post-process

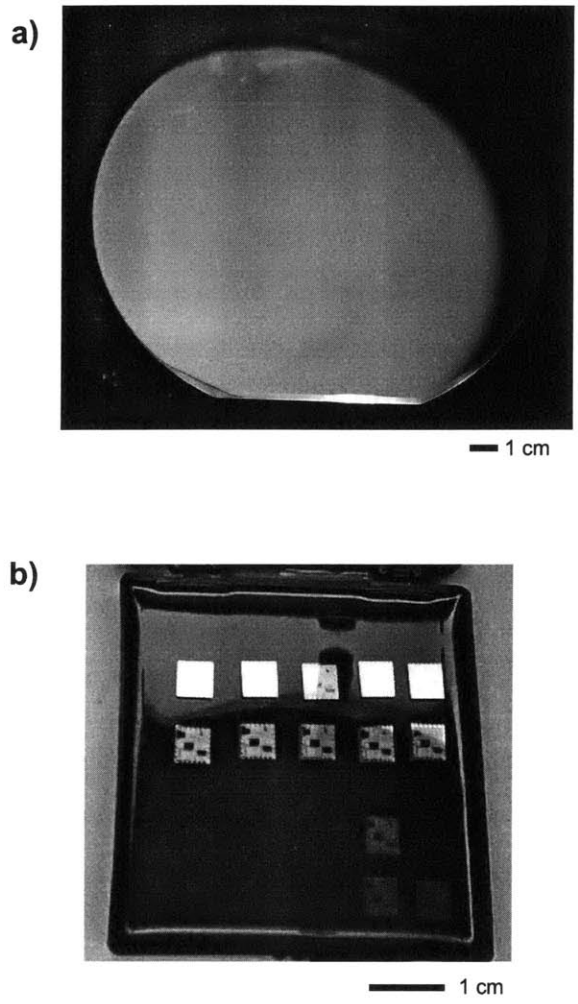

Figure 2-1: a) In planar technology, a process step is applied to the entire wafer. Shown is a 150 mm diameter wafer with a thin-film of Nb deposited on a SiO_2 substrate. b) Completed Nb trilayer superconducting device chips (5 mm on a side) contained in an Electrostatic Discharge (ESD) safe gel-pak.

test methods to ensure that proper targeting of device parameters has been met.

2.2 Wafer Preparation

The substrate preparation is a critical step in the fabrication of Josephson junction devices [31]. The substrate provides the mechanical support for the fabricated circuits. The first step in the process is the wet oxidation of clean, 150-mm diameter, prime silicon wafers (shown in Fig. 2-2). The initial silicon wafers are approximately 675 μm thick. Oxidation occurs at 1000 °C for approximately two hours in a heated furnace, producing a thick $\sim$5000 Å thermal oxide layer on the surface of the wafer. The oxidizing species must diffuse through the already formed oxide surface for the reaction to occur at the interface; the high temperatures aid in this process. Wet oxidation by a supply of water vapor consumes the substrate surface while forming the film, resulting in excellent adhesion. The chemical process on the surface of the wafer proceeds according to the following:

$$Si(s)+2H_2O(g) \longrightarrow SiO_2(s)+2H_2(g)$$

Due to molecular mismatch and thermal expansion differences, the resulting SiO_2 film is under compressive stress. This results in a slight wafer curvature or bending. It is desirable to produce a stable and reproducible surface for the subsequent deposition of the Nb trilayer.

2.3 Trilayer Fabrication

The Josephson tunnel junction is formed in a continuous trilayer process; a superconducting metal (Nb) is deposited, another metal layer (Al) is deposited on top then partially oxidized to form an insulating barrier (AlO_x), and finally a second superconducting metal (Nb) layer is added. The metal films are deposited through sputtering - sputtering requires a non-reactive gas, in our case argon, to shoot and knock off atoms of the intended target (Nb or Al). The scattered atoms then settle and adhere

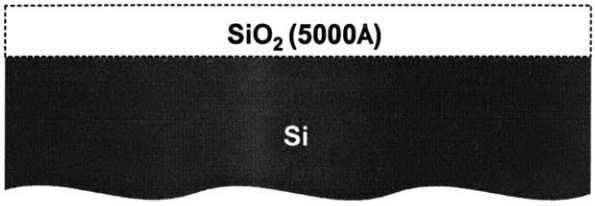

Figure 2-2: Wafer preparation. A $\sim$ 5000 Å silicon oxide layer is thermally grown on the Si substrate to produce a smooth, planar surface for subsequent trilayer growth.

onto the surface we intend to coat. The Nb/Al/AlO_x/Nb trilayer is fabricated in a DC magnetron sputtering system using 6" Nb and Al targets. The system is pumped until a pressure of $< 5 \times 10^{-7}$ Torr is achieved. The highest possible vacuum must be achieved in order to produce the purest films of the desired layer. Nb is then sputtered at 12 mTorr of Ar pressure and 1500 W of power to form a base-electrode 1500 Å thick. After cooling the wafers for one hour, Al is sputtered at 2 mTorr and 1 kW of power, forming a $\sim$ 60 Å thick layer. After another cooling period, the Al surface is oxidized by introducing pure oxygen at pressures ranging from 10-1000 mTorr at times ranging from 10 minutes to 20 hours, the specific time and pressure depend on the desired current density J_c. The current density J_c is defined as the maximum zero-voltage supercurrent (at liquid helium temperatures) passed through the junction per unit area. The current density J_c depends strongly on the pressure-exposure time $(P \cdot t)$ product, the dependence given by [32]

$$J_c \propto (P \cdot t)^{-0.4} \tag{2.1}$$

Long exposure times and high oxygen pressures yield low current densities (thick

oxide barriers) whereas short exposure times and low pressures yield high current densities (thin oxide barriers). The current densities J_c depend exponentially on thickness barrier and therefore, obtaining a precise and repeatable current density J_c value is difficult. Typical current densities in this process range from $100\,\mathrm{A/cm^2}$ to $10\,\mathrm{kA/cm^2}$. After oxidation, the system is again pumped to high vacuum pressures $< 5\times10^{-7}$ Torr. After another hour cooling period, Nb is sputtered to form a counter-electrode approximately 2500 Å thick. A cross section of the Nb trilayer is shown in Fig. 2-3. Following trilayer fabrication, the wafers are allowed to cool then cleaned in a megasonic rinser in a detergent solution, followed by cleaning in deionized water in a spin-rinser dryer.

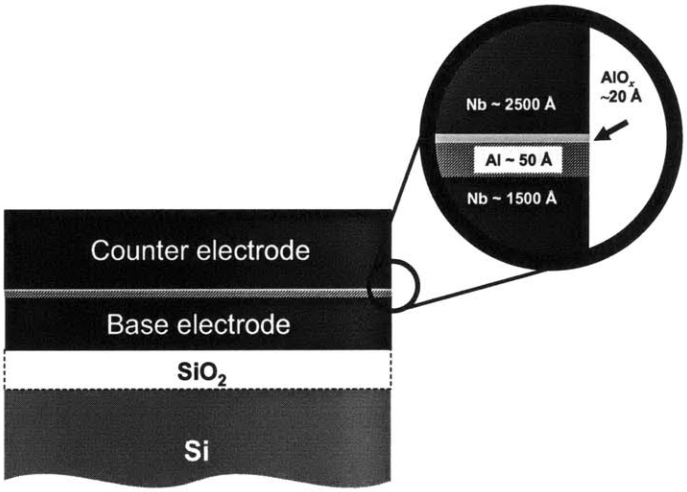

Figure 2-3: Nb/Al/AlO_x/Nb trilayer deposited in a continuous process step. Inset shows a closeup of the AlO_x tunnelling barrier region showing layer thickness values.

The trilayer is a critical step in the fabrication process and it is imperative that low-stress films are produced. It was determined that strains in sputtered Nb films have an important effect on the quality of the junctions, especially small ($< 1 \times 1\,\mu\mathrm{m}^2$) junctions [33]. Other groups have measured strains in Nb sputtered films and determined that the strain depends heavily on Ar pressure during the Nb sputtering. At low pressures, the stress is compressive changing to tensile at higher pressure. By

adjusting the Ar pressure to a zero-stress point (~12 mTorr), we have maintained a low-stress Nb trilayer film.

2.4 Optical Projection Lithography

In optical projection lithography, a pattern on a mask or reticle is projected onto a photoresist covered wafer by means of a high-resolution lens between the mask and wafer [34]. For our system, the patterns are defined using a GCA 5× reduction 365 nm *i*-line stepper. The reticles consist of patterned chromium on a quartz glass plate, fabricated by an external photomask fabrication company such as Photronics Inc. to a tolerance of $\leq 0.25\,\mu$m [35]. The reticle designs were created using a computer aided design (CAD) layout program (KIC). The optical projection system employs refractive lenses that provide 5× reduction over a field of $15\times15\,\text{mm}^2$. The reticle is put in a stepper whereby a laser-interferometer controlled stage steps and repeats the pattern across the entire wafer (Fig. 2-4). A wafer map (Fig. 2-5) shows the step and repeat pattern generated by the lithography step and repeat system.

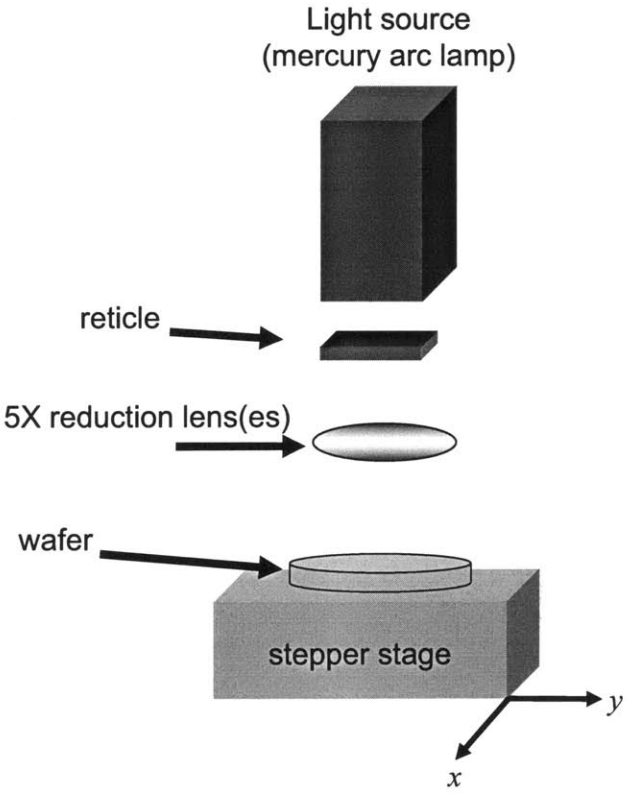

Figure 2-4: Optical Projection Lithography system. A pattern on a reticle is transferred to a resist coated wafer by means of a coherent light source and a series of refractive lenses that provide $5\times$ reduction over a field of $15\times15\,\mathrm{mm}^2$. A laser-interferometer controlled stage steps (in x- or y- direction) and repeats the pattern across the entire wafer.

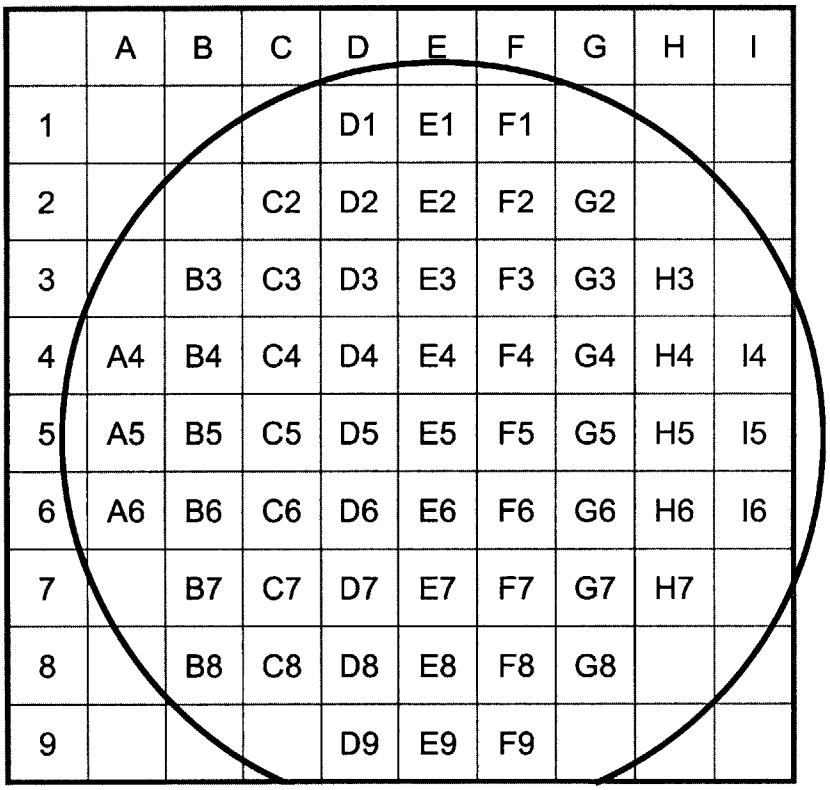

	A	B	C	D	E	F	G	H	I
1				D1	E1	F1			
2			C2	D2	E2	F2	G2		
3		B3	C3	D3	E3	F3	G3	H3	
4	A4	B4	C4	D4	E4	F4	G4	H4	I4
5	A5	B5	C5	D5	E5	F5	G5	H5	I5
6	A6	B6	C6	D6	E6	F6	G6	H6	I6
7		B7	C7	D7	E7	F7	G7	H7	
8		B8	C8	D8	E8	F8	G8		
9				D9	E9	F9			

Figure 2-5: Map of reticle pattern for 150 mm-diameter wafer. Each square box represents a $15 \times 15\,\mathrm{mm}^2$ area whereby the reticle pattern is exposed. The optical projection lithography system steps and repeats the reticle pattern over the entire wafer.

In optical lithographic systems using chrome-on glass reticles, the minimum feature size is generally given as [36]

$$w_{min} = 0.8(\lambda/NA) \tag{2.2}$$

where λ is the wavelength of the light and NA is the numerical aperture of the lens ($NA = n\sin\alpha$). For our system, $\lambda = 365\,\text{nm}$ and $NA \simeq 0.45$, so we find that $w_{min} \simeq 650\,\text{nm}$. This value is comparable to the smallest feature size in the process. For small wavelength, high numerical aperture lenses, we determine the depth of focus R, given as [36]

$$R = \lambda/2(NA)^2 \tag{2.3}$$

In our system, $R \simeq 900\,\text{nm}$, therefore our process requires the surface topography to be less than $\sim 900\,\text{nm}$ for a field size $15\times15\,\text{mm}^2$ in order for features to be in focus during exposure.

For all layers other than the resistor metal and contact pads, we used Shipley SPR-511A positive tone photoresist, applied at 4000 RPM and baked for one minute at 95 °C. Spin coating provides a uniform $\sim$1-2 μm thick resist layer. Hexamethyl disiloxane (HMDS) vapor was used to prime the wafers at 150 °C prior to resist coating. The primer formed bonds with the wafer surface and produced a polar surface to enhance the adhesion of resist to the substrate. The wafers were then placed in the optical lithography system. Alignment and exposure (with a dose of $155\,\text{mJ/cm}^2$) was then carried out to transfer the photomask pattern onto the resist. After exposure, the wafers were baked at 95 °C for one minute then developed using Shipley MFT .245. The resist was finally hardbaked at 115 °C for one minute. The final resist pattern is binary, there is no grey scale or depth to the image, only the presence or absence of resist. The photolithography process is shown in Fig. 2-6.

Liftoff of the resistor layer and contact pads (see sections 2.9 & 2.11) used an image-reversal process. The wafers were primed as done previously then AZ5214-E-IR negative photoresist was spun at 4000 RPM to give a $\sim 1.4\,\mu$m thick photoresist

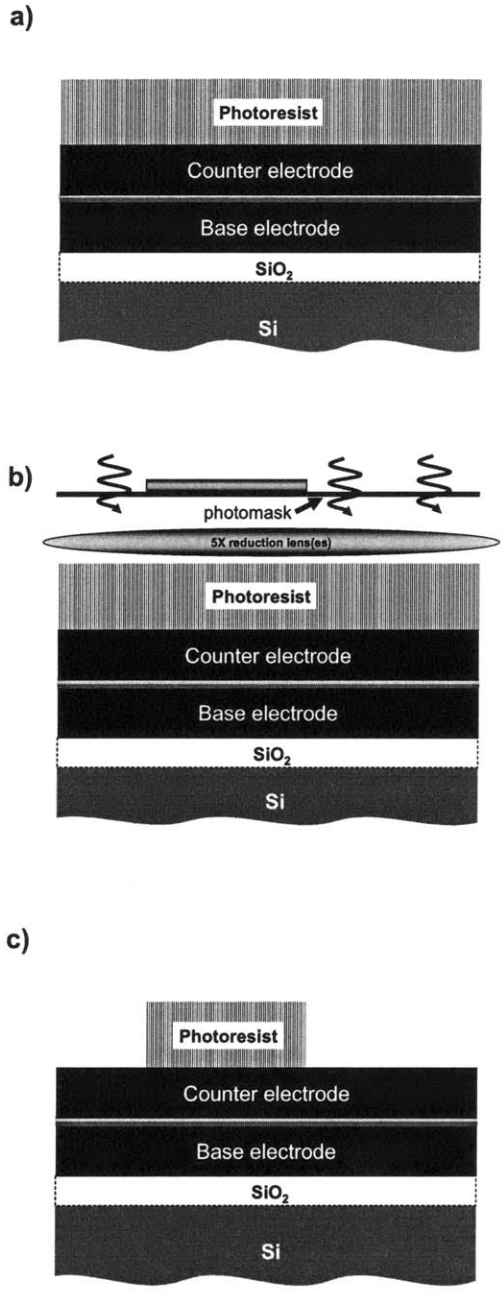

Figure 2-6: a) $\sim 1\mu$m thick photoresist layer is spin-coated to uniformly coat the wafer. b) Resist layer is patterned through exposure through a photomask. c) After exposure, the resist is developed then hardbaked.

layer. The wafers were exposed to a dose of $30\,mJ/cm^2$ then hardbaked at 110 °C for 45 seconds. Next, the wafers were flood exposed at a dose of $300\,mJ/cm^2$ then developed using two puddles of AZ-327 developer for a total of two minutes. This process produced undercut sidewall profiles which allowed for clean liftoff of the metal layer.

2.5 Reactive Ion Etch

In a reactive ion etch, etching occurs by a chemical reaction between the substrate and atoms or radicals produced in a plasma [36]. The plasma used in microfabrication is usually generated in either dc or rf glow discharges; however, rf discharges are generally preferred due to their stability, uniformity and high density of plasmas generated. The material etched is then desorbed as a volatile gaseous species and pumped away. Several advantages to using a gaseous rather than liquid medium include: 1) etch rates tend to be more controllable and 2) the temperature of the substrate can be better controlled.

Etching of the Nb metal layers was done using a load-locked reactive ion etch chamber using SF_6 etch gas at 50 W power, 25 mTorr pressure and a platen temperature of 50 °C. The backside of the wafer was cooled using helium gas. The etching process is nearly identical for the counter-electrodes as for the wiring layer and ground plane. For the base-electrode, we used a higher temperature (80 °C) to etch through the anodized Nb layer (see next section). The etch endpoint was determined by using fluorescence spectroscopy using an optical emission spectrometer. The fluorine intensity of both product and reactant peaks were monitored. The endpoint was stopped by the aluminum oxide barrier in the case of the counter electrode etch or by the PECVD oxide/thermal oxide layers in the case of subsequent Nb layers. Fig. 2-7a shows a cross section of the trilayer after RIE of the counter electrode. The RIE etch process produced a nominal etch rate of $\sim 500\,Å/min$. We used a slight over-etch ($\leq$ 10 sec) for all Nb layers except the wiring layer. The wiring layer required a 90 sec over-etch to adequately remove Nb stringers from the edges of the resistors. The Nb

stringers typically adhere to the side walls of the resistors, typically near the bottom region, and could potentially "short" out the resistors if not adequately removed. All etches were preceded by the etch of two monitor wafers for the purpose of chamber wall passivation.

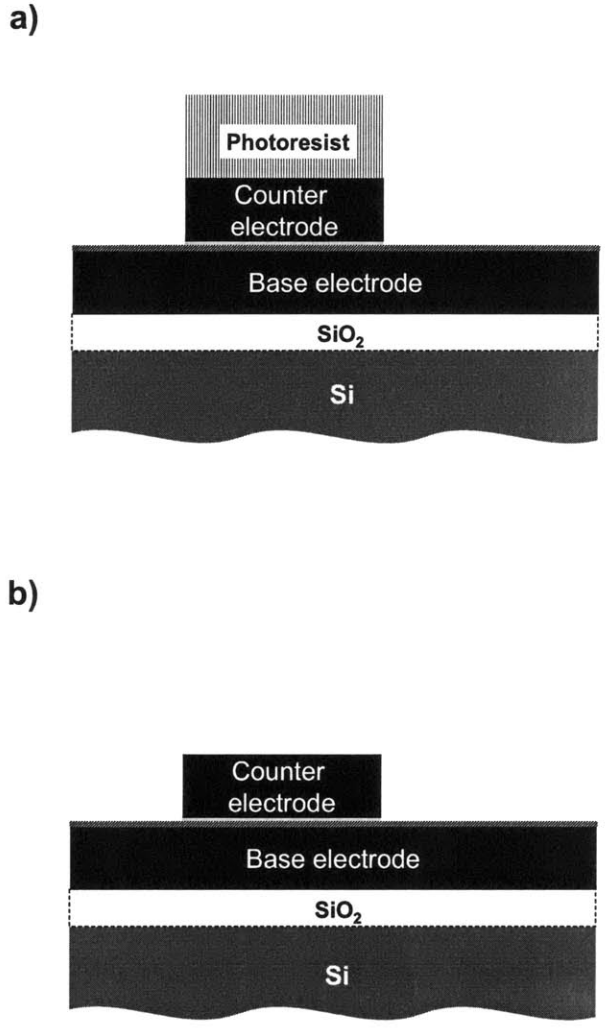

Figure 2-7: a) Patterned counter electrode is reactive-ion etched. b) After RIE, photoresist is removed by immersion in a stripping agent (ACT-935).

Photoresist was removed after metal and oxide etching using ACT-935 photoresist stripping agent. The wafers were immersed in ACT-935 at 75 °C for 30 minutes,

removing resist as well as additional residue. After removal of the photoresist, the wafers were cleaned using deionized water in a dump-rinser and spin-rinser dryer.

2.6 Anodization

Anodization is an electrolytic process in which a metal, in our case Nb, serves as the anode in a suitable electrolyte. When a current passes through the Nb film in the electrolytic solution, the surface is converted to its oxide form, the protective NbO_x layer around the junction perimeter is shown in Fig. 2-8. This oxidation progresses from the solution inward, towards the metal, with the final thickness determined by the applied voltage. The metal-oxide layer serves as a protective barrier to further ionic flow [37]. The anodized layer thus serves to minimize plasma, chemical, or other damage to the junction during further processing steps. Anodization processes of this sort have been used extensively in the past for the fabrication of Nb Josephson junctions [38]-[43]. Anodization has been incorporated into the standard Nb superconductive process to improve the critical-current-density uniformity of junctions. This effect will be explored further in the Chapter 3. The following section gives an in-depth description of the anodization process.

Anodization followed the RIE of the counter-electrode and stripping of photoresist, so the anodization was unmasked. Anodization was performed in an electrolytic solution of tartaric acid ($HOOC(CHOH)_2COOH$) and ammonium hydroxide (NH_4OH). 400 g of tartaric acid powder was added to a recirculating bath of an approximately 5L volume of deionized water (Fig. 2-9a). Then a 28-30% NH_4OH solution was added incrementally until the measured pH was 5.1 ± 0.1 (the total volume of NH_4OH solution added was > 300 ml). The anodization process proceeded as follows: 1) A Pt wafer (cathode) in the electrolytic solution was grounded while the Nb device wafer (anode) was connected to a power supply. 2) Shown in Fig. 2-9b, the voltage output of the power supply was ramped, from 0 V to 20 V, maintaining an initial constant current of 0.225 A through the wafer. The overall ramp time was approximately 50 sec. 3) The voltage was then held constant at 20 V. During the voltage hold time, the current

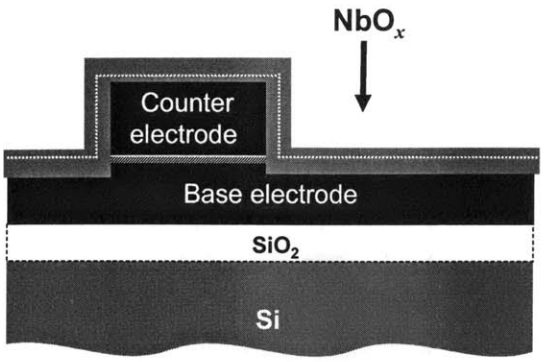

Figure 2-8: Junction is anodized, producing a protective NbO_x layer and effectively "sealing" the perimeter of the junction. Dotted white line indicates original surface.

through the wafers dropped exponentially as the NbO_x layer densified. 4) When the current level reached 10% of its initial value, the power supply was abruptly switched off. The total immersion time was approximately 1.5 minutes. After anodization, the wafers were cleaned using deionized water in a dump-rinser and spin-rinser dryer.

Anodization produced a ~ 500 Å thick NbO_x layer on the surface of the base and counter-electrode for an anodization voltage of 20 V. Fig. 2-10 shows a TEM image of the junction region. Sample preparation and TEM imaging of Josephson junctions was performed by the Microelectronics Center of North Carolina (MCNC) and TEM Analysis Inc. [44]. The NbO_x layer, covering the sidewalls of the counter-electrode, provides a protective layer around the junction perimeter. Comparing anodized/unanodized wafer pairs for wafers with 500 Å of NbO_x, we determined from step-height measurements that the thickness of anodized wafers was typically 300 Å greater than unanodized wafers. From this we conclude that approximately 200 Å of Nb was consumed in the growth process.

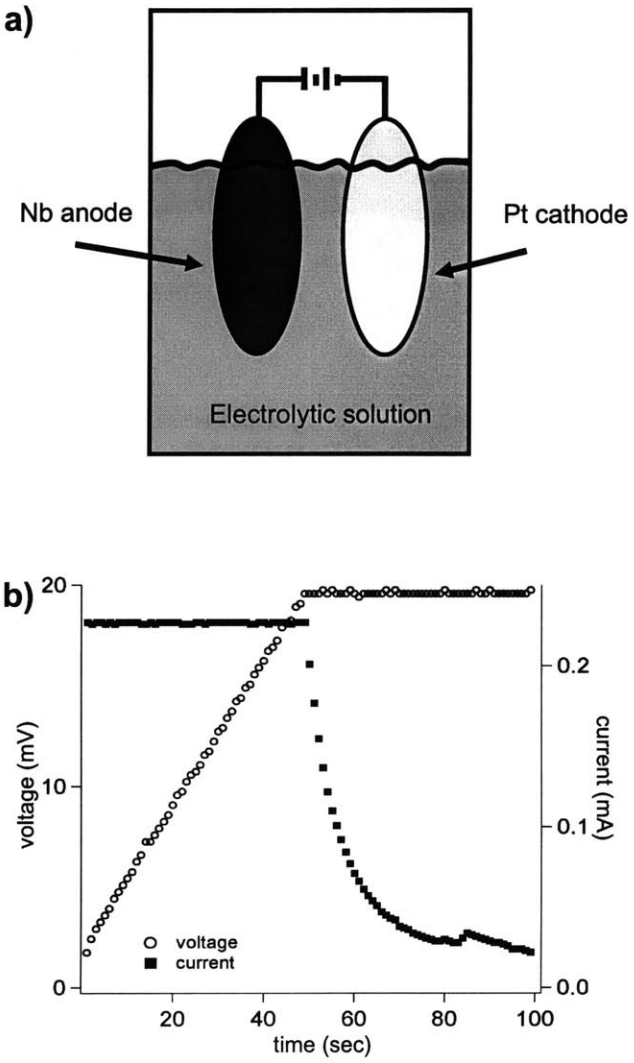

Figure 2-9: a) Setup of anodization process. The Pt wafer is used as the cathode while Nb serves as the anode in the reaction. b) When a current passes through the Nb film in the electrolytic solution, the surface is converted to its oxide form. The plot shows the current biased through Nb wafer and voltage output as a function of time.

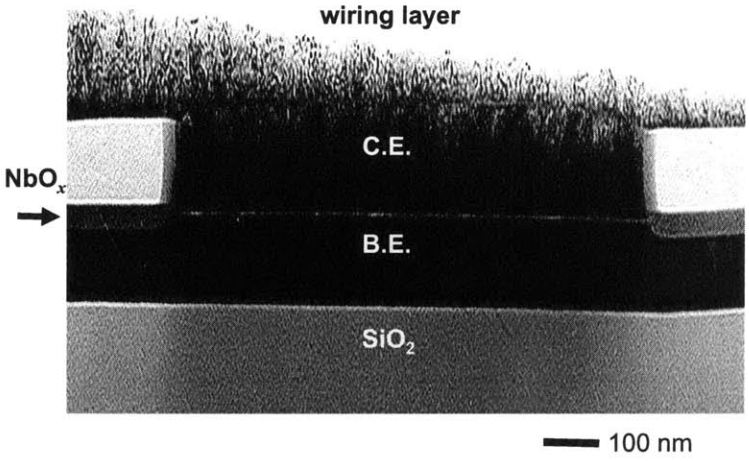

Figure 2-10: TEM image of the Josephson junction region consisting of a thin AlO_x barrier sandwiched between the base-electrode and counter-electrode. A $\sim$ 500 nm thick NbO_x layer serves to protect the AlO_x tunnel barrier from processing damage.

2.7 Aluminum Oxide Barrier Removal/Low Temperature Oxide Deposition

The AlO_x barrier was removed using a wet (chemical) etch - the material is removed by immersion in a liquid bath of chemical etchant. The wafers were placed in a fresh bath of 15% phosphoric acid (H_3PO_4) at 50 °C for approximately 90 sec. The barrier removal was followed by a cleaning step in the dump-rinser and spin-rinser dryer. Fig. 2-11 shows a cross section of the wafer after AlO_x barrier removal.

Plasma Enhanced Chemical Vapor Deposition (PECVD) is an established commercial technique for depositing materials, mainly oxide layers [37]. The maximum processing temperature allowable in any part of a superconducting circuit process is determined by the thermal stability of the Josephson junctions. The major advantage of PECVD is its lower temperature capability compared with other thermally driven CVD. For example, deposition temperatures of 700 to 900 °C are required to deposit silicon oxide films by thermal CVD. At such high temperatures, the quality of the

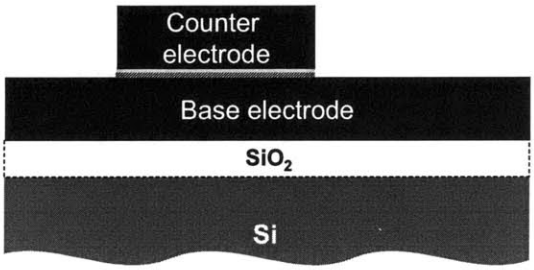

Figure 2-11: Exposed AlO_x barrier is removed using a wet chemical etch.

aluminum oxide barrier would severely degrade. Other groups report that the quality of the junctions remain unchanged up to a "catastrophic" temperature, typically between 180-250 °C [45]. For our PECVD system, deposition temperatures of 150 to 200 °C were sufficient to deposit SiO_2 films.

Silicon oxide is used as an insulating layer between various metal layers in the Nb superconducting fabrication process. PECVD silicon oxide films are used as an insulating dielectric material because of the low deposition temperature and their relatively low dielectric constant [45]. In PECVD, discharge plasmas are sustained within chambers where simultaneous Chemical Vapor Deposition (CVD) reactions occur. The energetic discharge environment was sufficient to decompose gas molecules into its component species; the net effect of the interactions is to cause chemical reactions to occur at a much lower temperature than in conventional CVD reactors without the use of plasma. Previously unfeasible high temperature reactions can be made to occur on the temperature sensitive Nb trilayer wafers.

For our system, oxide was deposited in a load-locked PECVD chamber using a combination of 2% SiH_4 (in He) and N_2O in a ratio of 9:4 at 900 mTorr pressure and 20 W of power. For our system argon diluted silane serves as the silicon source while

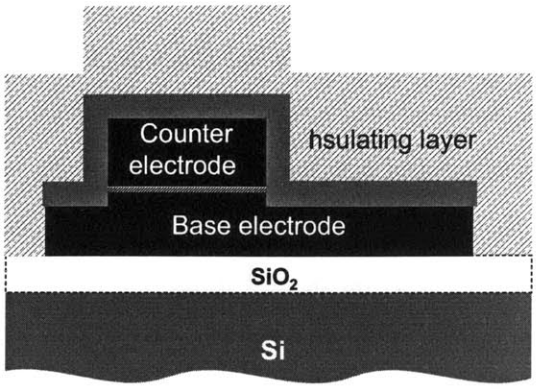

Figure 2-12: After the AlO_x barrier is stripped and the base electrode is etched, a 6000 Å PECVD oxide is deposited as an insulating layer.

nitric oxide (N_2O) serves as the oxygen source. The reaction occurred according to the following

$$SiH_4(g)+2N_2O(g) \longrightarrow SiO_2(s)+2H_2(g)+2N_2(g)$$

The platen was kept at $\sim$ 150°C and the deposition rate was approximately 400 Å/min. For the first PECVD oxide layer, 6000 Å of silicon oxide was deposited while for the second PECVD oxide layer, approximately 7500 Å was deposited. Fig. 2-12 shows a cross-section of the wafer after the first oxide deposition. The low deposition temperature resulted in cracks and voids in the oxide surface. The oxide quality, namely the refractive index and film density, at such low deposition temperatures is typically much poorer than the nominal PECVD processing temperature ($\sim$ 350 °C). However, subsequent planarization (see following section) improved the surface and may have sealed cracks and removed other defects.

2.8 Chemical Mechanical Planarization

Chemical Mechanical Polishing (CMP) is the process of smoothing and planarizing a surface with the aid of chemical and mechanical forces. The technique is widely used in semiconductor processing and has been incorporated into the Nb trilayer process by M.B. Ketchen *et al.* [30]. During CMP, a wafer is pressed against a rotating platen in order to remove a portion of and planarize the wafer surface. Removal of the intended layer is aided by a slurry, which acts to lubricate and erode the top of the wafer.

CMP was used to make self-aligned contact to the counter-electrode and to achieve a planar oxide surface for the Nb ground plane. The wafer is polished in a single-wafer polisher with an IC-60 (Rodel, Inc.) polishing pad and ILD-1300 slurry dispensed at a rate of 100 ml/min. The polish slurry is a dilute colloidal silica based solution. The wafer was pressed against the polishing pad with a pressure of 4 psi and a back pressure of 0.5 psi applied to the wafer. The polish rate was approximately 900 Å/min, and the polish variation across the wafer was $\leq \pm 10\%$. To achieve accurate polish endpoints, CMP was usually done in several steps. After each polish, the oxide thickness was determined by reflectrometry measurements until the desired thickness was achieved. Typically CMP removes ~ 50 nm of the top surface of the counter electrode, therefore removing the NbO_x layer covering the surface and a small portion of the Nb counter-electrode. After CMP, the wafers were cleaned in a megasonic station using a mild detergent. Fig. 2-13 shows a cross-section of the wafer after the first CMP process.

The primary performance advantage of CMP is the offer of global planarity needed for multi-level submicron metallization. The structure must be planarized otherwise deep large vias, aligned to the counter-electrode, must be incorporated to permit contact [46]. Global planarity is required as circuit dimensions extend into the sub-micron regime since lithography tools with high numerical aperture lenses and short wavelengths have relatively small depths of focus (~ 900 nm) [36]. CMP may also reduce or eliminate defects on the silicon oxide surface. Other advantages include improved step coverage and a reduction in severe topography, which allows for tighter

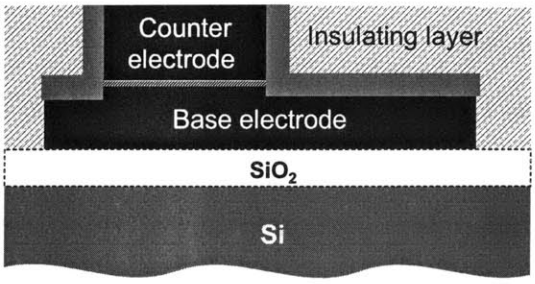

Figure 2-13: CMP of the oxide layer is used to achieve self-aligned contact to the counter-electrode and produces global planarity.

design rules. Severe surface topography leads to large variations in resist thickness making control of dimensions difficult, since thicker resists require longer exposure times while the thinner are will tend to be overexposed.

2.9 Resistor Metal Deposition and Liftoff

Liftoff is a method of forming a pattern on a substrate **following** resist exposure and development. Photoresist is initially spun, exposed and developed to form openings in the resist where material is to be deposited. The material defined is then deposited onto the surface of the substrate. Immersing the wafer into a solvent removes photoresist as well as the material on top.

The resistor metal in the superconducting device fabrication process was defined using liftoff. The liftoff process is detailed in Fig. 2-14a-d. The resistor metal uses 100 Å of titanium followed by 900 Å of platinum. The metal thin films were deposited by electron-beam evaporation in a rotating platen system. Ti was used to adhere the Pt to the silicon oxide surface. Although bulk Ti is superconducting below 1 K, for a sufficiently thin layer, it is resistive for $T \geq 10$ mK [47]. Deposition was controlled

by using a water-cooled quartz crystal microbalance to measure metal thickness. By adjusting the metal thickness, we targeted the low-temperature ($\leq 4.2\,\mathrm{K}$) sheet resistance to be $\sim 0.6\,\Omega/\mathrm{SQ}$. The liftoff process has several distinct advantages over other etching methods [36]:

1) Materials such as Pt and Au are extremely difficult to etch selectively.

2) Patterns in multilayers can be easily achieved. The resistor layers and contact pads in our process consist of two or more layers of differing metals.

3) The substrate is generally not etched or damaged during liftoff.

4) The substrate is kept at a relatively low temperature.

Liftoff of the resistor metal was achieved by immersion in acetone and followed by a cascade rinse in isopropynol. The wafers were subsequently spin-rinsed and spin-dried.

One possible drawback to the liftoff process involves contamination of the resistor edges from out-gassing of the photoresist during metal deposition [48]. Another disadvantage occurs during liftoff; metal film on top of the resist often breaks apart and causes debris that can fall back onto the substrate. We also observed from step-height measurements that lift-off creates raised metal edges around the resistor edges. This typically occurs when the photoresist does not have a re-entrant profile.

2.10 Oxide Etch

Contact between Nb metal layers was achieved through an oxide via. The oxide vias to the base electrode and wiring layers were etched in a rf reactive ion etch system. The recipe consisted of 800 mTorr of 200/20/20 standard cubic centimeters per minute (sccm) $Ar/CF_4/CHF_3$, using 150 W and a cooling stage at -20 °C. The etch rate was approximately 3000 Å/min and the etch time was determined from prometrix measurements of the oxide thickness over the base-electrode. To ensure adequate contact between either the wiring layer and base electrode or ground plane and wiring layer, we include a $\sim 25\%$ overetch of the oxide via.

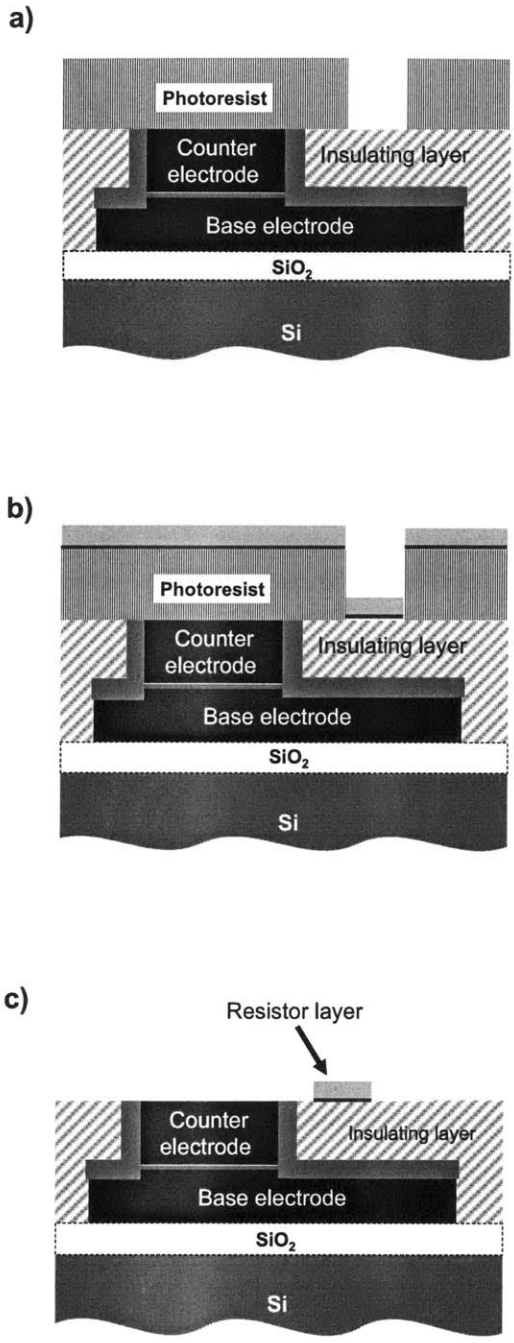

Figure 2-14: Resistor Layer Liftoff process. a) Negative photoresist is spin coated onto wafer surface. After exposure, we define areas where the resistor metal layer is to be deposited. b) Resistor metal layer is deposited in *e*-beam evaporation system. c) Liftoff of the resistor metal layer occurs when immersed in a solvent.

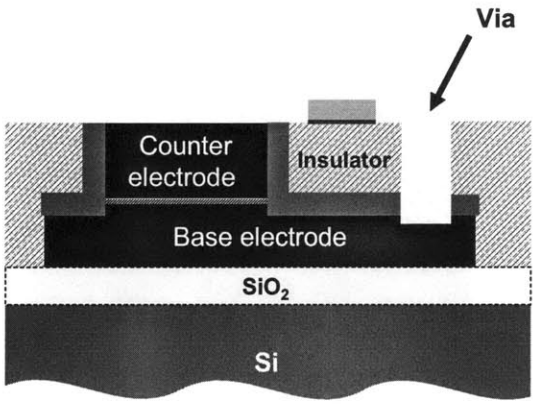

Figure 2-15: Oxide vias are formed to gain electrical contact to the base-electrode.

2.11 Niobium Wiring Layer and Contact Pad Deposition

The Nb wiring layer and ground plane were deposited similar to the counter-electrode and base-electrode (shown in Fig. 2-16a, b). The wafers were loaded into a DC magnetron sputtering system. The system was pumped to a pressure of $\sim 5\times10^{-7}$ Torr, Nb was then sputtered at 10 mTorr of Ar pressure and 1500 W power to form a wiring layer 2500 Å thick or ground plane 4000 Å thick. After sufficient cooling, the wafers were unloaded and cleaned in a megasonic station.

The contact pads were deposited by electron-beam evaporation and defined using liftoff, similar to the resistor metal deposition. The pads consist of 300 Å Ti, 3600 Å Pd and 500 Å Au. Since Au is a contaminant in the standard silicon fabrication facility, the contact pads were deposited in a separate processing laboratory. The metal layers were lifted off in acetone and cleaned in a isopropynol bath. A complete cross-section of a Nb trilayer circuit is shown in Fig. 2-17 with layer thicknesses values indicated in parentheses.

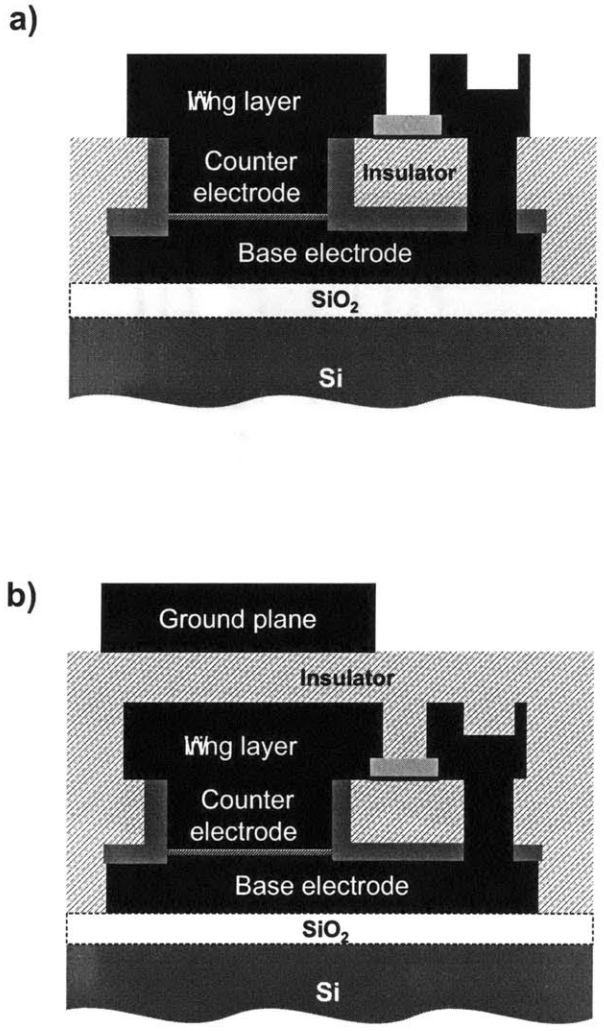

Figure 2-16: a) Nb wiring layer is deposited, patterned then etched. b) After the second CMP process, the ground plane is deposited, patterned and etched.

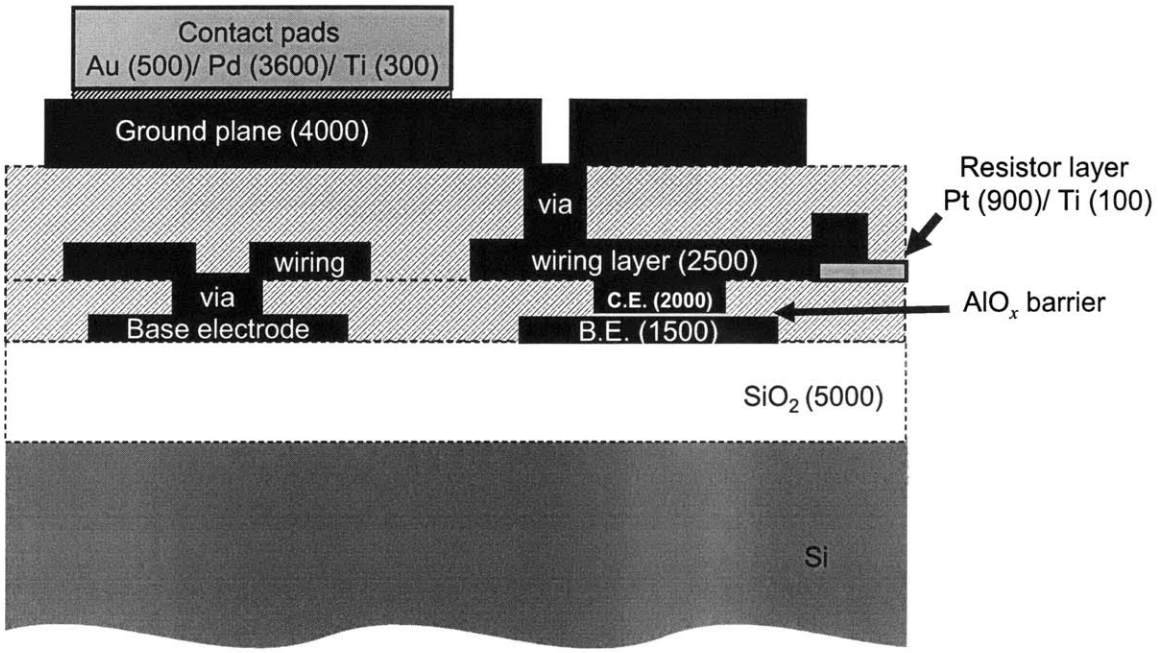

Figure 2-17: Cross-section of completed Nb trilayer circuit. Numbers in parenthesis indicate the thickness values of the layer in Å.

2.12 Process Test Methods

The wafers were tested both in and post-process to determine the overall device parameters of the circuits being fabricated. In-process testing involved measurements of the layer thickness and sheet resistances of the metal layers. For the metal layers, thickness was determined by stepheight measurements using a Tencor P-10 apparatus. For the PECVD oxide layers, thickness was determined by reflectometry measurements. Post-process room temperature testing was performed using an automated wafer probing station. Four point measurements were used to determine: 1) current density J_c, 2) sheet resistance of Nb and resistor metal layers to determine resistivity and thickness and, 3) process control such as oxide shorts or opens in via structures. After room temperature evaluation, the wafers are diced into $5 \times 5\,\mathrm{mm}^2$ chips, wire-bonded into an appropriate chip carrier or package, and finally placed in a low-temperature measurements setup (the post-process method is shown in Fig. 2-18).

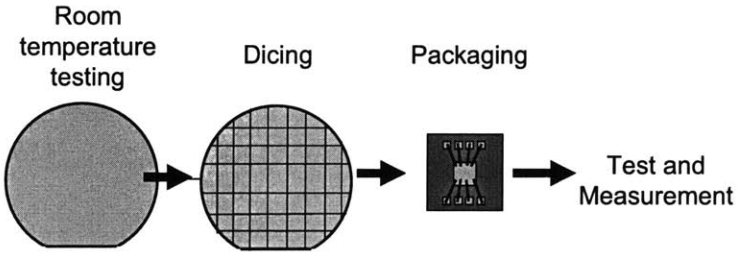

Figure 2-18: Post process test methods. After room temperature measurements, the devices are diced into $5 \times 5\,\mathrm{mm}^2$ size chips, packaged in a chip carrier, then placed in a low-temperature measurement setup.

2.12.1 Room Temperature Evaluation of Junction Critical Current

The major reason to perform room temperature measurements is to determine the overall critical-current-density J_c across the wafer. Determining J_c is imperative for targeting both on target and unform is critical in the process. Shown in Fig. 2-19, we employ specially designed four-point cross-bridge Kelvin resistor (CBKR) structures to determine the normal-state resistance R_n of the Josephson junction. Previous studies have shown that the critical current of a junction can be accurately determined from the room temperature R_n measurements [49]. The room temperature R_n was measured using an automated probing station (Ruckers and Kolls 683A Semi-Automatic Wafer Prober).

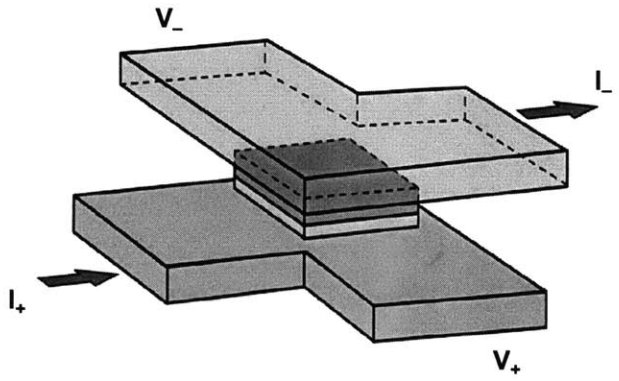

Figure 2-19: Cross Bridge Kelvin Structure (CBKR) test structure to measure normal state resistance R_n of junctions.

The critical current of a junction is determined by the empirical relation [49],

$$I_c R_n = 0.68 \times \frac{\pi \Delta(T)}{2e} \simeq 1.9\,\mathrm{mV}\ (\text{at } 4.2\mathrm{K}) \tag{2.4}$$

where $\Delta(T)$ is defined as the superconducting gap voltage. For Nb, $\Delta(T = 0) = 3\,\mathrm{mV}$. If the area A of the junction is known, then the J_c is easily determined to be

$$J_c = \frac{1.9\,\mathrm{mV}}{AR_n} \tag{2.5}$$

In order to prevent damaging our junctions, we took two precautions: First, to prevent electrostatic discharge (ESD) damage, the probing station pins were grounded before making contact to the junction pads. Second, we used the "make before break" method before applying current through the junction. This method consisted of introducing a resistive path parallel to the junction such that any initial current would run mainly through this resistor. This current path to the junction was then opened so current then flowed through the junction. This method prevented voltage from building up across the junction during the measurement.

Chapter 3

Improving Uniformity of the Critical-Current-Density J_C Uniformity

Controlling the critical-current-density J_c uniformity across a wafer is a major challenge in the Nb Josephson junction trilayer fabrication process. Typically, the J_c variation across a 150-mm-diameter wafer is $>$ 15 % for current densities ranging from 0.1 - 20 kA/cm^2. Highly uniform J_c is desired for producing low cross-chip J_c variation (cross-chip variation is typically ($<$ 1 %) as well as producing a higher quantity of chips per wafer at a given critical-current-density. Past results suggested that anodization of the junction region improves J_c uniformity across a wafer [38][50] as well as junction quality [51] but this suggestion has never been supported with direct comparisons between anodized / unanodized wafers fabricated simultaneously. Anodization has been incorporated into our standard DPARTS process and its effects on J_c uniformity have been studied by directly comparing anodized wafers with unanodized wafers [52]. Described in the previous chapter, the anodization procedure was performed after reactive ion etching of the counter-electrode. Because we felt that after RIE the junction region could be vulnerable to chemical, plasma and/or other damage from subsequent processing steps (shown in Fig. 3-1a), we anodized the wafer to form a 50-nm-thick protective metal-oxide layer around the junction perime-

ter. Fig. 3-1b shows that after anodization the junction region is "sealed" from the outside environment by a thick NbO_x layer. The remaining steps of the process were modified slightly to account for the presence of this layer.

In the following chapter, we discuss the incorporation of anodization into the standard Nb superconducting device fabrication process. We then discuss metrology methods used to determine the thickness of niobium oxide grown. We follow with a discussion of the effects of anodization on critical-current-density uniformity, presenting room-temperature normal-state resistance R_n measurements of junctions. We conclude with discussion and analysis of our results.

3.1 Incorporating Anodization Process

The modification of the fabrication process to include anodization consisted of three steps: 1) the development of the anodization process; 2) the integration of the anodization step into the existing DPARTS process; and 3) the development of metrology methods for process control. Anodization development was described in the previous chapter and in the following sections we discuss work in integration of the anodization process and process control methods.

3.1.1 Process Integration

Subsequent process steps after anodization were modified to account for the NbO_x layer. The NbO_x layer made it difficult to etch through the base-electrode and to gain contact through a via to the base- and counter-electrode. We modified the RIE etching process for the base-electrode slightly from that of the other Nb layers by performing it at a substrate temperature of 80°C (compared to 50°C for the other Nb layers). This elevated temperature was needed to etch through the 50 nm NbO_x layer. We also observed an etch undercut profile due to the anodic oxide (see Fig. 3-2). To achieve contact through the anodic layer at the base of the via (between the base-electrode/wiring layer and counter-electrode/wiring layer) we relied on the 25% over-etch of the PECVD deposited oxide and the pre-sputter of the wiring layer to

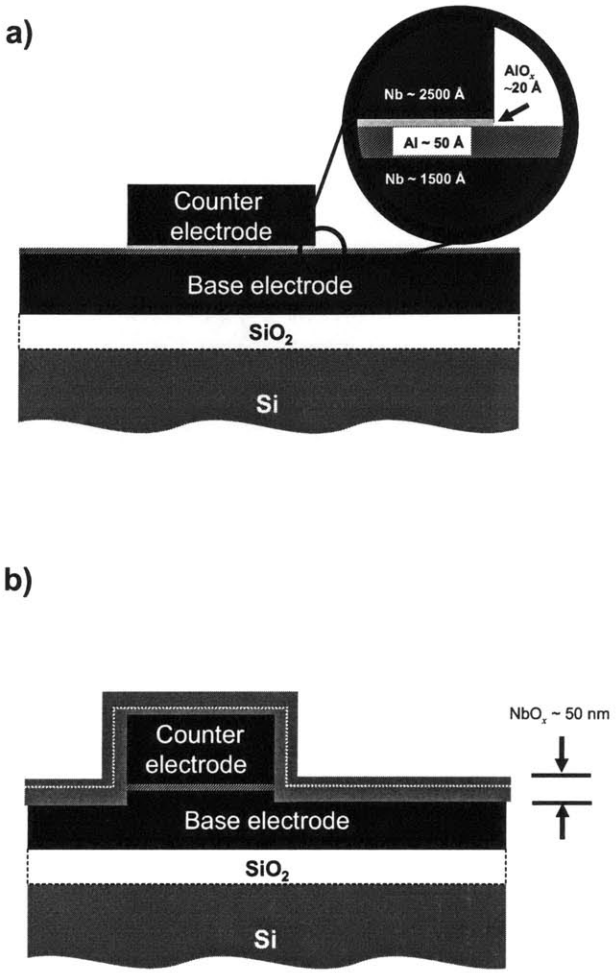

Figure 3-1: a) Nb Josephson junction after counter-electrode etch but immediately prior to anodization. Inset shows the thin AlO_x barrier region is vulnerable to chemical, plasma and/or other damage from further processing steps. b) Junction region after anodization. Junction is anodized, producing a protective NbO_x layer, effectively "sealing" the perimeter of the junction. The surface of the counter- and base-electrode is converted to a metal-oxide layer approximately 50 nm thick. The dotted line shows the original surface. Note: The anodic oxide causes the surface to swell up and out slightly during growth.

promote adhesion between the base-electrode and wiring layer. To achieve contact to the counter-electrode, we used the polishing from chemical mechanical planarization (CMP) and the pre-sputter prior to wiring deposition to remove the NbO_x grown on the top of the counter-electrode.

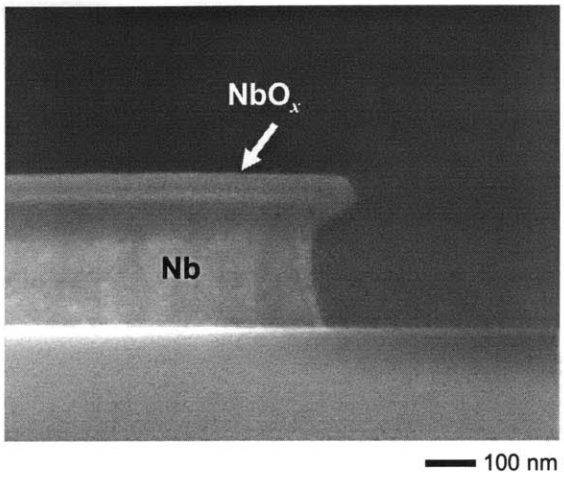

Figure 3-2: SEM image of NbO_x grown on Nb layer. Using an anodization voltage of 20 V, the NbO_x layer is approximately 50 nm thick. We also observe an etch undercut profile due to the anodic oxide.

3.1.2 Thickness Metrology

Determining NbO_x layer thickness is critical for both process control of anodization and for all subsequent dielectric metrology. In our process, film thicknesses are typically measured by using spectral reflectometry, for which the optical constants and thickness of all underlying films are required. Data available in the literature for bulk and thin-film Nb and NbO_x was found to be inadequate: it could not determine the anodic film thickness accurately from spectral reflectometry or ellipsometry. We therefore needed to determine the index of refraction n and absorption coefficient k of the underlying Nb and NbO_x as a function of wavelength λ. To determine the optical constants of NbO_x we first needed an independent measure of the film thickness. We used scanning electron microscopy (SEM) images to determine the film thickness.

We then determined the optical properties of the Nb and NbO_x film using a Hitachi U-4000 spectrophotometer with a 12-degree absolute-reflectance attachment. The resulting reflectance data was used to extract the index of refraction n and absorption coefficients k as a function of wavelength λ for a bulk Nb layer and 95-nm-thick NbO_x layer. The results are given in Table 3.1. NbO_x data varied by a few percent depending on the thickness of the oxide; the range of Cauchy coefficients was from A_n = 2.169 to A_n = 2.236 and from B_n = 0.047 to B_n = 0.05 while A_k and B_k were zero (the range is too small to be important for our purposes therefore we simply used Cauchy coefficients of A_n = 2.169 and B_n =0.047). For Nb the Cauchy coefficients were A_n = 3.20, B_n = -0.086 and A_k = 4.625 and B_k = -0.25. We then compared the film thicknesses extracted from fitting spectral reflectometry data to measurements from SEM images for a variety of anodization voltages and found agreement, as shown in Fig. 3-3. Finally, optical reflectometry and SEM data were compared to ellipsometric analysis at 632 nm and agreement was also obtained.

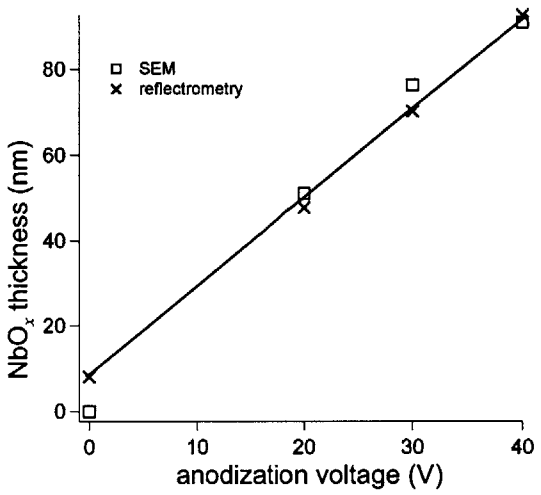

Figure 3-3: NbO_x film thickness for given anodization voltage. Film thickness is determined both by reflectometry measurements and SEM images. The solid line represents the best-fit line to the reflectometry data.

As mentioned previously, we used SEM images to estimate NbO_x thickness and transmission electron microscopy (TEM) images to inspect the anodic film. A SEM

Table 3.1: Optical constants of Nb and NbO_x. Index of refraction n and absorption coefficient k values vs. wavelength for Nb thick film and 95 nm thick NbO_x film.

λ (nm)	Nb n	Nb k	NbO_x n	NbO_x k
400	2.644	3.144	2.565	2.785×10^{-3}
425	2.707	3.262	2.565	1.666×10^{-3}
450	2.788	3.362	2.479	0
475	2.871	3.439	2.454	0
500	2.943	3.500	2.433	0
525	3.000	3.550	2.416	0
550	3.038	3.596	2.401	0
575	3.059	3.643	2.388	0
600	3.065	3.697	2.376	0
625	3.058	3.760	2.365	0
650	3.041	3.834	2.354	0
675	3.018	3.920	2.345	0
700	2.992	4.018	2.336	0
725	-	-	2.327	0
750	-	-	2.320	0
775	-	-	2.313	0
800	-	-	2.306	0

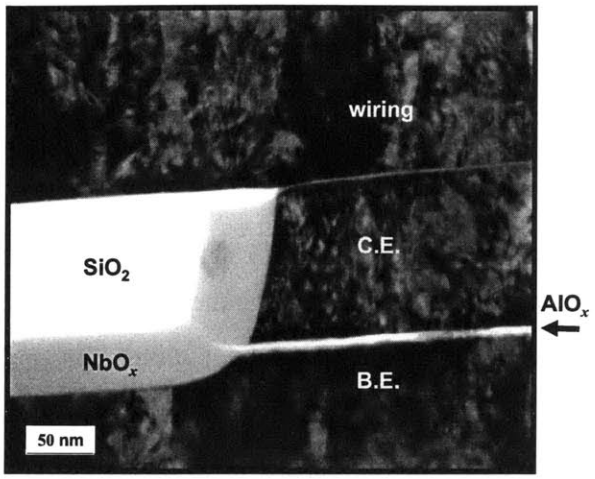

Figure 3-4: TEM image of an anodized junction showing clearly the sealing of the junction edge by NbO_x. Note the clean interface between the counter-electrode (C.E.) and wiring layer where the NbO_x has been removed by CMP.

image of NbO_x grown on a Nb layer is shown in Fig. 3-2. We estimate the thickness of the NbO_x layer to be $\sim 50\,\text{nm}$ for an anodization voltage of 20 V. Sample preparation and TEM imaging of Josephson junctions was performed by the Microelectronics Center of North Carolina (MCNC) and TEM Analysis Inc. [44]. Prior to imaging, the junctions were tested at liquid helium temperatures (4.2 K) and found to have good quality ($V_m > 50\,\text{mV}$). TEM images of the anodized junction region is shown Fig. 3-4. Comparing anodized/unanodized wafer pairs for wafers with 50 nm of NbO_x, we determined from step-height measurements that the thickness of anodized wafers was typically 30 nm greater than unanodized wafers. From this we conclude that approximately 20 nm of Nb was consumed in the growth process.

3.2 Effect of Anodization on Critical-Current-Density Uniformity

In order to determine the effect of anodization on the electrical characteristics of our junctions, we looked at their normal-state resistance R_n at room temperature. We

calculated the critical current I_c of a junction from the R_n measurements for a large quantity of junctions distributed across an entire wafer using an automatic probing station. From these measurements we determined critical-current-density uniformity for several anodized / unanodized wafer pairs where, for each pair, the trilayers were fabricated together.

Room temperature measurements using specially designed test structures were used to determine the overall critical-current-density across the wafer. We employed four-point cross-bridge Kelvin resistor (CBKR) structures to determine the normal-state resistance R_n of the Josephson junction as described in previous chapter. From the R_n values obtained at room temperature, we determined the approximate value of the critical current I_c of the junction. From the known junction area ($10 \times 10\,\mu\text{m}^2$), we then able to extract the J_c value.

3.3 Results/Analysis

Fig. 3-5 shows the J_c percent standard deviation across a wafer for six wafer pairs. Each pair was fabricated together, the only difference being the presence or absence of anodization. Also, for each pair of wafers, the trilayer formation was performed simultaneously. The percent standard deviation of J_c was typically $\sim 5\%$ for anodized wafers but $> 15\%$ for unanodized wafers. Overall, unanodized wafers had a factor of $\sim$ 3 higher standard deviation compared to anodized wafers. Error in room-temperature R_n measurements due to the finite lead resistance and sizing errors could not account for this difference in critical-current-density uniformity [49].

Our results suggest that there exists in-process modification of J_c that is avoided or diminished by anodization. The wafer pairs we examined were simultaneously subjected to the same highly uniform oxidation process involved in producing the tunnelling barrier, therefore making it unlikely for one wafer to differ significantly in J_c uniformity from the other. Isolating the cause of the modification remains difficult since many subsequent processing steps are required to produce useful junctions. Possible sources of damage or contamination of the junction barrier include: stress in the

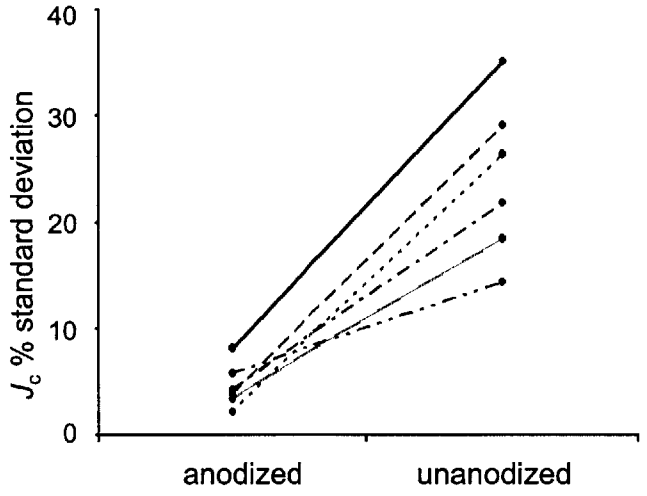

Figure 3-5: Comparison of cross-wafer critical-current-density standard deviation of anodized / unanodized wafer pairs. The wafers shown have J_c values ranging between 10^2 A/cm^2 and 10^3 A/cm^2. Lines connect data points on wafers whose trilayers were deposited together.

Nb film, plasma, and/or chemical sources (photoresist / developer, phosphoric acid, CMP slurry). Clearly, anodization reduces cross-wafer I_c spreads of large junctions ($> 2\times2\,\mu$m^2) suggesting that the anodic oxide layer retards attack of the junction. However, from separate room temperature and low temperature measurements, we have determined that anodization does not improve cross-wafer spread of small junctions ($< 2\times2\,\mu$m^2) since small junction I_c is mainly dominated by sizing variation rather than J_c variation and anodization does not appear to affect sizing variation.

Chapter 4

Superconducting Quantum Circuits

The Josephson junction is the basic building block of our physical qubit system and magnetic flux readout device under investigation. The following chapter begins with the fundamental electrical characteristics of the superconducting Josephson tunnel junction. The tunnel junction can be described both classically and under appropriate conditions, quantum mechanically. Next, we present a general overview of the persistent current (PC) qubit, describing previously developed theoretical work. We end with a discussion of our qubit state readout device - the magnetic flux meter or DC SQUID magnetometer.

4.1 Superconducting Tunnel Junction

The superconducting tunnel junction consists of two superconductors separated by an thin insulating barrier $\sim 10\,\text{Å}$ (shown in Fig. 4-1). At sufficiently low temperatures ($T \leq 9.2\,K$ for Nb), electrons in the superconductors condense into a "superfluid" with electrons of opposite spin pairing up to form a resulting "particle" known as a Cooper pair. The Cooper pairs have a net spin of zero, acting effectively as bosons that condense into the same macroscopic quantum state. In 1962, Brian Josephson predicted the probability of a Cooper pair tunnelling through the barrier was the same

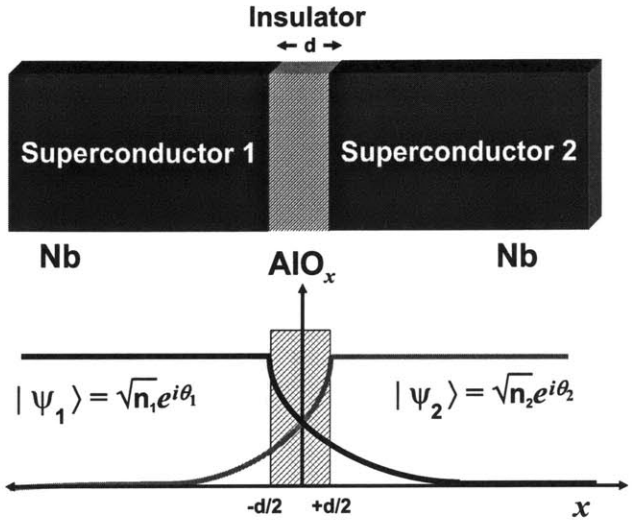

Figure 4-1: Superconducting Tunnel Junction. The junction consists of two superconductors separated by an insulating layer. For a sufficiently thin insulating barrier, the macroscopic wavefunctions of the superconductors ($|\psi_1\rangle$ and $|\psi_2\rangle$) interact.

as that for a single electron. The tunnelling of Cooper pairs is an ordered coherent process, like the coherent light emitted from a laser. When the barrier width d is large ($d > 100\,\text{Å}$) the macroscopic wavefunctions of the two superconductors $|\psi_1\rangle$ and $|\psi_2\rangle$ do not overlap but if the barrier is sufficiently thin ($d \sim 10\,\text{Å}$), the macroscopic wavefunctions of the two superconductors interact [53].

We analyze the dynamics of the Josephson effect by considering a Josephson junction in which regions 1 and 2 are the same superconducting metal [54]. The corresponding macroscopic wavefunctions in region 1 and 2 are $|\psi_1\rangle$ and $|\psi_2\rangle$ respectively. The wavefunctions in the superconductors have an effective density and phase - we assume the wavefunctions then are of the form,

$$|\psi_1\rangle = \sqrt{n_1}e^{i\theta_1} \tag{4.1}$$

$$|\psi_2\rangle = \sqrt{n_2}e^{i\theta_2} \tag{4.2}$$

where n_1 and n_2 are the densities of Cooper-pair electrons in superconductor 1 and

superconductor 2 respectively and θ_1 and θ_2 are the associated phase angles of the wavefunctions in the two superconductors.

The time-dependent Schrödinger wave equation for the two superconducting regions are:

$$i\hbar\frac{d|\psi_1\rangle}{dt} = U_1|\psi_1\rangle + T|\psi_2\rangle \tag{4.3}$$

$$i\hbar\frac{d|\psi_2\rangle}{dt} = U_2|\psi_2\rangle + T|\psi_1\rangle \tag{4.4}$$

where U_1, U_2 are the energy of the system and T is the electron-pair coupling term or transfer interaction across the insulator. For $T = 0$, U_1, U_2 represent the lowest energy states of the superconductors in regions 1 and 2. If the we connect the two superconducting regions to the terminals of a battery, there is a potential difference between across the junction, $U_1 - U_2 = 2eV$ (where $e = |e|$). Using the form of the wavefunctions from Eqns. (4.1) - (4.2) into Eqns. (4.3) - (4.4), we have,

Equating the real and imaginary components, we obtain

$$\frac{dn_1}{dt} = \frac{2T\sqrt{n_1 n_2}}{\hbar}\sin\theta \tag{4.5}$$

$$\frac{dn_2}{dt} = \frac{-2T\sqrt{n_1 n_2}}{\hbar}\sin\theta \tag{4.6}$$

$$\frac{d\theta_1}{dt} = \frac{T}{\hbar}\sqrt{\frac{n_2}{n_1}}\cos\theta - \frac{2eV}{2\hbar} \tag{4.7}$$

$$\frac{d\theta_2}{dt} = \frac{T}{\hbar}\sqrt{\frac{n_1}{n_2}}\cos\theta + \frac{2eV}{2\hbar} \tag{4.8}$$

where $\theta = \theta_2 - \theta_1$. From the above equations, one determines the current density J from region 1 to region 2 to be $\frac{dn_1}{dt}$ (or -$\frac{dn_2}{dt}$) or

$$J = \frac{2T}{\hbar}\sqrt{n_1 n_2}\sin\theta \tag{4.9}$$

for simplicity, we write,

$$J = J_0 \sin\theta \tag{4.10}$$

where $J_0 = \frac{2T}{\hbar}\sqrt{n_1 n_2}$. The final equations describes the time rate of change of the phase $\dot{\theta}$ given by,

$$\frac{d\theta}{dt} = \frac{d\theta_2}{dt} - \frac{d\theta_1}{dt} = \frac{2eV}{\hbar} \tag{4.11}$$

Eqns (4.9) and (4.11) are the general equations for a Josephson junction.

4.1.1 Current-Voltage Characteristics of a Josephson Junction

Josephson derived the governing equations for an ideal superconducting tunnel junction. In the previous section, we showed that an applied current I controls the gauge invariant phase difference $\varphi = \varphi_1 - \varphi_2$ between the two superconductors [53]

$$I = I_c \sin\varphi \tag{4.12}$$

we define I_c as the critical current or maximum supercurrent the junction can sustain. At finite temperatures, the critical current I_c of the Josephson junction is given by the Ambegaokar-Baratoff relation

$$I_c(T) = \frac{\pi\Delta(T)}{2eR_n}\tanh\left(\frac{\Delta(T)}{2k_BT}\right) \tag{4.13}$$

where R_n is the normal state resistance of the junction and the gap voltage $\Delta(T)$ can be numerically approximated by [55]

$$\Delta(T) = \Delta_0\left[\cos\frac{\pi}{2}\left(\frac{T}{T_c}\right)^2\right]^{1/2} \tag{4.14}$$

For Nb, $\Delta_0 = 1.5\,\text{mV}$. When the applied current increases from zero, initially there is no voltage across the junction. However, when $I > I_c$, we find from Eq. (4.11) that

a discontinuous voltage V appears across the junction (Shown in Fig. 4-2b) and the phase difference φ evolves with time according to the voltage-frequency relation,

$$\frac{d\varphi}{dt} = \frac{2\pi}{\Phi_0} V \tag{4.15}$$

where Φ_0 is a flux quantum and has the value $\Phi_0 = \frac{h}{2e} = 2.0679 \times 10^{-15}\,\mathrm{T{\cdot}m^2}$.

We can model a Josephson junction as an ideal Josephson junction in parallel with an external shunt resistor R and self-capacitance C, shown in Fig. 4-2a. Describing the equation of motion, we obtain [56, 57]

$$I = I_c \sin\varphi + \frac{V}{R} + C\frac{dV}{dt} \tag{4.16}$$

using Eq. (4.12) and Eq. (4.15), we can rewrite the above equation

$$\frac{\hbar C}{2e}\ddot{\varphi} + \frac{\hbar}{2eR}\dot{\varphi} = I - I_c \sin\varphi = -\frac{2e}{\hbar}\frac{\partial U}{\partial \varphi} \tag{4.17}$$

where we define U as,

$$U = -\frac{\Phi_0}{2\pi}(I\varphi - I_c \cos\varphi) \tag{4.18}$$

We realize that Eq. (4.17) describes the motion of a ball moving down an inclined washboard potential U [53]. The self-capacitance C is analogous to the mass of the object and the $1/R$ term describes the damping of the system. The degree of tilt of the washboard is determined by the bias current I. Shown in Fig. 4-3, for $I < I_c$, the particle is confined to one of the washboard potential wells, where it oscillates back and forth at plasma frequency,

$$\omega_p = {\omega_{p0}}^{1/2}\left[1 - \left(\frac{I}{I_c}\right)^2\right] \tag{4.19}$$

where $\omega_{p0} = 2\pi I_c/\Phi_0 C$. In this state, the time averaged voltage across the junction is zero, corresponding to $\langle\dot{\varphi}\rangle = 0$. As we increase the current above I_c, the tilt of the washboard increases such that the potential barrier ΔU to exit to the next potential

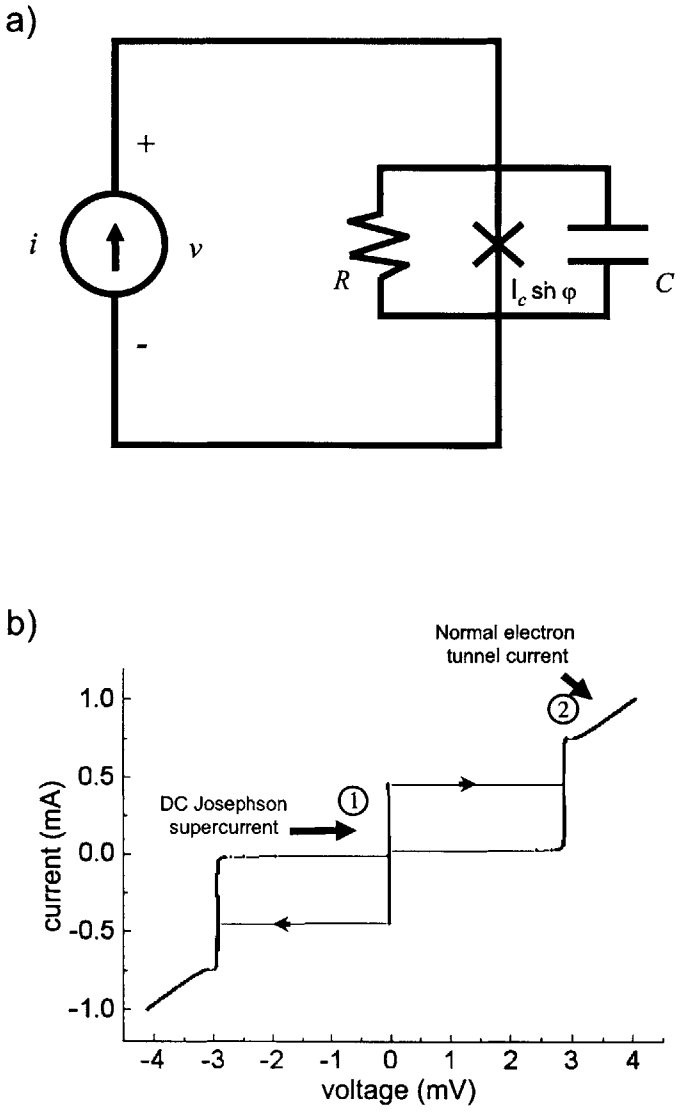

Figure 4-2: a) RCSJ model of a Josephson junction. A Josephson junction is modelled as a resistor and capacitor in series with an ideal Josephson junction (denoted by an $\times$) b) I-V curve of a $6\times6\mu\text{m}^2$ underdamped Nb Josephson junction at $\text{T} = 380\,\text{mK}$. Below a certain bias current value I_c, the junction is in its superconducting state. When the current exceeds I_c, the junction switches to its normal resistance state.

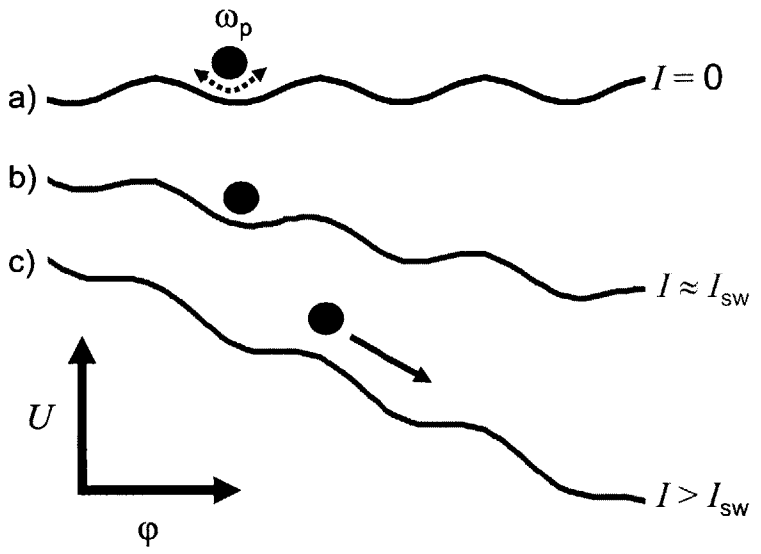

Figure 4-3: Washboard potential of the Josephson junction for various applied current values I. a) for applied current $I = 0$, the particle oscillates back and forth in a potential well at frequency ω_p b) Near $I \approx I_{sw}$, the particle escapes the metastable well through thermal activation over the potential barrier. c) The junction is in its finite voltage or "running" state.

well is given by

$$\Delta U = \frac{\Phi_0 I_c}{2\pi}\left[1 - \frac{I}{I_c}\right]^{3/2} \tag{4.20}$$

The rate to thermally overcome the potential barrier Γ_{th} is given by

$$\Gamma_{th} = \tau_{th}^{-1} = \alpha_d \frac{\omega_{p0}}{2\pi} e^{-\frac{\Delta U}{k_B T}} \tag{4.21}$$

where $\alpha_d = \frac{7.2\Delta U}{Qk_BT}$ is the damping parameter of system, which depends strongly on the quality factor Q. Eqn. (4.20) is valid only for large Q values. Once in its "running" state, the particle rolls down the washboard potential and a voltage appears across the junction. In the case of low damping ($R \rightarrow \infty$), the particle is again confined to a potential well only when I is reduced to a value much less than I_c. A typical $I - V$ curve of an underdamped junction is given in Fig. 4-2b. For Josephson junctions used

in quantum computing applications, we are concerned mainly with the underdamped (hysteretic) case. For this we require

$$\beta_c = \frac{2\pi I_c C R^2}{\Phi_0} \gg 1 \tag{4.22}$$

where β_c is known as the Stewart-McCumber admittance parameter [58].

4.1.2 Switching Current Distribution of Junction

The measured switching current value of a junction, defined as the current value at which the junction switches to its finite voltage state, is always less than I_c due mainly to thermal noise in the system. Fig. 4-4 shows a typical switching current distribution of a Josephson junction. The noise-induced activation is a stochastic process occurring at a rate dependent on I, the value of the switching current takes on random values a certain probability distribution $P(I)$ [59]. This distribution is defined by the condition that the probability the junction switches between I and $I + \delta I$ is $P(I)\delta I$. The measured $P(I)$ can be related to the transition rate τ over the potential barrier defined previously. The probability distribution in I is given by

$$P(I) = \tau(I)^{-1} \left(\frac{dI}{dt}\right)^{-1} \left[1 - \int_0^I P(i)di\right] \tag{4.23}$$

where $\left(\frac{dI}{dt}\right)$ is the bias current ramp rate. From the known capacitance C and critical current I_c of the junction, one can use a theoretical fit to compare to the experimental probability distribution. The effective noise level of the system can be characterized and determined if the noise in the system is thermal-noise-limited.

Fig. 4-5a shows a series of switching probability distributions $P(I)$ versus applied current at various temperatures. The $P(I)$ has an intrinsic asymmetry with a tail at low I and a more abrupt cutoff at high values of I. As temperature is lowered $T \to 0$, we expect the probability distribution width σ to narrow (standard deviation decreases shown in Fig. 4-5b) and the average switching current value to increase. As T is lowered to $k_B T < \hbar\omega_{p0}/20$, the probability distribution width σ is independent of

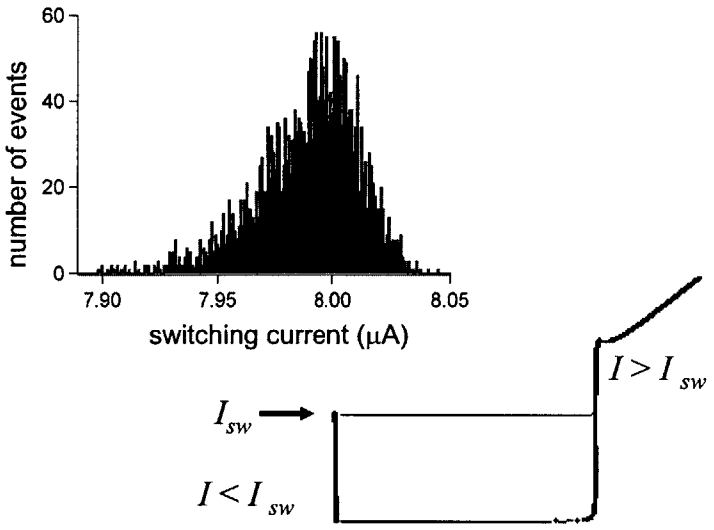

Figure 4-4: Switching current distribution of a $I_c \approx 8\mu$ A junction at $T \approx 12$ mK. 10^3 switching events are taken to create a switching current histogram.

T. At these temperatures, thermal activation over the potential barrier is negligible and quantum tunnelling effects begin to dominate.

4.1.3 Josephson Junction as a Non-linear Inductor

From the Josephson junction governing equations, we show that the Josephson junction behaves like a non-linear inductor [60]. The voltage v across an inductor is given as

$$v = L_J \frac{dI}{dt} \tag{4.24}$$

using Eq. (4.12) and (4.15) to solve for the inductance of the junction L_J in terms of the critical current I_c and φ,

$$L_J = \frac{\Phi_0}{2\pi I_c \cos\varphi} \tag{4.25}$$

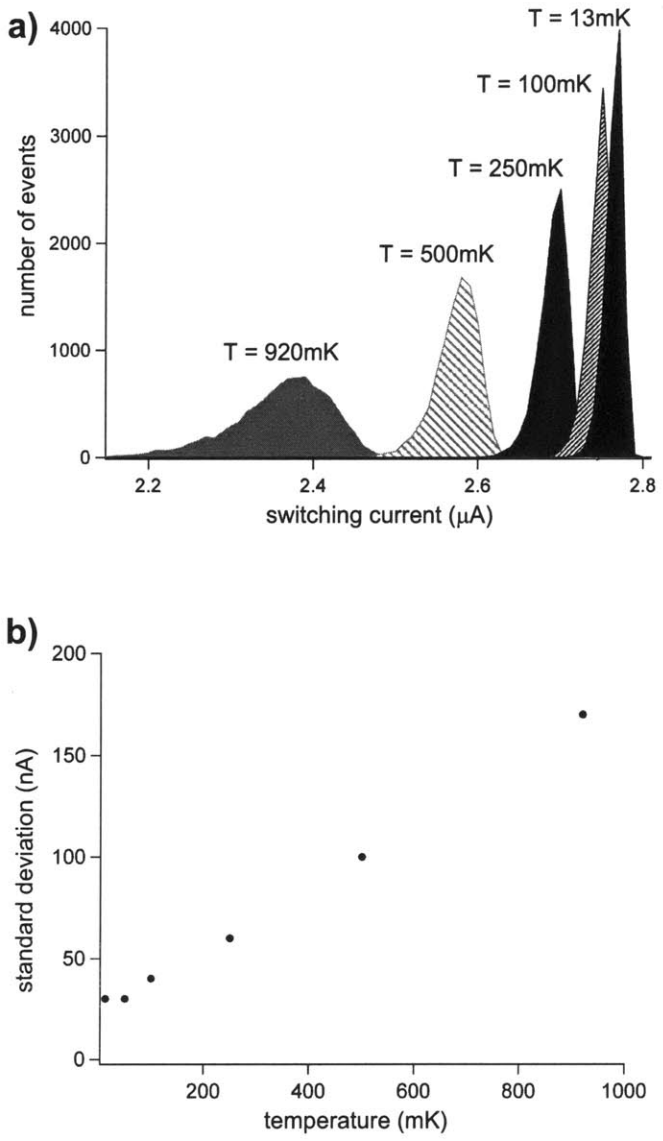

Figure 4-5: a) Switching current probability distribution of $I_c \approx 2.8\mu$A junction for various temperatures. As temperature decreases, the switching current I_{sw} increases and the standard deviation of the switching current decreases.b) Standard deviation σ of the switching current vs. temperature. The standard deviation decreases linearly with temperature. At sufficiently low temperature, thermal activation is not dominant and σ saturates.

We find that the Josephson junction acts as a non-linear inductor L_J. A non-linear inductor has two important consequences for observing quantum effects. First, the existence of a wave-packet associated with the phase difference φ can be demonstrated to decay into a metastable ground state by tunnelling. This process is known as Macroscopic Quantum Tunnelling (MQT). Second, one can observe the quantized energy levels spectroscopically since the quantum and classical responses differ when an external perturbation is applied.

4.2 Quantum Properties of Josephson Junctions

With current fabrication technology pushing the size of tunnel junctions into the submicron regime, more and more research has involved Josephson junction devices to study quantum mechanics at macroscopic scales [9]-[22]. For the case of a Josephson junction enclosed in a ring geometry, the macroscopic degrees of freedom are the magnetic flux Φ and the charge Q on the junction. We define Q as twice the charge of an electron e times the number of Cooper pairs N, $Q = 2eN$. One can design the circuit such that either the Josephson (magnetic) energy E_J or the charging energy E_c is the significant parameter. In the former case, the magnetic flux enclosed in a ring geometry is the well-defined quantum degree of freedom and in the latter case, the number of Cooper pairs on a superconducting island is the well-defined degree of freedom. If we treat these as operators, the operator $\hat{\varphi}$ is the quantum-mechanical phase conjugate to the operator $\hat{Q}$ so we have as our uncertainty relation,

$$\Delta\hat{\varphi}\Delta\hat{N} \geq 1 \tag{4.26}$$

Let us determine the Hamiltonian of a single tunnel junction [60]-[62]. We find that the Josephson junction can be modelled as a non-linear inductor in parallel with a capacitor (we regard the junctions as dissipationless). The charging (capacitive) energy is due to the sandwich structure of the junction and is the usual energy associated with a capacitor C,

$$U_c = \frac{1}{2}CV^2 = \frac{Q^2}{2C} \tag{4.27}$$

We determine the free energy required to change the phase of the Josephson junction. The Josephson energy is calculated by integrating the power dissipated from the system $\int_0^{t_0} VIdt$. V is the voltage generated while the current I is being changed from zero current at $t = 0$ to its final current value at time $t = t_0$. Using Eq. (4.12) and (4.15) to write the current I and voltage V in terms of phase, this yields

$$U_J = E_J(1 - \cos\varphi) \tag{4.28}$$

where $E_J = \frac{\Phi_0 I_c}{2\pi}$. The total Hamiltonian of our system is found to be,

$$\hat{H} = \frac{\hat{Q}^2}{2C} + E_J(1 - \cos\hat{\varphi}) \tag{4.29}$$

Let us make the operator replacement for charge in the φ representation $\hat{Q}/2e = \hat{N} \rightarrow i\partial/\partial\varphi$. For our particular devices, we are mainly concerned with the phase representation.

$$\hat{H} = -4E_c\frac{\partial^2}{\partial\varphi^2} + E_J(1 - \cos\hat{\varphi}) \tag{4.30}$$

where $E_c = \frac{e^2}{2C}$. The wavefunction for this Hamiltonian depends on the relative strengths of E_c and E_J. We can assume the wavefunction has the form of a Bloch function $\Psi(\varphi) = \sum u(\varphi)e^{ik\varphi}$. For the case of $E_J \gg E_c$, we can approximate the Hamiltonian as a particle confined to a series of harmonic oscillator potentials. The ground state is then a series of narrowly peaked wavefunctions $\Psi(\varphi)$, with a number of higher states in this potential minimum resembling the excited states of a harmonic oscillator,

$$\Psi(\varphi) \sim \exp(-\varphi^2/(2\sigma)^2) \tag{4.31}$$

where σ is the rms spread in phase φ, whose value is chosen to minimize the average energy of the system. When $E_c \gg E_J$, the second term in Eq. (4.29) can be

treated as a perturbation that couples charge eigenstates. For the ground state we can approximate this as,

$$\Psi(\varphi) \sim \cos\varphi \tag{4.32}$$

We find then that there are two regimes to our circuit, the phase and charge regime [60]. Devices fabricated in either the charge or phase regime have been studied to experimentally verify the competition between Josephson and charging effects. We have as our two basis states, the phase states and its Fourier transform, the charge states. The phase eigenfunction is the convenient choice for describing junctions dominated by the phase-dependent coupling E_J just as the number N eigenfunctions are useful for discussing junctions in the charging regime.

Proposals to use Josephson systems as qubits have up to now mostly concentrated on three basic types of implementations, the "Cooper-pair box" ("charge qubit") and the "rf SQUID ring" / "persistent current (PC) qubit" ("flux qubit") or large Josephson junction ("phase" qubit). In the first case, a small superconducting island is connected to a superconducting reservoir by a Josephson junction. At a suitable bias voltage on the island relative to the reservoir, these states are degenerate in the absence of Josephson tunnelling, but such tunnelling splits the two states. The eigenstates correspond to states with N and $N+1$ Cooper pairs on the island. In this system the most serious source of decoherence is believed to be fluctuations in the biasing voltage ("charge noise"). In the second implementation, the "flux qubit", the system is a superconducting loop interrupted by one or more Josephson junctions, typically of dimensions $\sim \mu$m, and biased by a suitable external magnetic flux. The eigenstates of this system correspond to different values of the circulating current and hence of the total flux enclosed in the loop. Fluctuations of the external flux ("flux noise") are a major source of decoherence in this system. We finally consider a large Josephson junction, the "phase qubit", consisting of a current biased Josephson junction with relatively large area $\approx 10 \times 10\,\mu\text{m}^2$. Near an applied current slightly less than I_c, the eigenstates of the system correspond to states of differing voltage

state tunnelling probabilities. The most serious source of decoherence for this system is fluctuations from the current source used to bias the junction.

4.3 Persistent Current Qubit System

The Persistent Current (PC) qubit is a promising candidate for a superconducting flux qubit. We discuss the PC qubit, reviewing previously developed theory, then follow with a discussion of the flux meter reading out the qubit - a DC SQUID magnetometer.

4.3.1 PC Qubit

The persistent current (PC) qubit proposed by Mooij, Orlando *et al.* [25, 26] was fabricated in a regime where the Josephson energy was significantly larger than the charging energy ($E_J/E_C \simeq 100$) meaning phase is the well defined quantum variable. The circuit, shown in Fig. 4-6, consists of a $\sim 10\,\mu$m sized loop interrupted by three Josephson junctions and inductively coupled to a superconducting magnetometer. Two of the Josephson junctions have equal Josephson coupling energy E_J while the third (weak) junction has Josephson energy αE_J where $0.5 < \alpha < 1$.

If we apply a small dc magnetic field through a superconducting loop (with or without junctions), we can induce a dc persistent current to flow. Under suitable device parameters, a three-junction loop will have two stable states corresponding to persistent currents of opposite direction when an applied magnetic field or frustration f (in units of Φ/Φ_0) is near a half integer value of a flux quanta Φ_0. If we ignore the self induced flux of the loop, fluxoid quantization states that the phases across the junctions are constrained by the applied flux through the loop. We find therefore,

$$\varphi_1 - \varphi_2 + \varphi_3 = -2\pi f \tag{4.33}$$

leaving φ_1 and φ_2 as independent dynamical variables.

Plotting the two independent variables φ_1 and φ_2, we find the Josephson potential

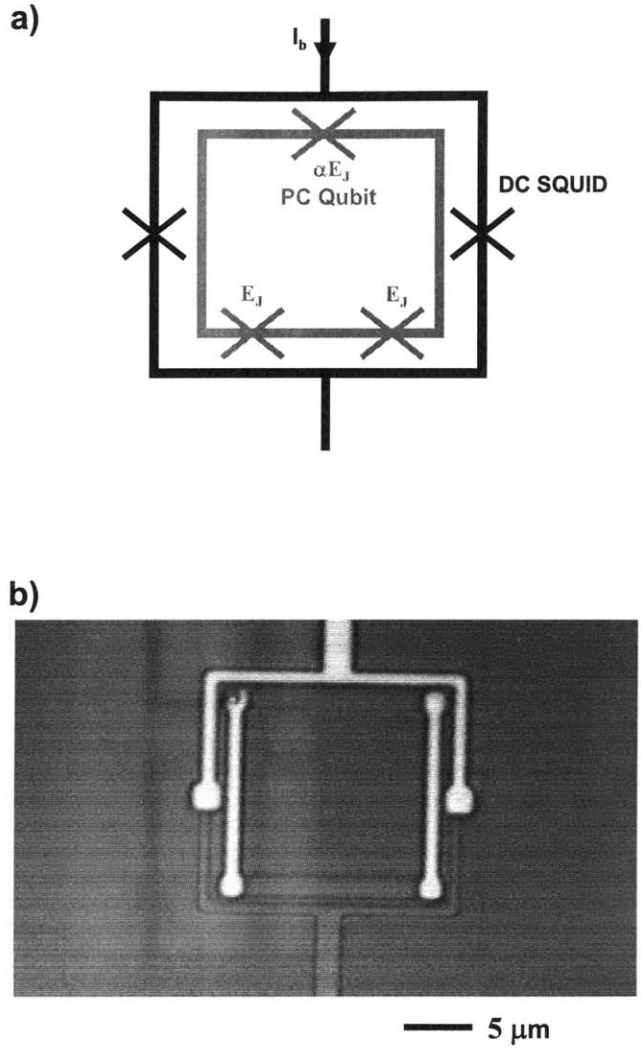

Figure 4-6: Persistent Current Qubit inductively coupled to a DC SQUID. a) Schematic of the PC qubit circuit. b) Image of the device fabricated at MIT Lincoln Laboratory Nb trilayer process. The three corners of the loop contain a junction while the fourth (upper left) contains a via.

energy U_J landscape is given by a two-dimensional coordinate space,

$$U_J(\varphi_1, \varphi_2) = E_J[2 + \alpha - \cos\varphi_1 - \cos\varphi_2 - \alpha\cos(\varphi_1 - \varphi_2 + 2\pi f)] \tag{4.34}$$

If we let $\alpha \simeq 0.8$, the effective potential is a periodic pattern of local double wells as shown in Fig. 4-7a. Large potential barriers separate the double wells whereas the potential barrier between the wells is sufficiently weak such that tunnelling between levels can occur. The system can be viewed as a particle in the Josephson potential with the charging energy E_c as its kinetic energy. Shown in Fig. 4-7b, by controlling the externally applied magnetic field near $f = \frac{1}{2}$, one can control the energy of the two minima.

Let us determine the Hamiltonian of our PC qubit. Defining phase coordinates $\varphi_p = (\varphi_1 + \varphi_2)/2$ and $\varphi_m = (\varphi_1 - \varphi_2)/2$, the Hamiltonian of the PC qubit loop can be written as,

$$\hat{H} = \underbrace{\frac{1}{2}\frac{P_p^2}{2M_p} + \frac{1}{2}\frac{P_m^2}{2M_m}}_{\text{Charging energy}} + \underbrace{E_J[2 + \alpha - 2\cos\varphi_p\cos\varphi_m - \alpha\cos(2\pi f + 2\varphi_m)]}_{\text{Josephson energy}} \tag{4.35}$$

where the momenta is written as $P_p = -i\hbar\partial/\partial\varphi_p$ and $P_m = -i\hbar\partial/\partial\varphi_m$. The mass terms depend on the capacitance C of the junctions and are defines as $M_p = 2C(\Phi_0/2\pi)^2$ and $M_p = 2C(1 + 2\alpha)(\Phi_0/2\pi)^2$. We have ignored the energy associated with the self-inductance L_q of the qubit loop in our Hamiltonian. Calculations have been performed to verify that for sufficiently small self-inductance of the qubit loop L_q, its effect can be ignored [63]. The energy bandstructure of the PC qubit, near $f = 1/2$, is shown in Fig. 4-8.

At the appropriate applied frustration f, we find the system has two low eigenenergies that are well separated from higher energy states (shown in Fig. 4-9a). Near $f = \frac{1}{2}$, theoretical results show that one can approximate the Hamiltonian of our circuit as a two level system given by [25, 64],

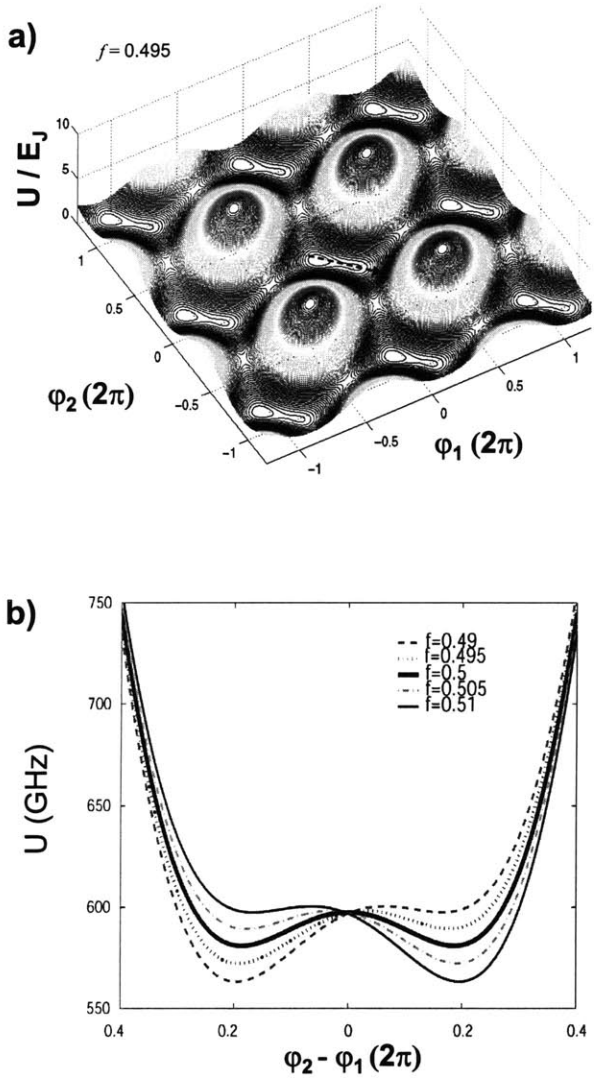

Figure 4-7: a) Josephson Energy Phase space near applied field $f = 1/2$ ($f = 0.495$) plotted as a function of φ_1 and φ_2. The Josephson energy potential consists of a periodic series of double well potentials. b) Energy along the trajectory indicated by the arrow. A unit cell contains two local minima. By varying the frustration, the double well potential configuration changes.

$$\hat{H} = -\frac{1}{2}(\varepsilon\sigma_z + \Delta\sigma_x) \tag{4.36}$$

where σ_z and σ_x are Pauli spin matrices described previously. We define Δ as the tunnel splitting at $f = \frac{1}{2}$. The energy bias ε is given by:

$$\varepsilon = I_p\Phi_0\left(f - \frac{1}{2}\right) \tag{4.37}$$

where I_p is the circulating current in the qubit. The system has for its two lowest eigenenergies $E_\pm$,

$$E_{-,+} = \mp\frac{1}{2}\sqrt{\Delta^2 + \varepsilon^2} \tag{4.38}$$

If Δ/ε is small, the eigenstates of H are nearly eigenstates of σ_z corresponding to states in which the system is localized in one well or another. At $f = \frac{1}{2}$, we expect degeneracy between the two states in the absence of quantum coherence. For sufficient coherent tunnelling, the eigenstates of the system $|\Psi_+\rangle$ and $|\Psi_-\rangle$ are the symmetric and anti-symmetric superpositions of the left $|0\rangle$ and right $|1\rangle$ well states

$$|\Psi_+\rangle = \frac{1}{\sqrt{2}}(|0\rangle - |1\rangle) \tag{4.39}$$

$$|\Psi_-\rangle = \frac{1}{\sqrt{2}}(|0\rangle + |1\rangle) \tag{4.40}$$

The expectation value of the circulating current is calculated to be $\langle I_{circ}\rangle = \partial E/\partial f$ [26]. For the two lowest energy states, we find the circulating currents will be of opposite direction (shown in Fig. 4-9b).

For millikelvin temperatures and low environmental noise, we expect damped coherent oscillations between the two potential wells. When the energy levels between wells are equal, the mixing of the two energy states between wells produces an energy gap Δ. We explain this gap by the following [65]: As the particle tunnels between the two potential wells, it lowers its kinetic energy by spreading its wavefunction over both wells. As a result the mixed ground state is shifted down by $\Delta/2$ with respect

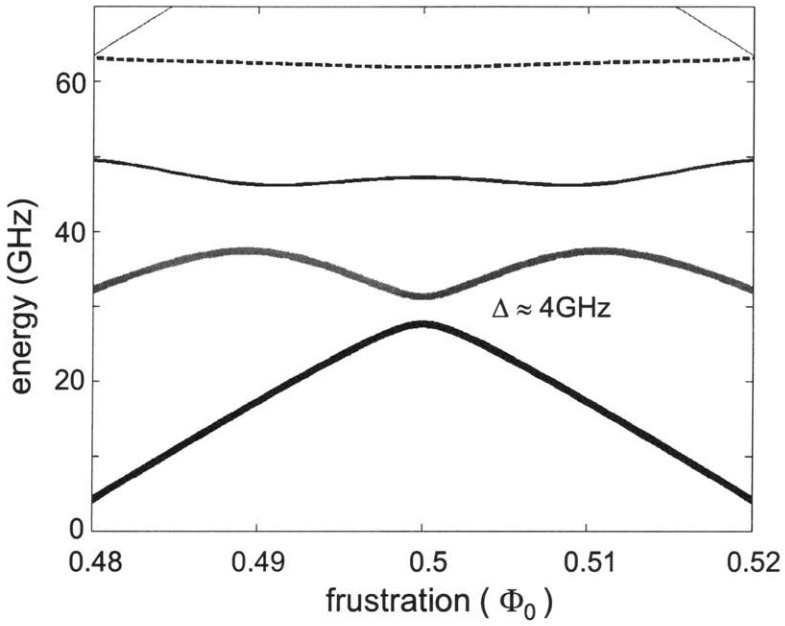

Figure 4-8: Eigenenergies of first four energy levels of PC qubit near f=1/2. Parameters are for: $E_J = 1.6\,\text{meV}$, $E_c = 12.5\,\mu\text{eV}$, $\alpha = 0.6$. At $f = 1/2$, the energy splitting between the ground state (black) and first excited state (gray) is $\Delta \approx 4\,\text{GHz}$.

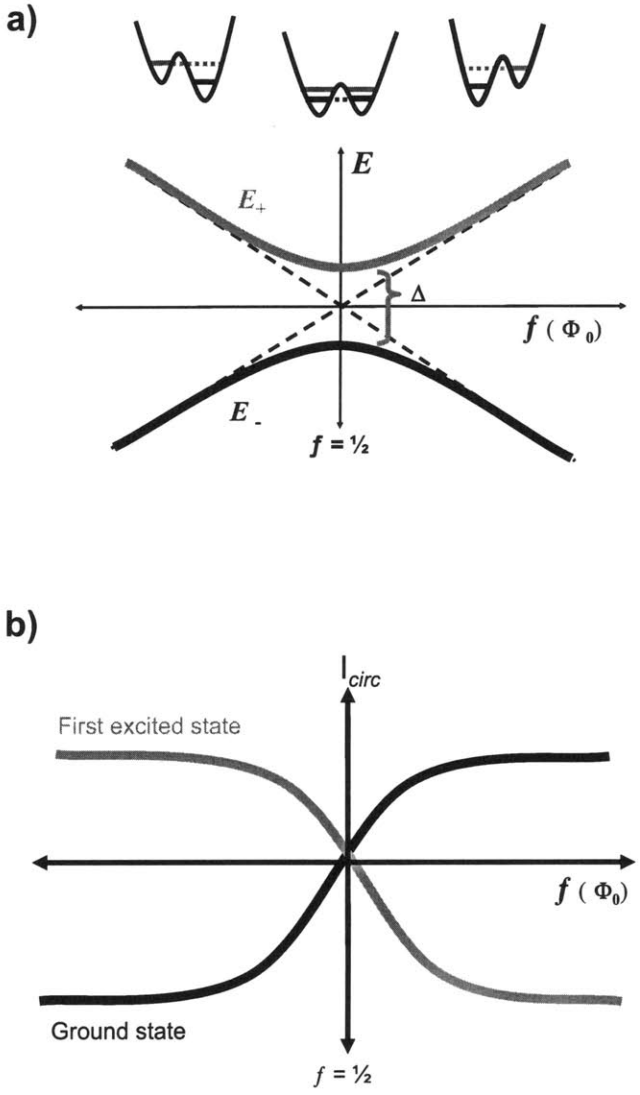

Figure 4-9: a) Two-level system. Ground state energy (black) and first excited state energy (gray) of the PC qubit loop as a function of applied frustration f. Classically (dashed lines), we expect a degeneracy point at $f = \frac{1}{2}$. With sufficient tunnel coupling, the energy levels are separated by a gap Δ. Shown above are the double well potentials (with two lowest energies indicated) at given applied frustrations. b) The circulating current of the PC qubit as a function of frustration for the ground state (black) and first excited state (gray).

to the individual wells. The corresponding anti-symmetric state is slightly higher in energy ($\Delta/2$) resulting in an excitation gap of Δ. We define regions where the energy levels between the double wells line up and an energy gap occurs as a level crossing or a resonant tunnelling event.

Unfortunately measuring this energy gap or observing a superposition of macroscopic states is extremely difficult due to decoherence by the environment. We require the eigenenergy splitting be much larger than the thermal energy fluctuations of the system ($k_BT \ll \Delta$). Although it is unclear that the thermal energy fluctuations experienced by the qubit are well-approximated by k_BT, it should certainly accepted that k_BT is a bound. At T = 1 K, the thermal energy is roughly 20 GHz. Therefore, an experiment at temperature T = 10 mK is subject to thermal energy fluctuations of roughly $k_BT \sim 0.2$ GHz. Since the device temperature is often significantly higher than the phonon temperature, we would ideally like at least a factor 10 higher in the energy splitting at $f = 1/2$ ($\Delta \geq 10k_BT$). Thus, we nominally desire $\Delta \sim 1$ GHz to achieve a large initial population (i.e., approach unity occupation probability) in the qubit ground state at $f = 1/2$.

Dephasing and Relaxation within the Spin-Boson Model

The major problem in superconducting circuits is the interaction of the surrounding environment with the quantum components, leading to irreversible loss and transfer of information or decoherence. Critical to an effective quantum computing is the extent to which the phase relation between the $|0\rangle$ and $|1\rangle$ components of the wave function is preserved. By the phenomenon of decoherence, any irreversible interaction of a quantum-mechanical system with its environment destroys the phase relations between the quantum states. The effect of decoherence in randomizing the relative phase is usually quantified by the dephasing time τ_φ, with the inverse given as the dephasing rate Γ_φ. In addition to τ_φ, it is useful to define the energy relaxation time τ_{relax} defined as the $1/e$ time to relax to its ground state from the first excited state. The inverse of the energy relaxation time is given as Γ_{relax} [66]. In general, dephasing occurs on a much faster time scale than relaxation.

The relaxation time and dephasing time for our PC qubit system is determined by applying a spin-boson model. The spin-boson model considers a dissipative two-level system - the environment is modelled as a bath of LC oscillators coupled to the modes of the quantum system. The influence of the oscillator bath on the qubit is described by the environmental spectral density function $J(\omega)$ given as

$$J(\omega) = \frac{\pi}{2} \sum_i \frac{c_i^2}{C_i \omega_i} \delta(\omega - \omega_i) \tag{4.41}$$

where c_i is the coupling strength to the i-th oscillator and ω_i is the resonant frequency of the i-th oscillator.

The relaxation rate Γ_{relax} and dephasing rate Γ_φ are then determined by the environmental spectral density function and the energy level separation δE between the ground and first excited state by,

$$\Gamma_{relax} = \tau_{relax}^{-1} = \frac{1}{2}\left(\frac{\Delta}{\delta E}\right)^2 \left[J(\omega) \coth\left(\frac{\hbar\omega}{2k_B T}\right)\right]_{\omega=\omega_0} \tag{4.42}$$

$$\Gamma_\varphi = \tau_\varphi^{-1} \simeq \frac{1}{2}\tau_{relax}^{-1} + \frac{1}{2}\left(\frac{\epsilon}{\delta E}\right)^2 \lim_{\omega\to 0}\left[J(\omega) \coth\left(\frac{\hbar\omega}{2k_B T}\right)\right] \tag{4.43}$$

In particular, we are interested in the ohmic dissipation of our quantum system, corresponding to a spectrum

$$J(\omega) = \frac{\pi}{2}\alpha\hbar\omega \tag{4.44}$$

which is linear at low frequencies up to some cutoff frequency. The dimensionless parameter α describes the dissipation or damping of our system and is inversely proportional to the quality factor Q,

$$\alpha_L \propto 1/Q \tag{4.45}$$

if we assume that the environment can be modelled as an ohmic bath, then we can estimate the decoherence times of a PC qubit in which the qubit states are those of opposite circulating current [14, 20, 26]. The energy relaxation and phase decoherence

times are then given in the spin-boson model for an ohmic environment by [8, 66]

$$\Gamma_{relax} = \tau_{relax}^{-1} \simeq \frac{\pi \alpha_L \delta E}{\hbar} \sin^2 \eta \coth\left(\frac{\delta E}{2k_B T}\right) \tag{4.46}$$

$$\Gamma_{\varphi} \simeq \tau_{\varphi}^{-1} \simeq \frac{1}{2}\tau_{relax}^{-1} + \frac{2\pi \alpha_L k_B T}{\hbar} \cos^2 \eta \tag{4.47}$$

where the mixing angle $\eta = \tan^{-1}(\Delta/\delta E)$.

Although extremely instructive, the spin-boson model is a simple model to analyze the decoherence in our system. A general method to study qubit decoherence by environmental noise has also been developed [67]. Other experimental environments, such as influence of the SQUID readout device [68, 69], have been considered to determine the noise coupling into the system. The measurement efficiency and measurement-induced decoherence of the readout device has been investigated.

4.3.2 DC SQUID Magnetometer

The success of the macroscopic quantum experiments is enhanced by the convergence of two superconducting technologies, a device exhibiting macroscopically observable quantum coherence and a sensor exhibiting nearly ideal sensitivity to variations in magnetic flux. For our system, a DC SQUID (Superconducting Quantum Interference Device) magnetometer is used to measure the magnetic flux produced by the circulating current in the PC qubit. SQUIDs are natural candidates as magnetometers since they are extremely sensitive detectors of magnetic flux and can be fabricated in the same process as the qubit [56]. For our system, the SQUID uses unshunted junctions that are extremely underdamped, in order to minimize decoherence of our quantum system. For high effective shunt resistances, we acquire lower noise from the SQUID in the superconducting regime (when no measurement is performed).

A schematic of a DC SQUID is given in Figure 4-10. The SQUID consists of two Josephson junctions connected in parallel in a superconducting loop. If we ignore the resistance and self-capacitance of the two junctions, the total current I_c through the SQUID is given by [53]

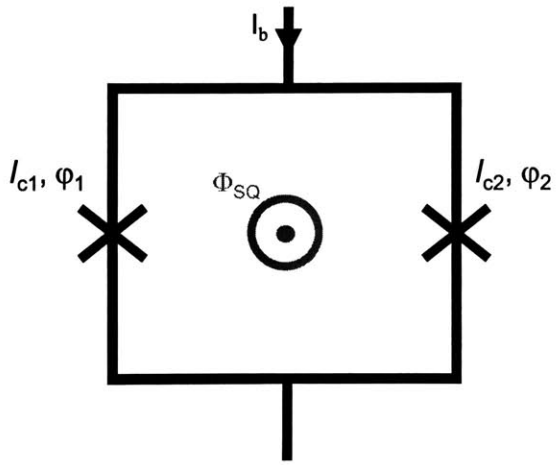

Figure 4-10: Circuit diagram of the DC SQUID. The DC SQUID consists of two Josephson junctions connected in parallel in a superconducting loop (I_{c1}, φ_1, and I_{c2}, φ_2 are the critical current and phase difference across the junctions respectively. A bias current I_{bias} is ramped to determine the total flux Φ_{SQ} threading the SQUID loop.

$$I_c' = I_{c1} \sin \varphi_1 + I_{c2} \sin \varphi_2 \tag{4.48}$$

where I_{c1}, φ_1, and I_{c2}, φ_2 are the critical currents and phase difference of the two junctions respectively. If we let the two critical currents I_{c1} and I_{c2} be equal ($I_{c1} = I_{c2} = I_c$) and impose the fluxoid quantization condition

$$\varphi_1 - \varphi_2 = -2\pi\Phi_{SQ} \tag{4.49}$$

we then obtain

$$I_c' = 2I_c \cos(\pi\Phi_{SQ}) \sin(\varphi_1 + \pi\Phi_{SQ}) \tag{4.50}$$

where Φ_{SQ} is the total flux through the SQUID loop given by,

$$\Phi_{SQ} = \underbrace{f}_{\text{applied flux}} + \underbrace{L_{SQ} I_c \sin(\pi\Phi_{SQ}) \cos(\varphi_1 + \pi\Phi_{SQ})}_{\text{flux from self-inductance}} + \underbrace{M I_{circ}}_{\text{flux produced by the PC qubit}} \tag{4.51}$$

where L_{SQ} is the self-inductance of the SQUID loop, M is the mutual inductance between the SQUID loop and PC qubit, and I_{circ} is the circulating current in the PC qubit. The switching current I_{sw} value is found to have a periodic modulation for an externally applied magnetic field (Shown in Figure 4-11). For the DC SQUID, we define the parameter β_L,

$$\beta_L = 2\pi L_{SQ} I_c / \Phi_0 \tag{4.52}$$

which determines the depth of modulation of the switching current. For maximum switching current modulation, we require β_L to be small $\beta_L < 1$. For our DC SQUID magnetometer, $\beta_L \simeq 0.9$. If we ignore the inductance of the SQUID loop, we find

$$I_c' = 2I_c |\cos(\pi\Phi_{SQ})| \tag{4.53}$$

Shown in Fig. 4-11a, the critical current I_c' is periodic with the applied magnetic flux Φ_{SQ}. The small inductance of the PC qubit produces a small $MI_{circ} \leq 10^{-2}\,\Phi_0$ flux signal. The flux signal in the SQUID is measured by ramping the bias I_{bias} current through the device and recording the current level I_{sw} where the SQUID jumps from the superconducting branch to the finite voltage (dissipative) branch. Escape to the voltage state is a stochastic process even when the external flux through the SQUID is fixed. This results in a large spread in I_{sw} in a histogram of switching events. Although we measure the total flux Φ_{SQ} through the SQUID, we are able to measure changes in the state of the PC qubit, due to a change in circulating current near applied frustration $f = 1/2$. The resulting qubit signal is a $\approx 100\,\text{nA}$ "step" like feature within the SQUID modulation curve as shown in Figure 4-11b.

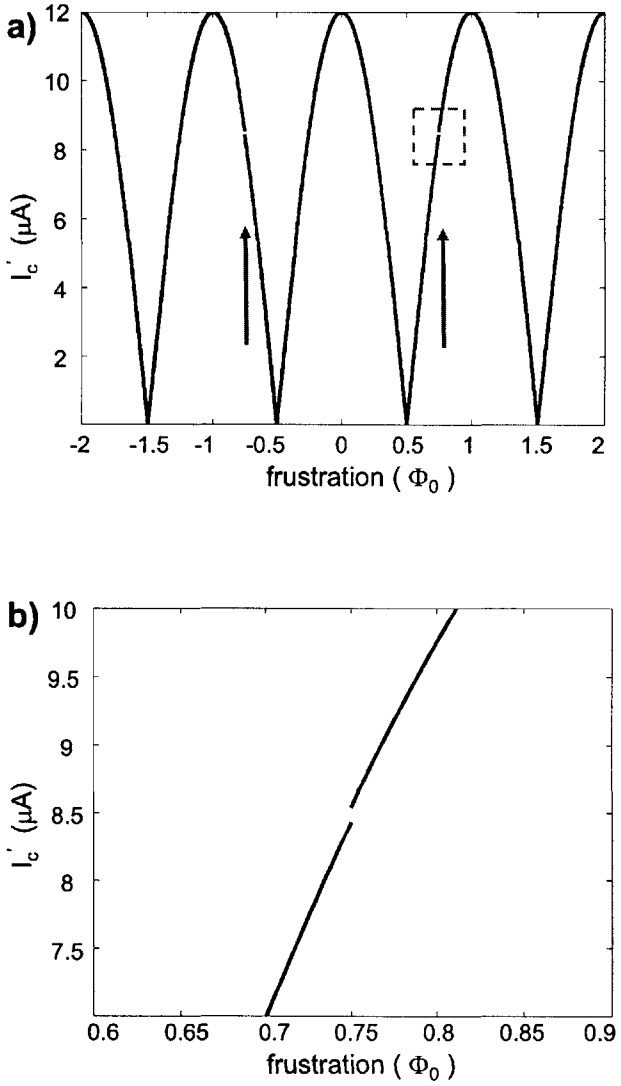

Figure 4-11: Simulation of the DC SQUID modulation assuming the SQUID self-inductance $L_{SQ} = 0$ and critical current I_c' of the SQUID is $12\,\mu$A. The arrows indicate the $3\Phi_0/2$ periodic qubit step signal and dashed box highlights a PC qubit step. For our parameters, we assume $MI_p \approx 10^{-2}\Phi_0$ b) Blow-up of the PC qubit step signal ($\sim 100\,$nA) due to the change in circulating current of the PC qubit.

Chapter 5

Experimental Realization of a Nb Persistent Current Qubit

It is valuable to investigate Nb-based Josephson devices as potential qubits. Nb has advantages over other technologies - it has a more mature fabrication capability and can be incorporated with existing RSFQ technology. Initial measurements on the PC qubit were performed at the Delft University of Technology with $Al/AlO_x/Al$ junctions fabricated in a shadow evaporation technique [14]. Spectroscopy measurements demonstrated a superposition of macroscopic quantum states in the Al qubit. Coherent temporal oscillation experiments have determined the energy relaxation time and dephasing time of the Al qubits to be $\sim 900\,\mathrm{ns}$ and $\sim 20\,\mathrm{ns}$ respectively [20]. Previous methods to determine dissipation in these devices are applicable at relatively high temperatures ($T \approx 0.55\,K$) [70] or rely on indirect measurements of switching probabilities [71, 72]. For Nb based structures, experimental investigation of decoherence is sparse due to the challenges of both fabricating Nb devices of sufficient quality and the difficulty in the time resolution of the measurement. Quantifying the dissipation in Nb devices is extremely useful because it indicates whether the dissipation is acceptable to make error-tolerant computation feasible.

The following chapter discusses experimental progress in $Nb/Al/AlO_x/Nb$ Josephson junction qubits measured at dilution refrigerator temperatures, with an emphasis on determining the energy relaxation time τ_d between macroscopic quantum levels.

The low-temperature experimental setup, which is vital to minimizing noise and decoherence in our system, is detailed and the measurement process is discussed. The main aspect of the research involves off-chip microwave spectroscopy experiments to probe the energy bandstructure of the system. We can induce transitions between the two distinct energy levels of the system by applying low-amplitude microwaves resonant with the energy level separation. Time-resolved measurements of the intrawell energy relaxation time τ_d between macroscopic quantum levels are presented [73]. From the low-temperature measurements, one can infer a decoherence time for these Nb devices. The measured relaxation times ($\approx 24\mu$s) suggest a strong potential for quantum computing employing Nb-based superconducting circuits.

Initial measurements on the Nb PC qubit (fabricated at MIT Lincoln Laboratory) were performed at ^{3}He refrigerator temperatures. At $T \simeq 300\,\mathrm{mK}$, time-ordered measurements of the two states of the qubit probed the thermal activation rate over a potential barrier [74, 75]. Using a model that incorporates thermal activation, the system parameters ($E_J \sim 4\,\mathrm{meV}$ and $E_c \sim 2\,\mu\mathrm{eV}$) were extracted and a quality factor Q for the Nb PC qubit was estimated to be $\sim 3 \times 10^5$. The flux biasing of the devices effectively transformed the impedance seen by the qubit by a factor of $(3L_J/M)^2$, where $L_J = \Phi_0/(2\pi I_c)$ is the Josephson inductance of each of the three junctions in the qubit. The results of the quality factor Q are in approximate agreement with independent measurements of the subgap resistances of MIT Lincoln Laboratory Nb Josephson junctions ($R_{subgap} \approx 10\,\mathrm{M}\Omega$) at low temperatures ($\mathrm{T} \simeq 1\,\mathrm{K}$). The large Q value for these devices show great promise for Nb-based qubits.

At sufficiently lower temperatures ($\mathrm{T} \simeq 20\,\mathrm{mK}$), where thermal activation is negligible, macroscopic resonant tunnelling or DC level spectroscopy between quantum levels have been observed in Nb PC qubit structures [76, 77]. Depending on the external parameters, the system may have multiple quantum energy levels in one of the two wells, where each level has approximately the same magnetization. The quantum levels are measured by observing resonant tunnelling between the two wells of the double well potential configuration. Fig. 5-1 are plots of the qubit state probability (theory and experiment) vs. frustration when the SQUID magnetometer current bias

is ramped at two different rates (a) 4 mA/ms and (b) 0.8 mA/ms. The probability that the state will transition from **1** to **0** depends on the tunnelling rate and the time for the system to remain in the level crossing region. The rate of resonant transition from the lowest energy level in one well to a high energy level in another well was determined theoretically for a double well potential configuration [78]. The slower ramp rate (0.8 mA/ms) results in a higher probability that the qubit transitioned to the **1** state, which is made clear by the developing peaks marked by the vertical lines. Since the flux bias which the qubit sees is constantly changing (due to the changing circulating current in the DC SQUID as the bias current is ramped), the sharp peaks in the state probability indicate the qubit has passed through an energy bias which gives a high tunnelling rate. It also shows that it spends a significant amount of time at that level alignment only for certain external flux biases. Thus, when the current ramp rate is slower, the indicated peaks are expected to increase, which is consistent with experiment. By measuring the width and height of the tunnelling peaks as a function of the SQUID ramp rate, the fitted value of the intrawell relaxation time τ_d between macroscopic quantum levels has been determined to be of order $\sim 1 - 10\,\mu$s.

5.1 Nb PC Qubit Sample Parameters

We begin with the overall parameters of our Nb PC qubit device and DC SQUID flux meter (sample parameters are summarized in Table 5.1 and 5.2). The PC qubit has an area $16\times16\,\mu\text{m}^2$ and the DC SQUID loop has an area $20\times20\,\mu\text{m}^2$. The linewidths of the loop are approximately $\sim 1\,\mu$m wide. The ratio of SQUID to PC qubit area was approximately 3/2, such that the change in flux signal from the qubit would occur at the most sensitive region of the SQUID's $\langle I_{sw}\rangle$ modulation curve. The self-inductance of the loops were calculated using FASTHENRY, a three-dimensional inductance extraction program [79]. We estimate the self-inductance of the PC qubit loop and DC SQUID loop to be 40 pH and 50 pH respectively and the mutual inductance M between the two loops to be 20 pH. From measurements of step regions in the DC SQUID modulation curve, the mutual inductance M is estimated to be 25 pH [76].

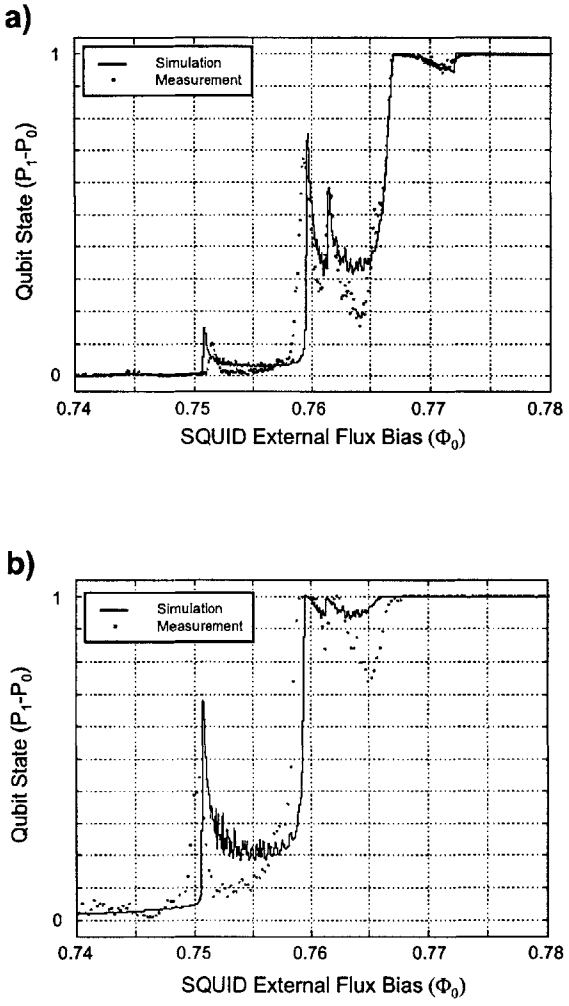

Figure 5-1: The qubit state probability when the SQUID is ramped at a rate of a) 4 mA/ms and b) 0.8 mA/ms. The solid lines correspond to the theoretical model, while the solid circles are experimental data points. The slower ramp rate results in a higher probability that the qubit will transition to the 1 state, as is made clear by the growing peaks marked by the vertical lines.

The two junctions of the SQUID had nominal junction sizes of $1.2\times1.2\,\mu m^2$ and the qubit had junction sizes of $0.5\times0.5\,\mu m^2$ for the smaller junction and $0.6\times0.6\,\mu m^2$ for the two larger junctions, giving $\alpha \simeq 0.7$. The current density J_c of the sample was $\sim 400\,A/cm^2$. The total critical current of the DC SQUID I' was measured to be $12\,\mu A$ and the critical current of the PC qubit was estimated from the area of the smaller junction and current density J_c to be 1-2 μA. We therefore estimate the maximum flux signal change from the three junction loop to be $MI_{circ} \simeq 10^{-2}\,\Phi_0$. The SQUID was shunted with on-chip 2 pF capacitors in order to increase the effective mass C of the SQUID, thereby lowering its LC resonant frequency. The shunt capacitor is formed by the Nb base electrode and wiring layers as the capacitor plates and the SiO_2 insulating layer for the dielectric. From the given sample parameters, a bandstructure of the qubit (Shown in Fig. 5-2) is calculated, showing the level crossings of the system

.

Table 5.1: PC Qubit Sample Parameters

Qubit junction dimensions	$0.5\times0.5\,\mu m^2$ (small)
	$0.6\times0.6\ \mu m^2$ (large)
α	0.6
Loop area	$16\times16\,\mu m^2$
Loop Inductance	40 pH
Circulating Current	1-2 μA
E_J	2.1 meV $\approx$ 500 GHz
E_C	2-4 $\mu eV \approx$ 0.5-1 GHz
E_J/E_C	500-1000

Table 5.2: DC SQUID Parameters

DC SQUID junction dimensions	$1.1\times1.1\,\mu m^2$
Loop area	$20\times20\,\mu m^2$
Loop Inductance	50 pH
Total Critical Current I'	12 μA
β_L	0.2
Shunt Capacitance	2 pF
Mutual inductance M to qubit	20 pH

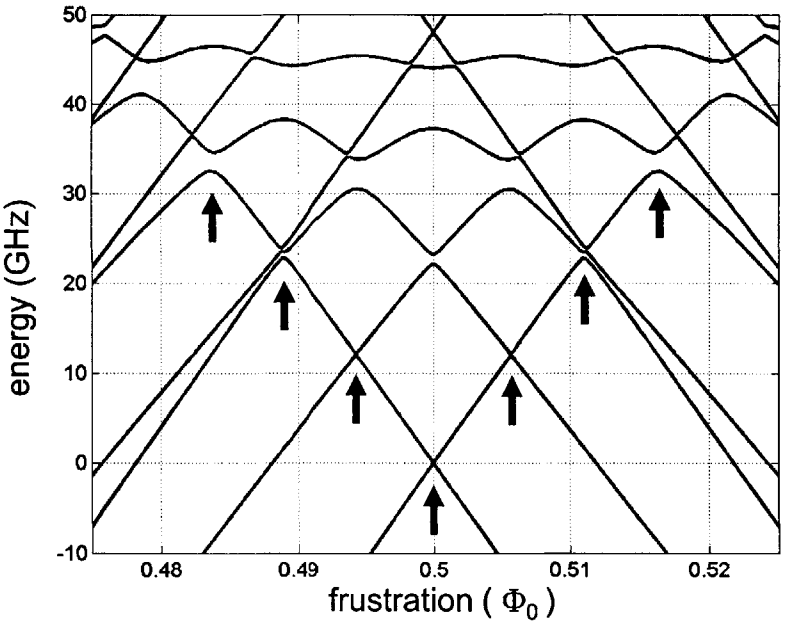

Figure 5-2: Energy band structure of PC qubit near f=1/2 for parameters given in Table 5.1. Note the tunnel splitting or level crossings occur at certain values of frustration f causing an energy "gap" between levels (indicated by arrows).

5.2 Experimental Implementation

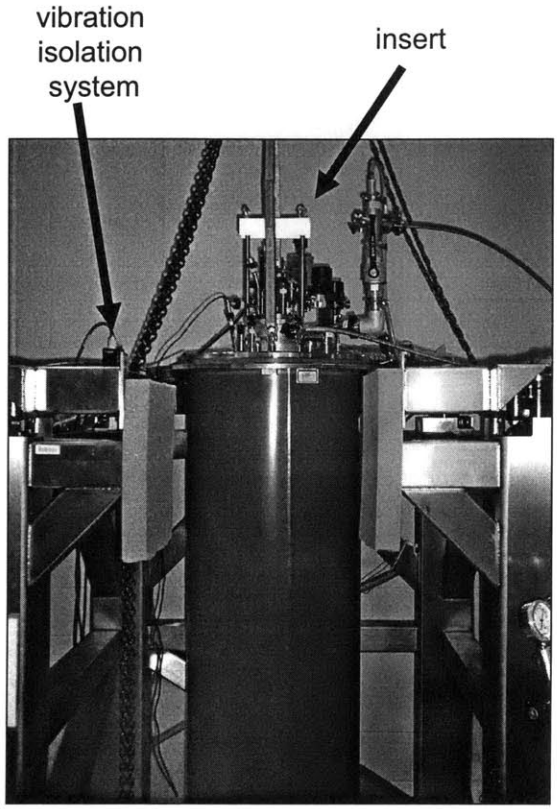

Figure 5-3: The dilution refrigerator floats on a vibration isolation table. Outside the inner vacuum can (IVC) sits a superconducting magnet and a 4-layer Cryoperm magnetic shield assembly.

Measurements on the PC qubit were performed in a standard Oxford Kelvinox 400 Dilution Refrigerator with a base temperature of ~10 mK. The temperature of the refrigerator is reached through evaporative cooling of concentrated ^{3}He into a heavier "dilute" phase within a mixing chamber. Shown in Fig. 5-3, the dilution refrigerator is supported by a vibration isolation table which minimized vibrational disturbances to the qubit system. All electrical connections were thermally anchored at various stages along the insert to reduce heat load on the mixing chamber and sample. Temperature measurements were determined using a Femtopower thermometry system, allowing

useful measurements to be made of the ruthenium oxide resistance sensors at the mixing chamber. The resistance measurements allowed for accurate thermometry measurements down to $\sim 20\,\mathrm{mK}$.

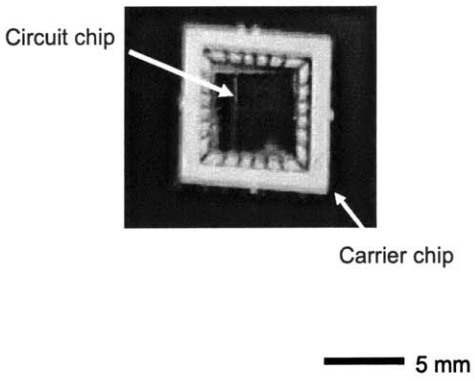

Figure 5-4: Circuit chip bonded within chip carrier. Gold wire bonds electrically connect the circuit chip to the carrier.

The sample was mounted on a chip carrier (shown in Fig. 5-4) that was enclosed in an oxygen-free-copper sample cell (Fig. 5-5), thermally anchored to the mixing chamber of the dilution refrigerator and magnetically shielded by four layers of cryoperm-10 μ-metal located outside the vacuum can but within the He-filled dewar. The μ-metal shielding was used to attenuate unwanted external magnetic field fluctuations by a factor $\sim 10^2$. Extensive effort was made to isolate the sample from external noise coming down the DC lines. All electrical leads connected to the SQUID were carefully filtered by Electromagnetic Interference (EMI) filters to the battery-powered room temperature electronics. *RC* filters at the 1 K stage were used to give cutoff frequencies of 10 kHz. We used stainless steel powder filters, located at the mixing chamber, to attenuate high frequency (-20 dB at 1 GHz) electrical noise. The powder filters consisted of three inch long copper tubes, filled with stainless steel powder, housing a 1 m long coiled wire. The copper sample cell was used to shield the sample from 50 mK blackbody radiation. Additionally, a copper shield, anchored

to the 50 mK stage, was used to shield the entire assembly from radiation at temperatures > 50 mK. Shown in Fig. 5-5, microwaves were injected to the qubit via a separate semirigid cryogenic coaxial cable with 20 dB attenuators at the 1 K pot and the mixing chamber. The microwave cables were terminated with a small ($\sim$ 1 cm) loop placed approximately 1 cm above the sample, inductively coupling microwave radiation to the qubit loop. The external magnetic field was applied to the sample by a superconducting solenoid wrapped around the vacuum can located in the liquid ^{4}He bath. The solenoid consisted of $\sim$100 turns of superconducting wire producing a field of ~ 20 mG per mA. A room temperature π filter on the magnet field lines was used to attenuate high frequency (-6 dB at 30 kHz) noise. A smaller solenoid, located within the sample cell, provided a means to produce pulsed state preparation magnetic fields to the sample. The entire low temperature assembly is shown in Fig. 5-6.

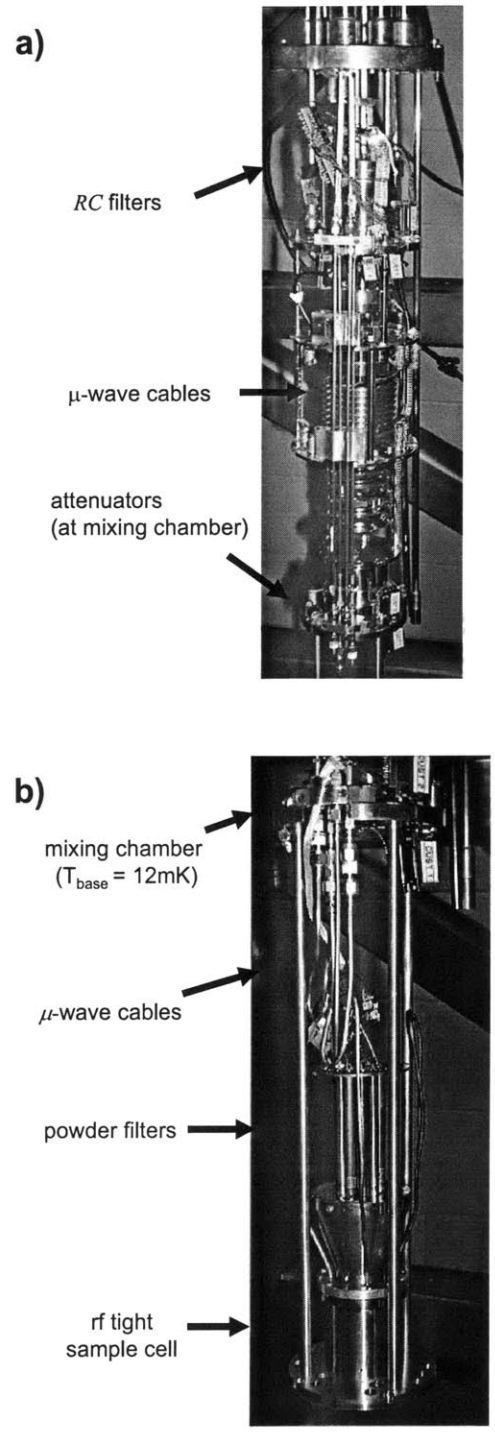

Figure 5-5: a) High frequency cable setup to irradiate microwaves to the qubit sample. Cables are attenuated at the mixing chamber and 1 K stage and directly enter the sample cell. b) The sample is mounted in a oxygen-free copper sample cell thermally anchored to the mixing chamber. The electrical lines for the bias and voltage leads are filtered by copper powder microwave filters to attenuate high frequency (> 1 GHz) noise.

5.3 Current Bias and Measurement Scheme

The electronics measurement setup is shown in Fig. 5-7. The bias current through the DC SQUID was generated by an Agilent 33250A Arbitrary Waveform Generator at a ramp rate between 100 Hz to 250 Hz. The voltage waveform generator was optically isolated from the sample using a BURR-BROWN ISO100 device and current biased through a 100 kΩ resistor. The bias current was ramped linearly to a current value slightly greater than the critical current of the DC SQUID then ramped down to a slightly negative offset value (- 0.1 V) to ensure the SQUID returned to its zero voltage state. When the device switched from the superconducting state, the resulting gap voltage ($V_{gap} = 3\,mV$) was amplified ($\times 100$) by a low-noise AD624 battery powered precision instrumentation amplifier. An Agilent 53132A Universal Counter recorded the time elapsed between a bias current of zero to its switching current value I_{sw}. The corresponding time elapsed τ_{switch} is then linearly proportional to the switching current value. The discontinuous switching current measurement method is presented in Fig. 5-8.

Typical switching current distributions consisted of 10^3 switching events taken at a fixed magnetic field. Shown in Fig. 5-9a is a typical Current-Voltage curve of the DC SQUID. The hysteretic $I-V$ is similar to that of a single junction of comparable critical current value. Below a certain switching current value, the SQUID is in the superconducting state. Ramping the bias current through the DC SQUID to a value greater than the switching current causes the SQUID to jump to its finite voltage state. Fig. 5-9b shows the corresponding switching current histogram of the DC SQUID at a fixed magnetic flux. The stochastic nature of the switching event creates a current distribution, similar to the switching current distribution of a single junction described in section 4.1.2.

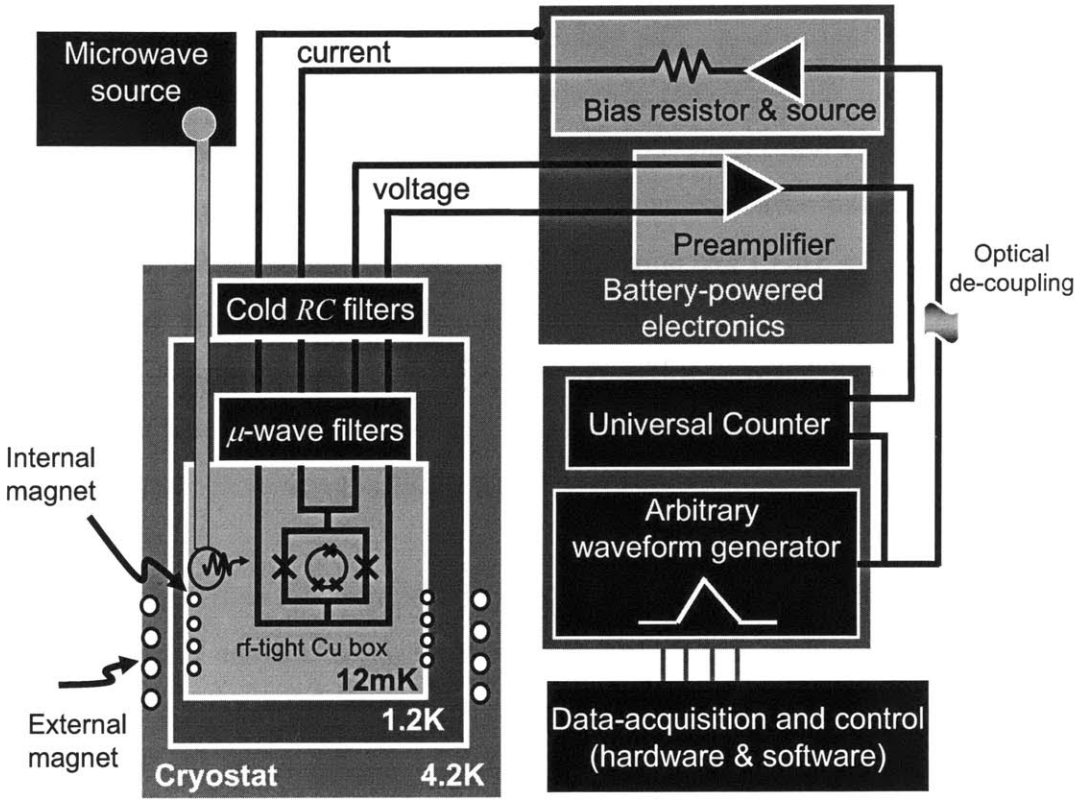

Figure 5-6: Experimental Measurement setup. The lines to the DC SQUID readout device are filtered at the 1 K stage and mixing chamber (12 mK). Using battery-powered electronics, the current through the SQUID is ramped and the switching current value is determined. The PC qubit is magnetically flux biased using an external magnet located in the 4 K bath. An internal magnet at the mixing chamber is used for state preparation. An external microwave source is used to irradiate the sample.

The applied magnetic field was swept in small increments ($\sim 0.03\,\mathrm{m}\Phi_0$) and at a given (fixed) magnetic field value, the average switching current values were recorded (Fig. 5-10). As described in Section 4.3.2, we observe a cosine-like periodic modulation of the average switching current vs. magnetic field. The current through the large magnet solenoid (located outside the IVC) was supplied by a Yokogawa 7651 Programmable DC Source. Near $\frac{3}{4}\Phi_0$ of the DC SQUID ($\frac{1}{2}\Phi_0$ for the PC qubit), we observed a small change in flux signal ($\sim 10^{-2}\,\Phi_0$) produced by the PC qubit (shown in Fig. 5-11a). The periodicity of the flux signal was observed to occur at $\frac{3}{2}\Phi_0$ of the DC SQUID as expected. The signal alternated between persistent current flowing to enhance then subtract from the applied magnetic field. From the histogram plots, one finds the PC qubit is in a bimodal state near $f = \frac{1}{2}$, a single measurement of the flux will find the state in either of the two circulating current states. For $f < \frac{1}{2}$ the lower switching current corresponds to state of the system in the lower potential well and for $f > \frac{1}{2}$, the higher switching current corresponds to the state of the system in the lower potential well. Overall, the system tended to remain in its lowest energy state.

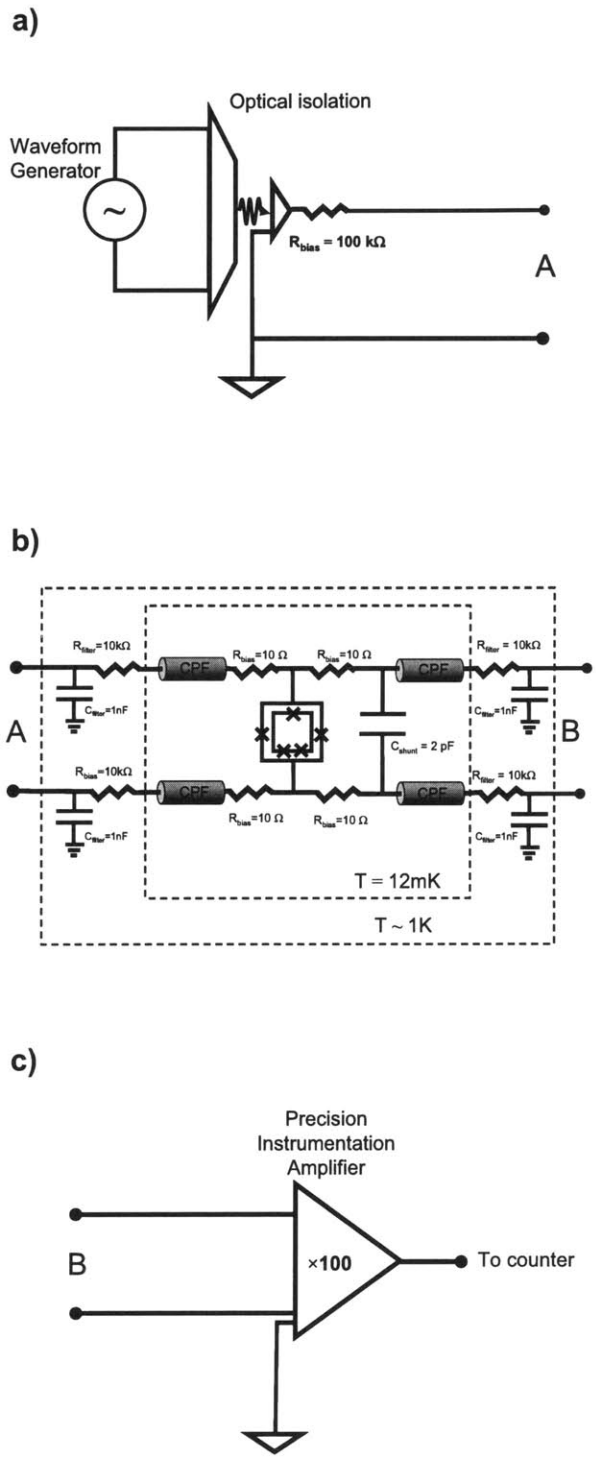

Figure 5-7: Circuit diagram for current bias and voltage readout. a) The waveform is generated using a waveform generator, optically isolated from the sample. b) Cables are filtered at the 1 K stage using *RC* filters and at the mixing chamber using copper powder filters (CPF). c) The resulting gap voltage is amplified (×100) using a precision instrumentation amplifier.

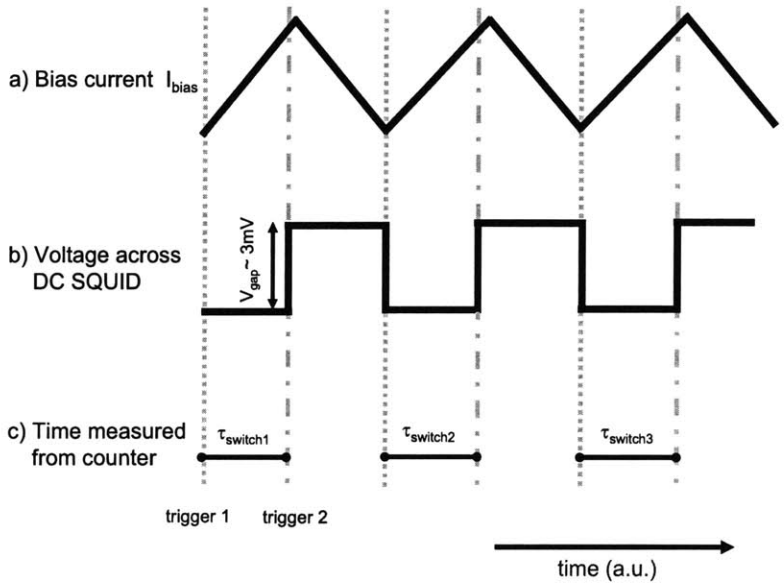

Figure 5-8: Discontinuous Switching current measurement. a) Current Bias is linearly ramped to a current slightly higher than the switching current level of the DC SQUID. At a given current value the dc SQUID switches to the finite voltage state. The switching current value is inferred from the time to switch measurement. This process is repeated $N \sim 10^3$ times for a given magnetic field.

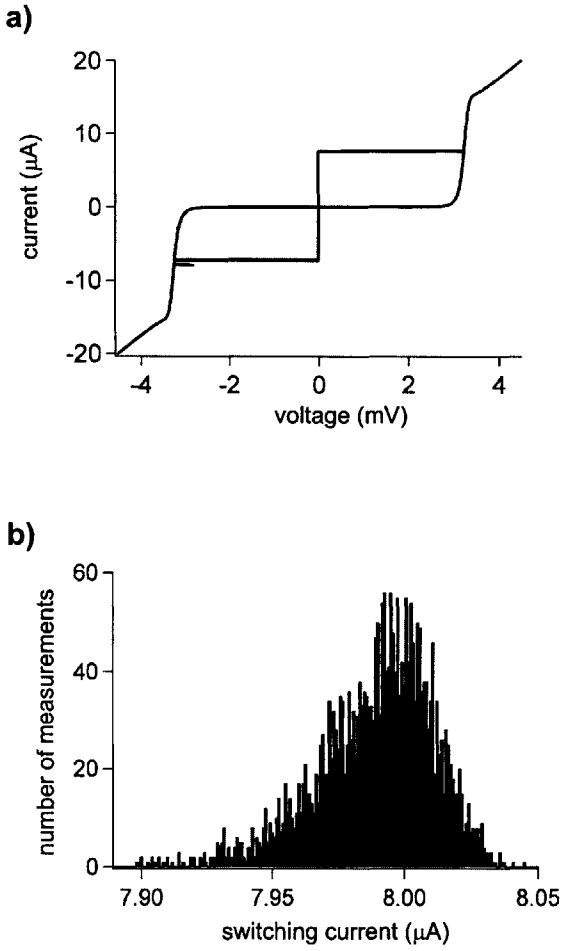

Figure 5-9: a) Current-Voltage Characteristics of the DC SQUID at T = 15 mK and zero magnetic field. b) Typical switching current histogram of DC SQUID consisting of 10^3 measurements.

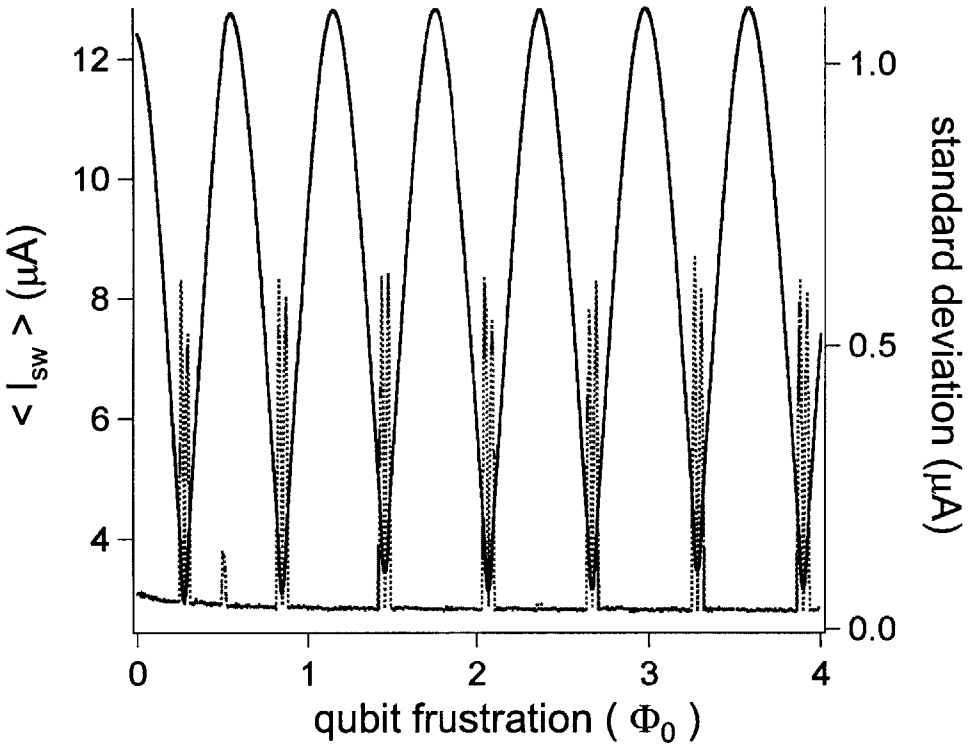

Figure 5-10: DC SQUID Average Switching current $\langle I_{sw} \rangle$ modulation (solid line) is periodic in applied magnetic field. Near f=1/2, we detect a change in the circulating current of the PC qubit, indicated by an increase in the switching current standard deviation (dashed line).

A detailed plot of the qubit "step" region (average and contour) is shown in Fig. 5-11. Fig. 5-11a is a plot of the average switching current value $\langle I_{sw} \rangle$ vs. frustration whereas Fig. 5-11b is a contour plot of the switching current distribution - each vertical segment is a switching current histogram and the gray scale represents the number of switching events. The qubit is initially prepared in the higher switching current branch using a state preparation pulse (detailed in next section). At certain frustrations, macroscopic tunnelling between adjacent wells is at a maximum. At these given level crossings, resonant tunnelling causes transitions to the lower switching current state, indicated by small population distributions in the lower switching current branch at $f \approx 0.49$, $f \approx 0.495$ and $f \approx 0.5$ (indicated with arrows in Fig. 5-11b). As described in Sec 5.1, previous work on Nb PC qubits investigated the resonant tunnelling event, or DC level spectroscopy, between macroscopic quantum levels [76].

5.4 Spectroscopy Measurements on PC Qubit

Off-chip spectroscopy of the qubit energy levels was achieved using microwave pulses to produce photon induced transitions or resonant transitions between quantum states. For each measurement trial (Fig. 5-12), we first prepared the qubit in a particular state (state $|1\rangle$) by tilting the double well potential. This was performed by applying an appropriate frustration via a $200\,\mu$s current pulse through the inner solenoid, to a regime where the system has a single well and then waited a sufficiently long time ($\sim 1\,$ms) for the system to relax to its ground state. We used an Agilent 33250A Function Generator to apply the magnetic field state preparation pulse to the sample. After the qubit had relaxed to its ground state, the potential was tilted back to the frustration where it was to be measured. At dilution refrigerator temperatures, the qubit will have a finite probability of remaining in state $|1\rangle$, which is effectively metastable on the timescales considered in the experiment. Second, we used an Agilent E8257C Analog Signal Generator to apply a $600\,\mu$sec microwave pulse to the qubit, inducing transitions between an energy level in the right well and a higher energy level in the left well (shown in Fig. 5-12). Fig. 5-13 indicates the location of

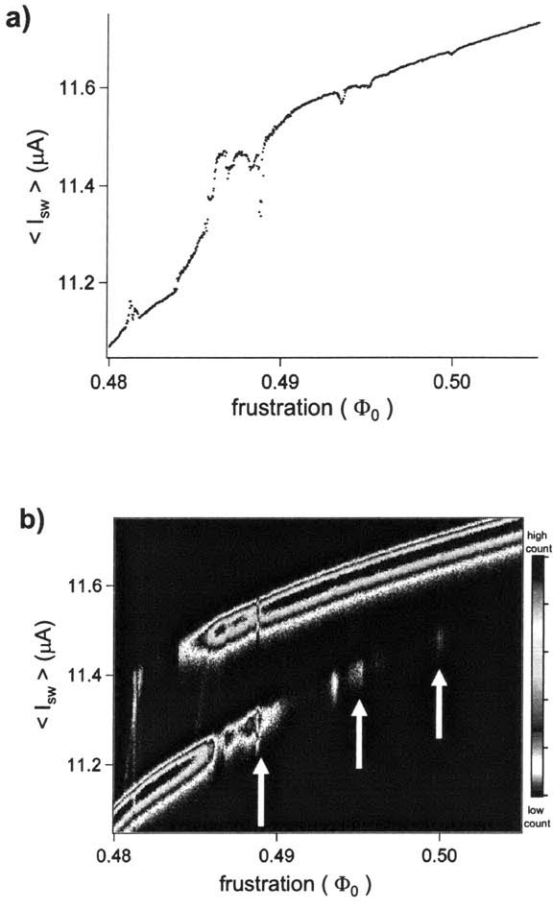

Figure 5-11: a) Blowup of qubit "step" region, corresponding to a change in circulating current. Data represents average of 10^3 switching events b) Contour plot of the "step" region. The qubit is initially prepared in the higher switching current and at given level crossings (indicated with arrows), resonant tunnelling causes transitions to the lower switching current state.

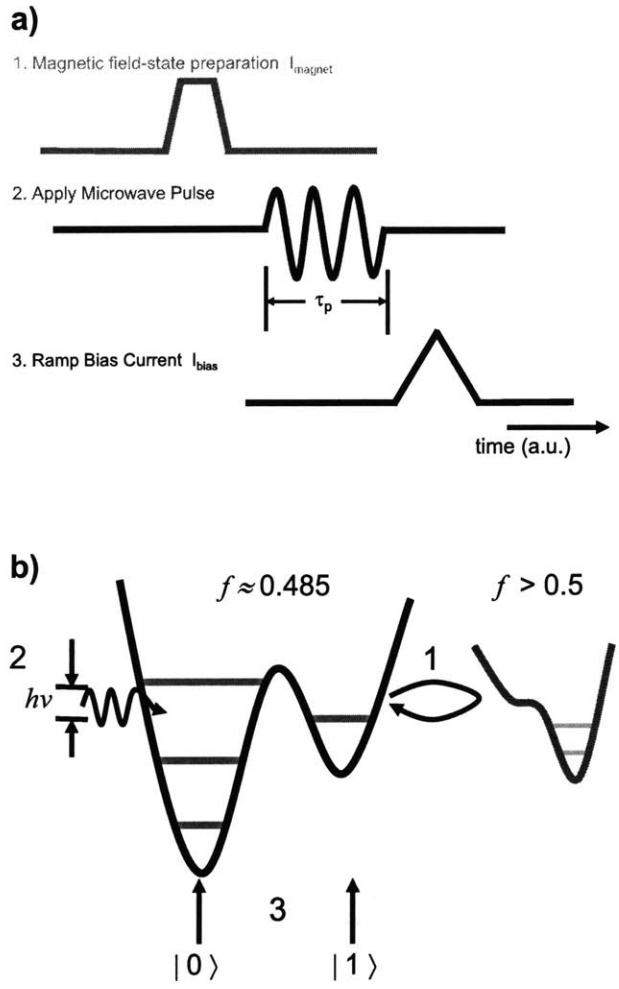

Figure 5-12: a) Pulse sequence used for Spectroscopy measurements. First, the state preparation pulse localizes the qubit in a metastable state. Second, resonant microwaves are applied to the system. Third, the bias current I_{bias} through the SQUID is ramped, thereby measuring which well the system is in. b) Pulse sequence effect on double well at $f \approx 0.485$. The state preparation produces a magnetic field ($f > 0.5$) pulse which localizes the system in the right well. Microwave radiation, at the indicated frequency, causes transitions between the energy level in the right well to the highest energy level in the left well. Ramping the bias current determines which well (left or right) the system is in.

the resonant transitions from the bandstructure of the PC qubit near $f = 1/2$. At low temperatures, the qubit will have a finite probability of remaining in $|1\rangle$, which is effectively metastable on the time scale considered. We then applied microwaves with duration time τ, inducing transitions between states $|1\rangle$ and $|0\rangle$. After the microwaves were shut off, the bias current I_{bias} of the SQUID was ramped through values slightly higher than its critical current I_c, thereby reading the qubit state, $|0\rangle$ or $|1\rangle$. For a fixed frustration, this procedure was repeated more than 10^3 times to minimize statistical error in the measurement. A histogram of the switching current clearly shows the probability distribution of the qubit state occupation. Shown in Fig. 5-14 are a series of contour plots of the switching-current histograms (for varying microwave frequencies applied) obtained by scanning the frustration at $T \simeq 12\,\mathrm{mK}$. Each vertical slice is a switching current histogram, and the gray scale represents the number of switching events (proportional to the switching probability).

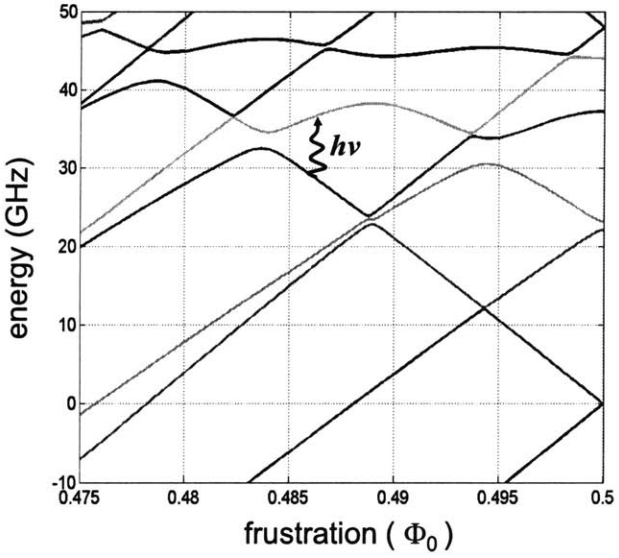

Figure 5-13: Calculated energy-level diagram of the PC qubit using qubit parameters determined from independent measurements. The arrow marks where the photon induced transitions occurred.

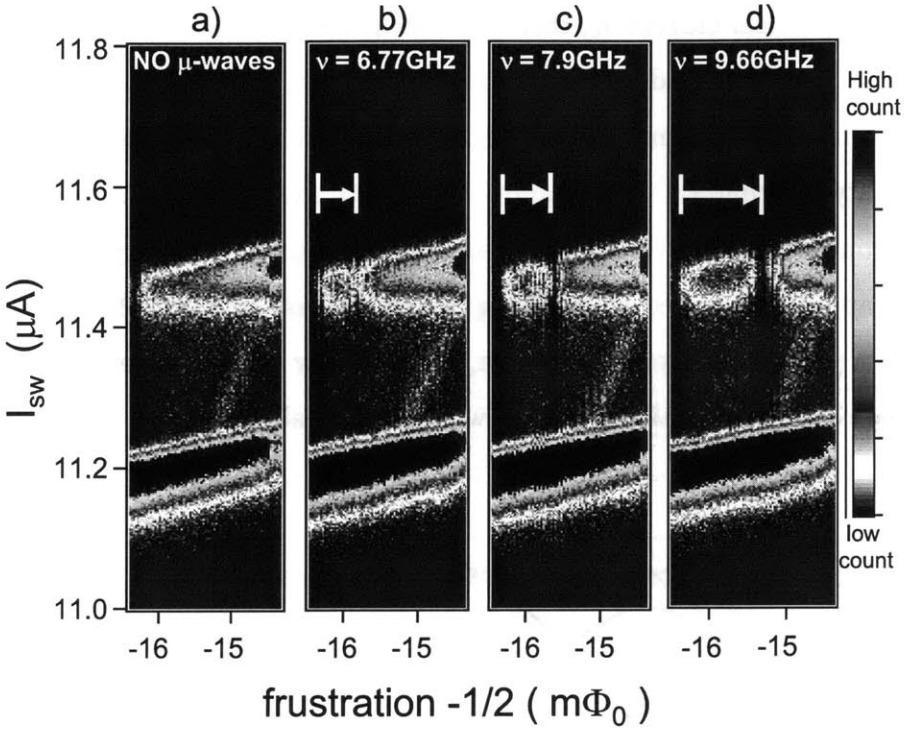

Figure 5-14: Contour plots of the switching current distribution (a) without microwaves, and with microwaves at (b) $\nu = 6.77\,\mathrm{GHz}$, (c) 7.9 GHz, and (d) 9.66 GHz. In each plot, the left-most tip of the upper branch corresponds to a fixed frustration point $f \simeq 0.484$. Without microwave irradiation, the population in the upper branch (state $|1\rangle$) decreased continuously to zero as the frustration decreased from 1/2. Microwaves pumped the population from state $|1\rangle$ to state $|0\rangle$ at the resonant frustration, the bias point at which the microwave frequency matched the energy level spacing between two states. The white arrows indicate that the resonant frustration moves toward 1/2 with increasing microwave frequency, in agreement with the qubit energy structure.

A bimodal structure in the switching-current distribution, caused by the opposite persistent current of the qubit, was observed at $f \simeq 0.485$. The lower branch represents the qubit in the $|0\rangle$ state, and the upper branch represents the qubit in the $|1\rangle$ state. The substantial population in state $|1\rangle$ demonstrates that we had successfully prepared the qubit in $|1\rangle$, because, near $f_q \simeq 0.485$, the qubit had a much higher single-well ground-state energy in $|1\rangle$ than that in $|0\rangle$. However, the energy barrier height and width relative to the lowest energy level of state $|1\rangle$ were small enough so that the qubit had a large probability of tunnelling to $|0\rangle$. A high probability of transition from one well to another can occur when energy levels on the left well are resonant with levels on the right well. The left-most tip of the higher branch marked a fixed frustration point $f_q \simeq 0.484$, below which it was not possible for the qubit to stay in $|1\rangle$, because the double well potential becomes a single-well state. Microwaves, with frequencies matching the energy difference between $|1\rangle$ and the highest level of $|0\rangle$, were used to generate transitions between the two states. The most striking feature of the contour plots is that a population "gap" or depleted region (i.e., zero population region) in the $|1\rangle$ branch was created by the microwaves (Fig. 5-14(b) to (d)). With increasing microwave frequency, the gap moved away from the left-most tip, as expected from the energy level structure (Fig. 5-13). The "gap" resulted from the initial population in the right well driven between the right and left well, eventually decaying to the ground state in the left well. The quantitative agreement between the gap position and the energy level structure confirmed that the gap resulted from the microwave induced transitions between the two macroscopic quantum states $|1\rangle$ and $|0\rangle_3$ (the third excited energy level of the state $|0\rangle$). Fig. 5-15 shows the average switching current values vs. frustration with different microwave frequencies applied. As we increase the frequency, we observe the "dip" (induced by the resonant transitions) shift with frustration. By mapping the energy separation, Fig. 5-16 shows the change in frustration vs. applied microwave frequency. The observed slope ($\Delta\nu/\Delta f \approx 4 - 6\,\mathrm{GHz/m}\Phi_0$) of the two resonant positions is consistent with the bandstructure calculations shown in Fig. 5-13. We also observe for a fixed frequency $\nu = 8.78\,\mathrm{GHz}$, the resonant "dip" increases in amplitude for increasing

microwave power (shown in Fig. 5-17). For large microwave power, we expect the microwaves to create a significant population distribution in the left ($|0\rangle$) well.

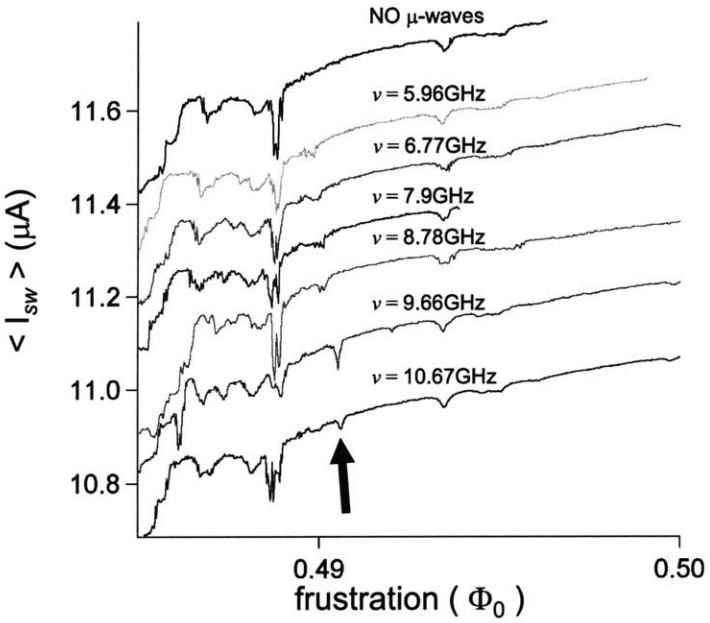

Figure 5-15: Traces of the average switching current $\langle I_{sw} \rangle$ versus frustration, measured with indicated microwave frequencies ν applied. Power is fixed at 0.5 mW. Dips in the traces (indicated with arrow) occur when microwaves are resonant with the energy difference between quantum levels. Using a range of frequencies ν, we are able to map the energy level separation between quantum levels.

The photon induced transitions at the indicated applied frequencies were an incoherent process - the microwave pulse duration of $600\,\mu$s, much longer than the estimated decoherence time ($0.1 - 100\,\mu$s) [14, 20, 26]. Additionally, no periodic variation of population with varying pulse duration (for long pulses) was observed. In a simple two-level system, observing such a gap would be unexpected for an incoherent transition, since the population in the lower level ($|0\rangle$) should always be larger than 0.5 in that case. In order to address this gap phenomenon in our double-well potential system, a multi-level pump-decaying model is introduced, which will be discussed in the following section.

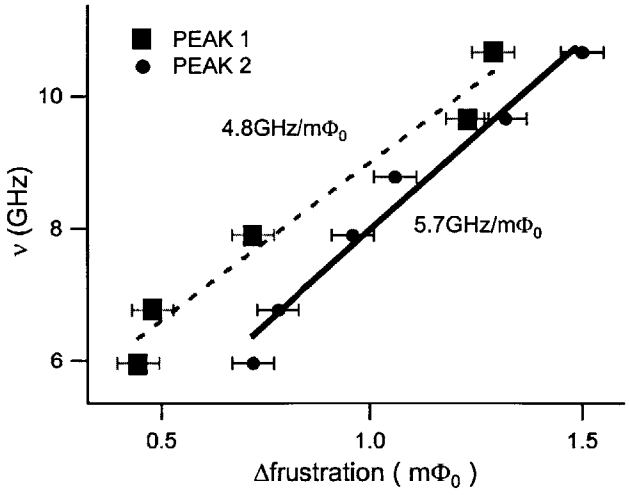

Figure 5-16: Mapping the energy level separation ν for a given change in frustration at $f \approx 0.485$ and $f = 0.49$. The resonant microwave dip (shown in Fig. 5-15) shifts with microwave frequency.The calculated slope values are consistent with the bandstructure calculations

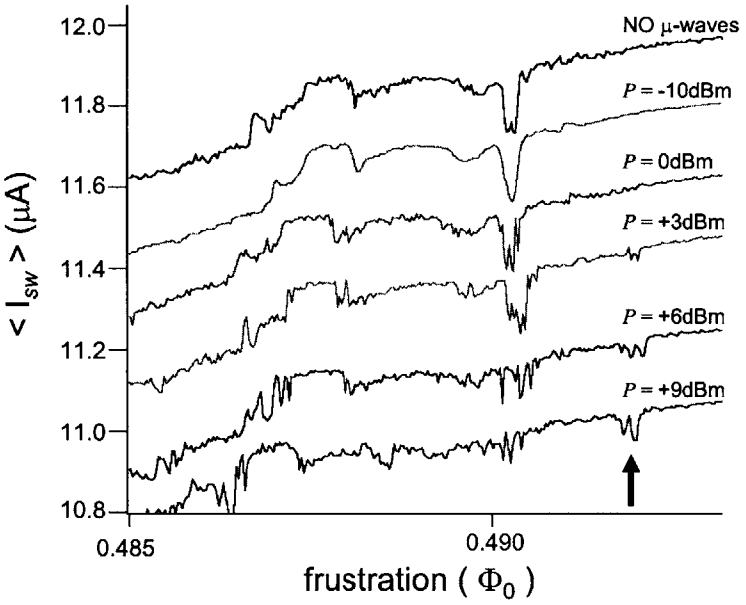

Figure 5-17: Traces of the average switching current $\langle I_{sw} \rangle$ versus frustration, measured at fixed frequency $\nu = 8.78\,\mathrm{GHz}$ but varying microwave power. Dips in the traces (indicated with arrow) increase in amplitude as power increases.

5.5 Energy Relaxation Time Measurements

For simplicity we consider only three levels in our system (shown in Fig. 5-18), the initial (prepared) state $|1\rangle_0$, the $|0\rangle_3$ state to which radiation induces a transition, and the state $|0\rangle_2$ to which the population of $|0\rangle_3$ decays. More accurately, the state $|0\rangle_3$ decays to $|0\rangle_2$, $|0\rangle_1$, and $|0\rangle_0$, but for ease of calculation, we collectively label these states as $|0\rangle_2$ with an overall effective intrawell decay rate $\gamma_d = 1/\tau_d$. The temporal evolution of the three-level system under microwave irradiation is thereby described by the following three coupled rate equations:

$$\frac{dP_{10}}{dt} = -\gamma_1 P_{10} + (\gamma_1 + \gamma_2) P_{03} \tag{5.1}$$

$$\frac{dP_{03}}{dt} = \gamma_1 P_{10} - (\gamma_1 + \gamma_2 + \gamma_d) P_{03} \tag{5.2}$$

$$\frac{dP_{02}}{dt} = \gamma_d P_{03} \tag{5.3}$$

in which P_{10}, P_{03}, and P_{02} are the occupation probabilities of level $|1\rangle_0$, $|0\rangle_3$, and $|0\rangle_2$ respectively. γ_1 is the stimulated transition rate between $|1\rangle_0$ and $|0\rangle_3$, and γ_2 is the spontaneous relaxation rate from $|0\rangle_3$ to $|1\rangle_0$. Generally, for a given system, γ_1 is proportional to the microwave power P_{rf}, and γ_2 can be considered to be a constant. For the initial condition $P_{10}(0) = 1$, with $P_{03}(0) = P_{02}(0) = 0$, Eqns. (5.1)-(5.3) can be solved analytically. For $\gamma_1 \geq \gamma_d$, which is satisfied in our experiment, the probability of finding the qubit remaining in the state $|1\rangle_0$ at $t > 1/(2\gamma_1 + \gamma_2 + \gamma_d)$ is given by

$$P_{10}(t) \approx a_1 \exp(-t/\tau') \tag{5.4}$$

where a_1 depends weakly on the microwave power and can be considered as a constant in the relevant time scale.

From Eqns. (5.1)-(5.4), we obtain a linear second order differential equation,

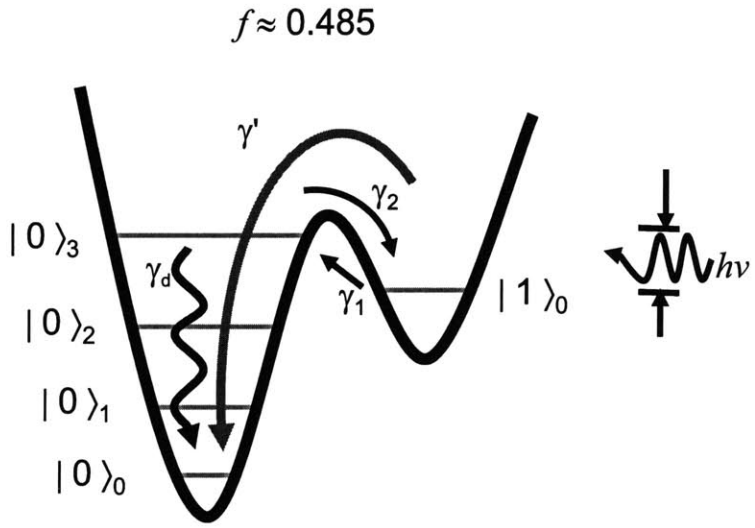

Figure 5-18: a) Double well potential at $f \approx 0.485$. Microwave radiation, for the indicated frequency $h\nu$, causes transitions between the energy level in the right well $|1\rangle_0$ to the highest energy level in the left well $|0\rangle_2$. γ_1 is the stimulated transition rate from $|1\rangle_0$ to $|0\rangle_3$ and γ_2 is the spontaneous relaxation rate from $|0\rangle_3$ to $|1\rangle_0$. Relaxation (at rate γ_d) occurs between $|0\rangle_2$ and $|0\rangle_0$.

$$\frac{d^2P_{10}}{dt^2} + (2\gamma_1 + \gamma_2 + \gamma_d)\frac{dP_{10}}{dt} + \gamma_d\gamma_1 P_{10} = 0 \tag{5.5}$$

The general solution to Eqn. (5.5) is of the form,

$$P_{10} = a_1 e^{r_1 t} + a_2 e^{r_2 t} \tag{5.6}$$

where a_1, a_2, r_1 and r_2 are constants. Solving for r_1 and r_2, we find

$$r_{1,2} = \frac{-(2\gamma_1 + \gamma_2 + \gamma_d) \pm \sqrt{(2\gamma_1 + \gamma_2 + \gamma_d)^2 - 4\gamma_1\gamma_d}}{2} \tag{5.7}$$

We assume $\gamma_1, \gamma_2 \gg 2\gamma_d$ therefore, $(2\gamma_1 + \gamma_2 + \gamma_d) \gg 2\sqrt{\gamma_1\gamma_d}$ then,

$$r_{1,2} \simeq \frac{-(2\gamma_1 + \gamma_2 + \gamma_d) \pm (2\gamma_1 + \gamma_2 + \gamma_d)(1 - \frac{2\gamma_d\gamma_1}{(2\gamma_1+\gamma_2+\gamma_d)^2})}{2} = -\frac{\gamma_d\gamma_1}{(2\gamma_1 + \gamma_2 + \gamma_d)} \tag{5.8}$$

The overall interwell time $\tau^{'}$ for the transition from state $|1\rangle_0$ to state $|0\rangle_0$ is then,

$$\tau^{'} \simeq (2 + \frac{\gamma_2}{\gamma_1})\tau_d = (2 + \frac{\gamma_2}{AP_{rf}})\tau_d \tag{5.9}$$

and A is the coupling constant between the microwave source and the qubit. We note for strong driving (large pumping effects) $AP_{rf} \gg \gamma_2$. Therefore, at high microwave power, the overall decay time $\tau^{'}$ saturates to

$$\tau^{'} \simeq 2\tau_d \tag{5.10}$$

The physical picture of the three-level pump-decaying process is that microwaves populate the highest level with a population $P_{03} \propto 1/(2 + \gamma_2/\gamma_1)$, which decays to the lowest level with a rate γ_d. Therefore, the effective decay rate of the population of the initial state is given by Eqn. (5.9), and with τ_p sufficient long, $P_{10}(t) \longrightarrow 0$; this agrees with the experimental observations.

A significant impact of Eqs. (5.4) and (5.9) is that τ_d can be determined by measuring $P_{10}(t)$. Because the switching current I_{sw} of $|0\rangle$ is smaller than that of $|1\rangle$,

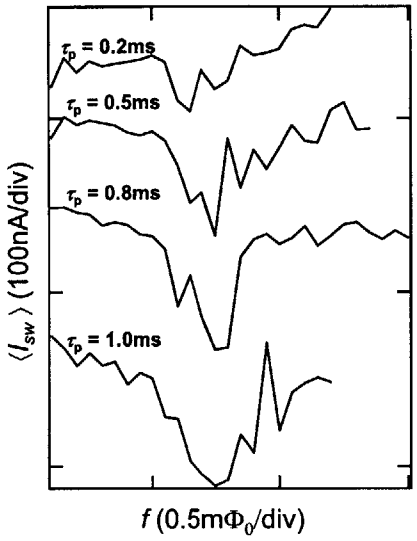

Figure 5-19: Resonant dips at for microwave pulse length $\tau_p = 0.2$, 0.5, 0.8 and 1 ms. For long microwave driving times, most of population relaxes to state $|0\rangle_0$.

pumping the system from state $|1\rangle$ to state $|0\rangle$ will generate a dip in the switching current I_{sw} average as a function of frustration, and the dip amplitude is proportional to $1 - P_{10}$. The applied radiation produces a population distribution between state $|1\rangle_0$ and state $|0\rangle_3$, with a relaxation time τ_d associated with the decay from $|0\rangle_3$ to $|0\rangle_0$. Fig. 5-19 shows the dip amplitude for different microwave irradiation times, τ_p. The nominal power of the microwave source was $P_{rf} = 31.6\,\mu$W. For small irradiation time, we expect the population distribution in state $|0\rangle_3$ to be small and therefore the probability to find the system in the left well is approximately zero for short τ_p radiation time. For longer radiation time, we continually produce transitions from state $|1\rangle_0$ to state $|0\rangle_3$, whereby in state $|0\rangle_3$ the system relaxes to state $|0\rangle_2$. Fig. 5-20 is a series of plots of the maximum dip amplitudes as a function of the microwave irradiation time, τ_p. For Fig. 5-20a, $P_{rf} = 31.6\,\mu$W and the time constant τ', obtained from a best fit, is $130 \pm 20\mu$s. It should be noted that τ' is not equal to τ_d, but, rather, it depends on γ_2/γ_1. For large P_{rf}, (i.e., $\gamma_1 \gg \gamma_2$), we expect the equal population distribution between states $|0\rangle_3$ and $|1\rangle_0$ then subsequent relaxation to the system

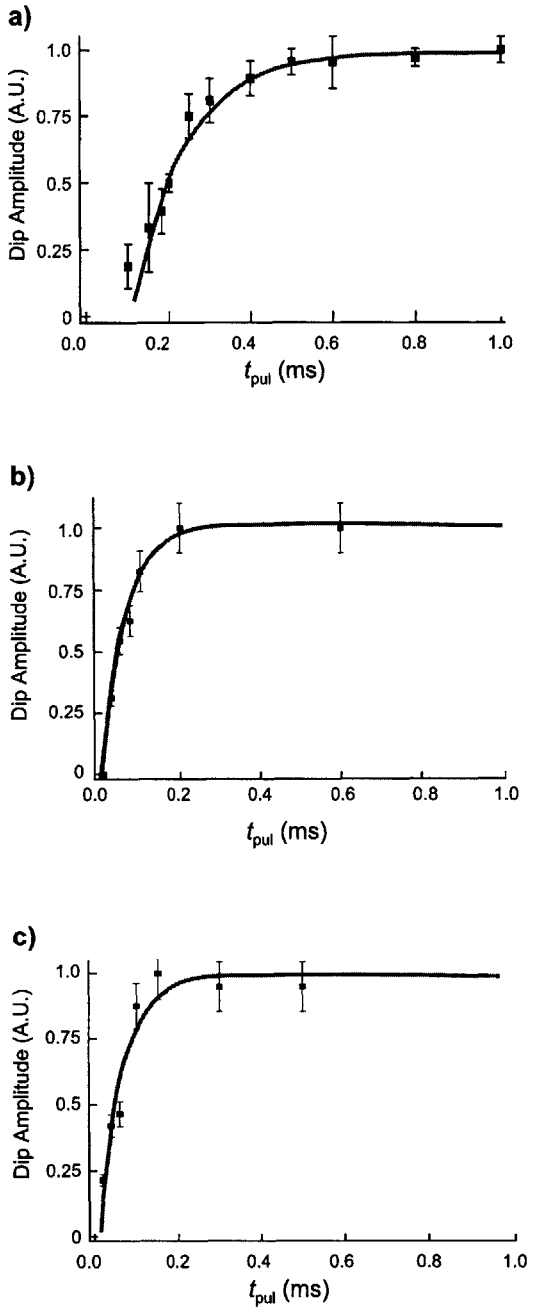

Figure 5-20: The amplitude of the microwave resonant dip as a function of microwave duration τ_p for microwave frequency $\nu = 9.66\,\text{GHz}$ and nominal power a) $P_{rf} = 31.6\mu\,\text{W}$, b) $P_{rf} = 125.9\mu\,\text{W}$ and c) $P_{rf} = 500.0\,\mu\text{W}$. The solid squares are experimental data and the solid line is a best fit to an exponential decay. From the best fit, we can obtain a value for the overall transition time τ' for a given microwave power.

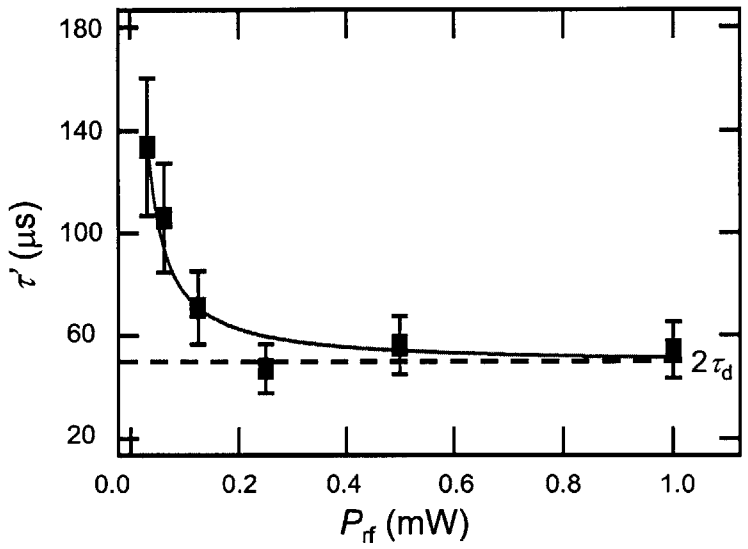

Figure 5-21: $\tau^{'}$ vs. microwave amplitude for $\nu = 9.66\,\mathrm{GHz}$. The solid line is a best fit to Eqn. (5.9). For increasing P_{rf}, $\tau^{'}$ saturates to $2\tau_d$ (denoted by dashed line).

ground state $|0\rangle_0$. Thus for large P_{rf}, we showed previously that $\tau^{'}$ is limited by the relaxation time τ_d and will saturate to $2\tau_d$. For $\gamma_1 \sim \gamma_2$, we are able to determine τ_d by measuring the microwave power dependence of $\tau^{'}$. Shown in Fig. 5-21 is $\tau^{'}$ measured at various microwave powers. $\tau^{'}$ saturates at about $50\,\mu\mathrm{s}$ for $P_{rf} > 200\,\mu\mathrm{W}$. By adjusting γ_2/A and τ_d as fitting parameters, we obtained $\tau_d \cong 24.3 \pm 2.7\,\mu\mathrm{s}$ from a best fit to Eqn. (5.9), which is consistent with dc tunnelling measurements. The measured intrawell relaxation time is of the same order of magnitude as the reported energy relaxation times in NbN and Al-based qubits [17]-[20]. Note that γ_2 is another important parameter which determines interwell energy relaxation. Unfortunately, the value of γ_2 could not be extracted from the fitting, due to the unknown coupling constant A. Future experiments in which microwave coupling is independently characterized should allow the extraction of γ_2.

The primary effect of the environmental dissipation on the intrawell dynamics of the PC qubits is that, at low temperature ($k_B T \ll E_1 - E_0$), the width of an excited level with energy E_n is given approximately by

$$\gamma_d \simeq \frac{E_n}{Q} \tag{5.11}$$

where Q is the quality factor of classical small oscillation in the potential well [80, 81]. From τ_d we determined $Q \sim 5 \times 10^5$, close to the value obtained from thermal activation measurements at intermediate temperatures $0.3 - 1.2\,\mathrm{K}$ [74, 75]. Note that Q is proportional to the subgap resistance, which ideally depends on the temperature as [82],

$$R_{subgap} \propto e^{\Delta/k_B T} \tag{5.12}$$

where Δ is the superconducting gap voltage discussed in section 4.1.1. The temperature independence of Q suggests the presence of additional environmental sources of dissipation [26].

This long intrawell relaxation time is important for experiments in quantum computing in two ways. First, the lower two energy levels in the left well, $|0\rangle_0$ and $|0\rangle_1$, could themselves be used as the two qubits states, with a third state $|0\rangle_3$ used as the read-out state. Because the PC qubit had no leads directly connected to it and the magnetic coupling circuit is optimally designed to lessen the effects of the electromagnetic environment, the PC qubit is much less influenced by this environment than are other similar single-junction schemes. Second, assuming the environment can be models as an ohmic bath, as in the spin-boson model, then we can estimate the decoherence times of a PC qubit in which the qubit states are those of opposite circulating current [14, 20, 26]. The energy relaxation and phase decoherence times within the spin-boson model for an ohmic environment were discussed in section 4.3 [66]. For our PC qubit system, $\alpha_L \sim 1/Q$ is the quantum damping parameter [82] which we estimate using our measured Q value. For our Nb PC qubit operating with opposite circulating currents states (for instance, biased near $f_q \approx 0.484\Phi_0$ where $\Delta \approx 2$ GHz and $\delta E \approx 4\,\mathrm{GHz}$), a conservative estimate gives $\tau_{relax} \geq 30\,\mu\mathrm{s}$ and $\tau_\varphi \geq 20\,\mu\mathrm{s}$ at 15 mK. We emphasize that an ohmic environment model may not adequately describe all sources of decoherence; these times must be viewed as estimates pending experi-

mental verification. Nonetheless, for a typical Rabi frequency $\Lambda = 1\,\mathrm{GHz}$, we obtained a quantum quality factor $Q > 10^4$, larger than the oft-quoted basic requirement for error-tolerant quantum computer.

5.5.1 Simulations of the Quantum Behavior

We previously employed a classical multi-level system to characterize the experimental behavior of the PC qubit system. Since the measurement process is incoherent (state readout is performed on a much longer time scale than the decoherence time), we do not expect to observe the periodic evolution of the qubit state with pulse duration. For rapid state readout ($\sim$ns ramp time), we expect to observe driven quantum oscillations between states $|0\rangle_3$ and $|1\rangle_0$. Therefore, a quantum mechanical model of the PC qubit is needed to simulate the time evolution of the system when driven with applied microwave radiation.

A simple three-level quantum system with energy relaxation or damping is used to model the PC qubit system biased at $f \approx 0.485$. The system has energy level $|3\rangle$ in the right well and levels $|2\rangle$ and $|1\rangle$ in the left well (shown in Fig. 5-22). We incorporate energy relaxation into our model by employing operation elements for amplitude damping. Our treatment considers the double well potential of the PC qubit within an open system, enabling us to describe the effect of noise and energy loss of the quantum system. For our system, we consider relaxation from state $|3\rangle$ to state $|1\rangle$ with rate γ_{31} and relaxation from state $|2\rangle$ to state $|1\rangle$ with rate γ_{21}. Microwaves induce coherent oscillations between states $|3\rangle$ and $|2\rangle$ at frequency Λ. We characterize the system using the density operator language, convenient to incorporate energy dissipation into our system.

The system is initially prepared in the metastable state $|3\rangle$ (right well)

$$|3\rangle = \begin{pmatrix} 0 \\ 0 \\ 1 \end{pmatrix} \tag{5.13}$$

The density operator language is convenient to incorporate energy dissipation.

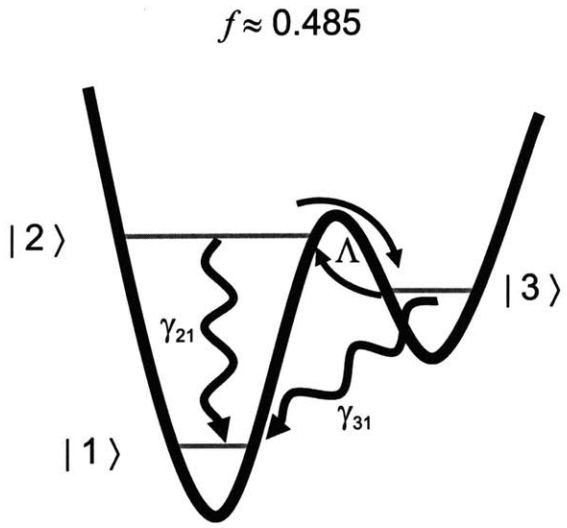

Figure 5-22: PC qubit double well potential at $f \approx 0.485$. Resonant microwaves induce transitions between $|3\rangle$ and $|2\rangle$. Due to energy dissipation, damping occurs between levels $|2\rangle$ and $|1\rangle$ at rate γ_{21} and between $|3\rangle$ and $|1\rangle$ at rate γ_{31}.

Suppose a quantum system is in one of a number of states $|\psi_i\rangle$, we define the density matrix as

$$\rho \equiv \sum_i p_i |\psi_i\rangle \langle\psi_i| \tag{5.14}$$

where p_i is the probability in state $|\psi_i\rangle$. We note that $\sum_i p_i = 1$ with $p_i \geq 0$. We define the initial density matrix ρ_0 to be

$$\rho_0 = |3\rangle\langle 3| = \begin{pmatrix} 0 & 0 & 0 \\ 0 & 0 & 0 \\ 0 & 0 & 1 \end{pmatrix} \tag{5.15}$$

The Hamiltonian H_R using the rotating wave approximation couples the states $|3\rangle$ and $|2\rangle$ when radiation is applied and is given by,

$$H_R = \begin{pmatrix} 0 & 0 & 0 \\ 0 & 0 & \Lambda \\ 0 & \Lambda & 0 \end{pmatrix} \tag{5.16}$$

where Λ is the driven oscillation frequency between state $|3\rangle$ and $|2\rangle$. The time dependent density matrix is given by,

$$\rho(t) = e^{iHt}\rho_0 e^{-iHt} \tag{5.17}$$

If we consider no damping effect (perfect isolation from the environment), we expect continuous coherent oscillations between levels $|3\rangle$ and $|2\rangle$. If we now consider damping between levels $|3\rangle$ and $|1\rangle$ as well as from levels $|2\rangle$ and $|1\rangle$, the density matrix is found by

$$\rho(t') = \sum_k E_k \rho(t) E_k^\dagger = E_0 \rho(t) E_0^\dagger + E_1 \rho(t) E_1^\dagger \tag{5.18}$$

where E_0, E_1 are the damping operators between levels $|3\rangle$ and $|1\rangle$. The amplitude damping operators from state $|3\rangle$ to state $|1\rangle$ are given by,

$$E_0 = \begin{pmatrix} 1 & 0 & 0 \\ 0 & \frac{1}{\sqrt{2}} & 0 \\ 0 & 0 & \sqrt{1-\Gamma_{31}} \end{pmatrix} \tag{5.19}$$

$$E_1 = \begin{pmatrix} 0 & \frac{1}{\sqrt{2}} & 0 \\ 0 & 0 & \sqrt{\Gamma_{31}} \\ 0 & 0 & 0 \end{pmatrix} \tag{5.20}$$

where $\Gamma_{31} = 1 - \exp(-t/\tau_{31})$ and τ_{31} is the energy relaxation time between state $|3\rangle$ and $|1\rangle$.

We now consider damping from state $|2\rangle$ to state $|1\rangle$ at a rate γ_{21}. The density matrix $\rho(t'')$ after time t'' is then

$$\rho(t'') = E_2\rho(t'')E_2^\dagger + E_3\rho(t'')E_3^\dagger \tag{5.21}$$

where E_2, E_3 are the damping operators between levels $|2\rangle$ and $|1\rangle$. The amplitude damping operators E_2 and E_3 are given by,

$$E_2 = \begin{pmatrix} 1 & 0 & 0 \\ 0 & \sqrt{1-\Gamma_{21}} & 0 \\ 0 & 0 & \frac{1}{\sqrt{2}} \end{pmatrix} \tag{5.22}$$

$$E_3 = \begin{pmatrix} 0 & \sqrt{\Gamma_{21}} & 0 \\ 0 & 0 & 0 \\ 0 & 0 & \frac{1}{\sqrt{2}} \end{pmatrix} \tag{5.23}$$

where $\Gamma_{21} = 1 - \exp(-t/\tau_{21})$ and τ_{21} is the energy relaxation time between state $|2\rangle$ and $|1\rangle$.

The overall probability in state $|3\rangle$ as a function of time is then given by $\rho_{3,3}(t)$. Fig. 5-23 shows a simulation of the probability of the system in the right well ($|3\rangle$) as a function of time with $\tau_{21} = 20\,\mu$s and $\tau_{31} = 200\,\mu$s. The system oscillates between state $|3\rangle$ and $|2\rangle$, with an exponential envelope caused by damping to the system's lowest energy level $|1\rangle$.

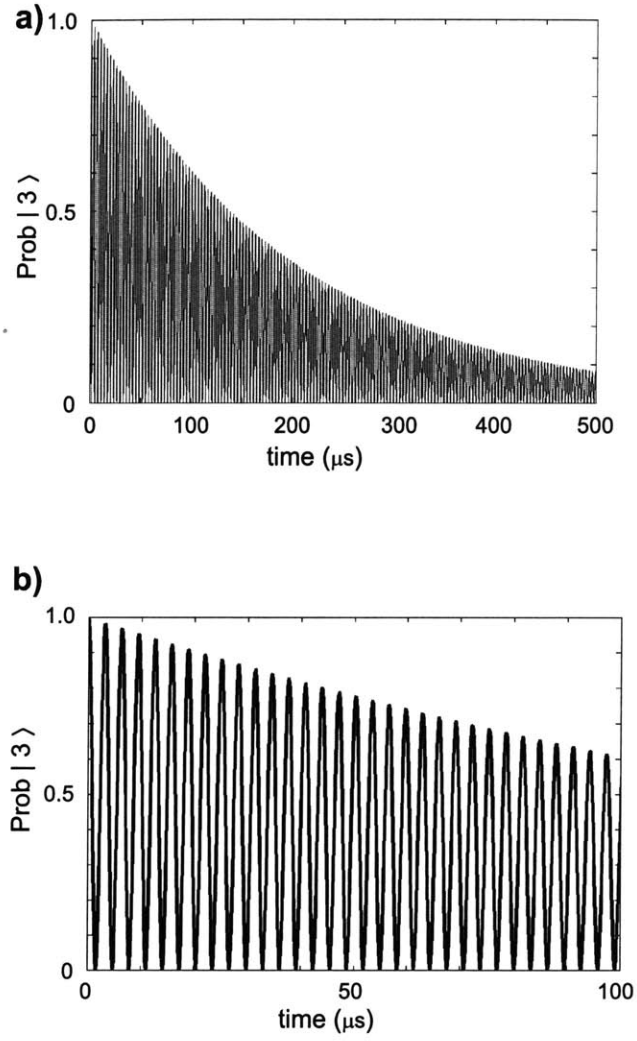

Figure 5-23: Probability in state $|3\rangle$ as a function of time for parameters $\Lambda = 10\,\text{MHz}$, $\tau_{31} = 200\,\mu\text{s}$ and $\tau_{21} = 20\,\mu\text{s}$. For sufficiently long driving times, the system eventually relaxes to the system's lowest energy state $|1\rangle$.

5.5.2 Waiting Time Measurements

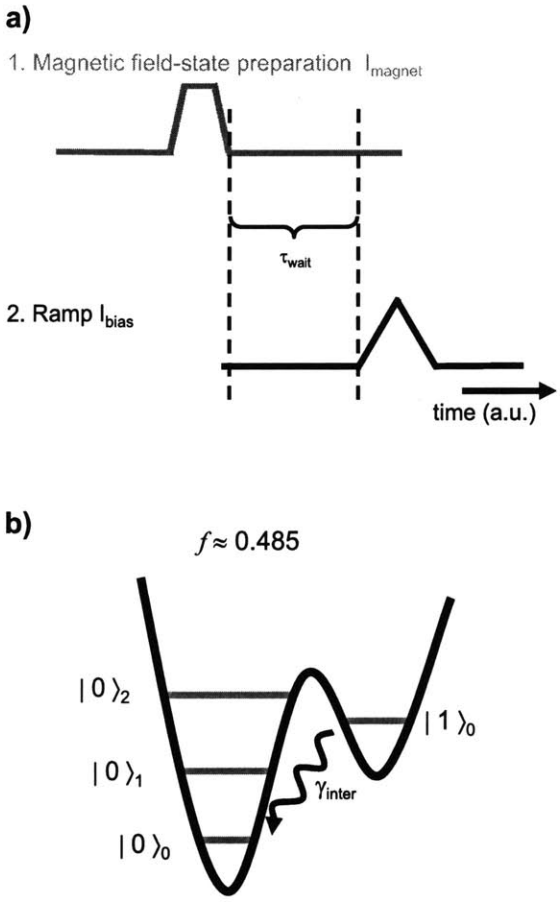

Figure 5-24: Double well potential structure. The particle is initially prepared in the metastable state $|1\rangle_0$ within the right well. At rate γ_{inter}, the system relaxes to the ground state energy of the system $|0\rangle_0$, in the left well.

To verify the stability of energy state in the right well in time, we examine the interwell energy relaxation between quantum states. The qubit is biased to exhibit an asymmetric double-well potential (shown in Fig. 5-24). Interwell population transitions were generated by first initializing the system in the "ground state" of the higher-energy well using a state preparation pulse, then waiting for time τ_{wait} for the population to relax to the lowest-energy state in the right well (i.e., the true system ground state). We assume an exponential decay to state $|1\rangle_0$ of the form

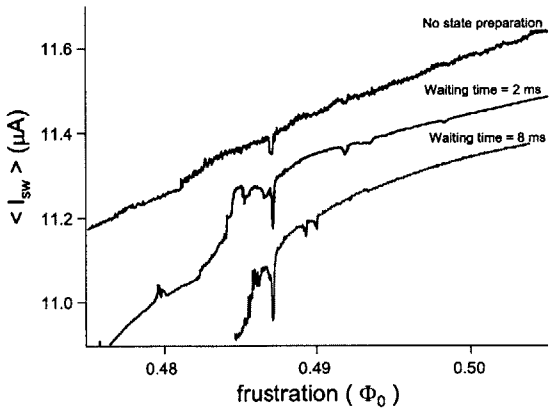

Figure 5-25: Average switching current value plots for varying waiting times. Top curve for no state reparation pulse. As the waiting time between state preparation and readout increases, we observe a significant increase in the lower state $|0\rangle$ population due to interwell relaxation.

$$P_{10}(t) \approx b_1 \exp(-t/\tau_{inter}) \tag{5.24}$$

where P_{10} is the initial population in state, b_1 is a constant, and τ_{inter} is the interwell energy relaxation time. By increasing the waiting time between state preparation and measurement, we observed an increase in the lower-energy well population at level crossings (Shown in Fig. 5-25).

5.6 Experimental Challenges-Future Considerations

Several technological improvements are needed to enhance the experimental progress of the Nb PC qubit. Coherent oscillations experiments will require 1) a well-isolated environment for qubit control and 2) a stable magnetic field source. The difficulty in achieving the proper microwave environment and a steady magnetic field bias is characterized and new methods will be presented (in Appendix B) to overcome these experimental hurdles.

From the switching current response of the SQUID readout device, it was determined that strong resonant coupling within this cavity occurred at microwave

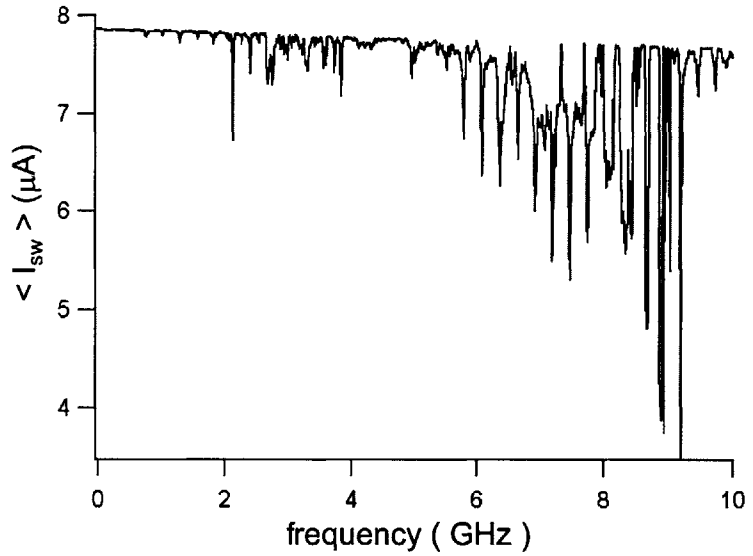

Figure 5-26: DC SQUID $\langle I_{sw} \rangle$ for given applied microwave frequencies at zero magnetic field. Strong coupling between the microwaves and DC lines results in suppression of I_{sw} at certain the frequencies. A microwave package has been designed to eliminate these unwanted resonances (See Appendix B).

frequencies near or at the qubit energy level separation of interest (Shown in Fig. 5-26). At zero applied magnetic field, the DC SQUID switching current value was recorded as the microwave frequency was swept from $0 - 10$ GHz. The length of the DC bias lines ($\sim 3-4$ cm.) was of comparable length to the applied radiation (10 GHz corresponds to 3 cm) therefore the radiation coupled predominantly to these DC measurement lines. At a resonant frequency of the cavity, mode oscillations suppressed the switching current value of the DC SQUID. A microwave package, whose first resonance frequency is higher than the energy levels separation, has been designed and fabricated to reduce or eliminate these oscillations for greater qubit control.

In order for coherent oscillations to be observed, the frustration at which the PC qubit is biased must remain stable in order to maintain a constant energy level separation. To apply an external magnetic field through the qubit a superconducting magnet is used, driven by a Yokogawa current source. Fig. 5-27 shows the Fourier

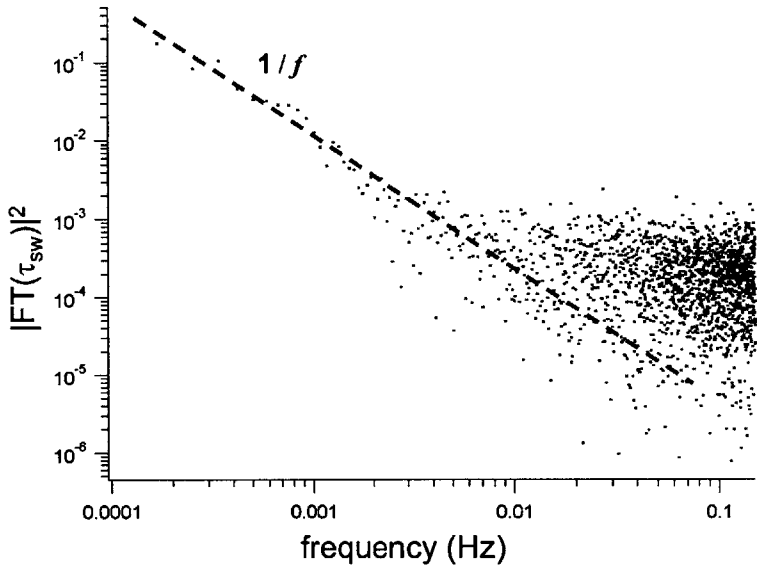

Figure 5-27: DC SQUID $\langle I_{sw} \rangle$ $1/f$ noise. For a fixed magnetic bias, the switching current of the DC SQUID is sampled at 250 Hz for a $\sim$ 10 hr time period.

transform of the switching current measurements for a 10 hour period (repetition frequency 250 Hz). Fluctuations in the critical current of the junctions I_c cause $1/f$ noise in the switching current value of the DC SQUID.

5.7 Summary

This chapter presented low temperature measurements of a Nb PC qubit. The measurements first required design of the electronics measurement apparatus and low temperature sample environment to minimize noise coupling to the quantum system. Considerable effort was made to reduce the effects of electrical, vibrational and magnetic noise coupling into our system. At dilution refrigerator temperatures, spectroscopy was used to map the energy level separation between quantum states. We observed resonant transitions between quantum levels, at microwave frequencies ranging from 5-10 GHz which were consistent with theoretical predictions of the calculated bandstructure of the qubit. After probing the energy level separation, the intrawell

relaxation time τ_d was directly measured by generating resonant transitions between macroscopically distinct quantum states using varying microwave pulse lengths. By varying the driven microwave pulse length, we observed dynamic population distributions between potential wells. A multi-level decay process was then observed and the intrawell relaxation time τ_d was determined to be 24μs with a quality factor Q greater than 10^5. The measured relaxation time and Q are consistent with previous experimental work on the Nb PC qubits. The decoherence time is predicted to be proportional to the level of dissipation, which results from the coupling between the qubit and environment [83]. The corresponding phase-decoherence time within a spin-boson model is inferred to be $\sim 20\,\mu$s for these devices. These measurements indicate that flux qubits operating between wells would also have sufficient decoherence times, demonstrating good prospects for well-fabricated Nb trilayer junctions to be used as superconducting qubits. Nonetheless, measurements to observe coherent oscillations between quantum states will require a well-isolated microwave environment for optimum qubit control.

Chapter 6

Conclusions

6.1 Summary of Results

Superconducting qubits, the PC qubit in particular, continue to show great promise for large scale quantum computing applications. The largest drawback to macroscopic qubits was thought to have been the rapid rate of decoherence within such systems. Recent studies in superconducting qubits show that this view may be pessimistic - improvements in fabrication technology and low-temperature measurement techniques will eventually lead to longer decoherence times.

This thesis investigates the experimental implementation of the Nb PC qubit. The PC qubit has been designed, fabricated in a standard Nb trilayer process, and measured at dilution refrigerator temperatures. The doctoral research involves understanding the fabrication process to design an appropriate Nb PC qubit and readout device for the low-temperature measurement setup. Further work is necessary to quantify the decoherence mechanisms in the PC qubit system - both from internal (fabrication) and external (low temperature environment) factors.

The MIT Lincoln Laboratory superconductive device fabrication process was used to produce submicron Josephson junctions for both quantum computing applications and RSFQ circuitry. Requirements for coherent quantum devices monolithically integrated with classical electronics required targeting of exact fabrication parameters and producing high quality Josephson junctions. The anodization process was one

method investigated to improve critical current-density J_c uniformity. We compared J_c uniformity of wafer pairs, fabricated together, with the only difference being the presence or absence of the anodization step, and showed cross-wafer J_c standard deviation is a factor 3 higher for unanodized wafers. To control for anodization, the wafer pairs we examined were simultaneously subjected to the same highly uniform oxidation process involved in producing the tunnelling barrier. The results suggest that there exists in-process modification of J_c that is avoided or diminished by anodization. Isolating the cause of the modification, however, remains difficult since many subsequent processing steps are required to produce useful junctions.

Low-temperature measurements investigated decoherence within these fabricated Nb-based PC qubits. The measurements required careful design of the electronics measurement apparatus and low temperature sample environment to minimize noise coupling to the quantum system. Initial measurements on the Nb-based qubit mapped the energy level separation between quantum states using spectroscopy. We observed resonant transitions between quantum levels, at microwave frequencies ranging from 5-10 GHz which were consistent with theoretical predictions of the calculated band-structure of the device. The intrawell relaxation time τ_d was then directly measured by generating resonant transitions between macroscopically distinct quantum states using varying microwave pulse lengths. By varying the microwave pulse length or microwave power, we observed dynamic population distributions between potential wells. A multi-level decay process was then observed and the intrawell relaxation time τ_d was determined to be 24μs with a quality factor Q greater than 10^5. The measured relaxation time and Q are consistent with previous experimental work on the Nb PC qubit fabricated at MIT Lincoln Laboratory. The relatively long relaxation times and high Q value indicates that these intrawell levels are well-isolated from the electromagnetic environment and are themselves potentially favorable qubit levels. The decoherence time is predicted to be proportional to the level of dissipation, which results from the coupling between the qubit and environment [83]. The corresponding phase-decoherence time within a spin-boson model is inferred to be longer than $20\,\mu$s for these devices. These measurements indicate that flux qubits operating between

wells would also have sufficient decoherence times, demonstrating good prospects for well-fabricated Nb trilayer junctions to be used as superconducting qubits. Considering the attractiveness of Nb-based qubits from the point of view of robust and well-developed, mature fabrication methods, these relaxation times suggest that they are a promising candidate for realizing a scalable quantum computer.

6.2 Future Work

Further work is needed in both material/process engineering research coupled with low temperature coherence measurements to produce reliable, high quality (low dissipation) qubits with long coherence times. Continued feedback between circuit design, fabrication and low-temperature measurements are required to converge on a successful PC qubit sample. Successful low temperature measurements also requires careful isolation techniques to minimize noise to the sample. The successful qubit device then requires the thorough understanding and consideration of the fabrication methods, qubit sample design, and low-temperature setup.

Progress within the Nb superconducting fabrication technology requires materials research to further improve the viability of using Nb devices for quantum computing applications. The scope and depth of the fabrication facilities enhance the probability of success in the fabrication of high quality Josephson junctions for qubits. A new fabrication process (Ten day or TD process) has recently developed for rapid turnaround in the process time. The ten day process relies on three Nb metal layers to form a circuit (using anodized Nb as an insulating layer). The standard fabrication process can be modified to this Nb/Al/AlO_x/Nb fabrication technology, such as the addition of a second aluminum layer on top of the aluminum oxide, and thickening of both aluminum layers, have also been suggested to improve performance. The thickened aluminum is known to improve the barrier chemistry. Although Nb is better lattice-matched to the AlO_x barrier, this modification may reduce leakage due to pinhole, or other defects in the barrier, while still retaining a high gap voltage. The use of ultra low-J_c junctions ($J_c \sim 10\,\mathrm{A/cm^2}$), which are correlated to reduced sub-gap current,

may also be employed for the PC qubit.

Future work on the low temperature measurements of the PC qubit will focus on observing coherent oscillations between distinct quantum energy levels. At the proper energy level separation, one can apply varying (between 1 ns - 10μs) microwave pulse lengths to drive transitions between levels. One then finds the probability of finding the system in a given well is periodic with microwave driving time. Progress to observe coherent oscillations between macroscopic quantum states within this PC qubit system requires improvements in sample isolation and readout. Improving isolation between the quantum system's environment, which accompanies advances in low-temperature measurement techniques, will lengthen the dephasing time τ_{vaprhi}. The observation of Rabi oscillations therefore requires engineering a microwave cavity and devising a method for rapid measurement capability to readout the state of the qubit. The immediate objectives for the measurement of timed coherent oscillations are:

- Design and install a microwave package that incorporates DC magnetic field biasing capability and allows microwave irradiation inside the package. Progress on the microwave package is discussed in Appendix B.

- Implement high-bandwidth cables for the SQUID current bias and voltage readout lines. Demonstrate $\sim$ 100 MHz bandwidth (approx. 10 ns resolution) capability. Copper powder filters will be used to filter these lines above $\sim$1 GHz.

- Demonstrate microwave irradiation using on-chip coplanar waveguide terminated with an inductor and show that this applied irradiation is largely decoupled from the DC SQUID. Progress on the on-chip waveguides are discussed in Appendix B.

The research presented in this thesis shows the potential of superconducting qubits for large scale quantum computing applications. Many challenges, most importantly the decoherence effect in superconducting qubits, must be overcome to realize a useful Josephson junction device. The basic studies on the Nb PC qubit presented are the

initial step in the development of a practical superconducting qubit. Nonetheless, the study of macroscopic quantum effects in superconducting devices continues to be an academically challenging and fruitful area of research.

Appendix A

MIT Lincoln Laboratory DPARTS Process

The MIT Lincoln Laboratory doubly planarized all-refractory technology for superconductive electronics (DPARTS) process is used to fabricate submicron Nb/Al/AlO_x/Nb Josephson junction devices. The DPARTS process uses optical projection lithography using an i-line stepper, chemical mechanical planarization(CMP) of two silicon-oxide layers, a self-aligned via process and dry reactive ion etching (RIE) of the Nb layers and via etching steps. In general, the base electrode (M2), counter-electrode (M3) and wiring layer (M4) are used to form Josephson junctions circuits while a fourth Nb layer (M5) is used as a ground plane layer to minimize magnetic coupling between circuit elements. Two SiO_2 layers (I2 and I3) are used as passivation or insulating layers. The resistor layer (R1) is used as a resistor metal layer. Finally, the contact pad layer (M6) is used to gain electrical contact to the Nb Josephson junction circuits.

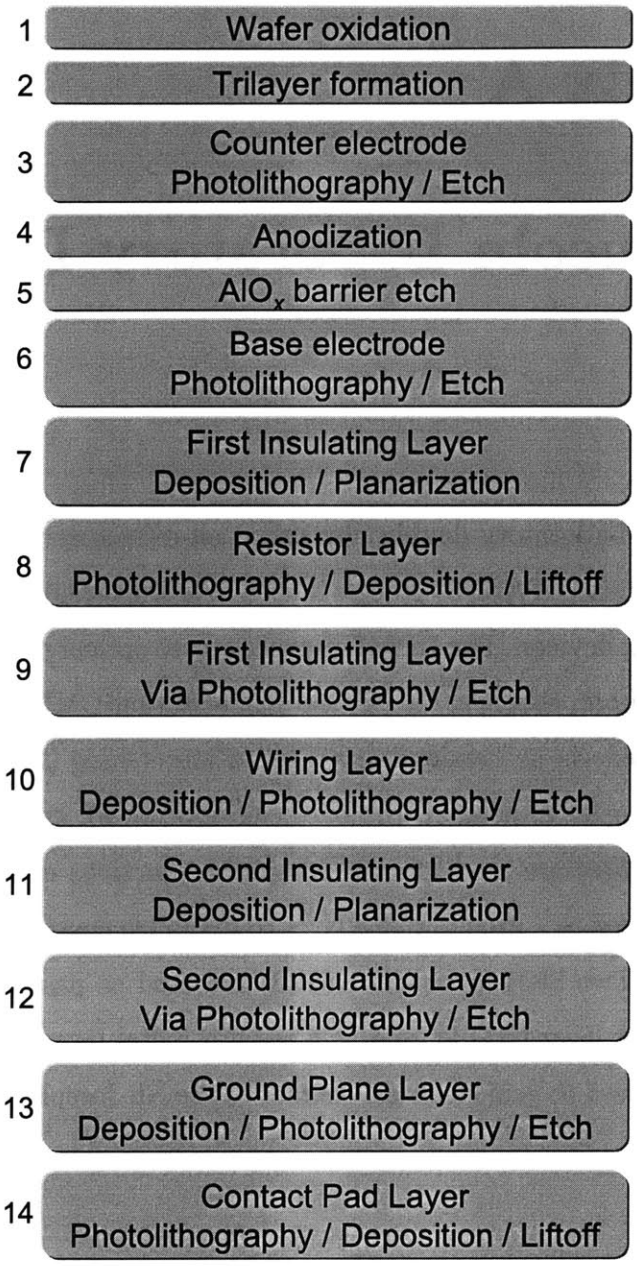

Figure A-1: MIT Lincoln Laboratory Abbreviated process flow.

Table A.1: Given layer, conventional layer name, material and final thickness values in MIT Lincoln Laboratory Low Temperature Superconducting Device Fabrication Process.

Layer	**Conventional Layer name**	**Material**	***Thickness(Å)**
Base-electrode	M2	Nb	1500
Counter-electrode	M3	Nb	2000
First PECVD Insulating layer	I2	SiO_2	3500
Resistor	R1	Ti/Pt	100/900
Wiring	M4	Nb	2500
Second PECVD Insulating layer	I3	SiO_2	6000
Ground plane	M5	Nb	4000
Contact pad	M6	Ti/Pd/Au	300/3600/500

*Final layer thickness value at its maximum, which can be less than the deposited thickness value.

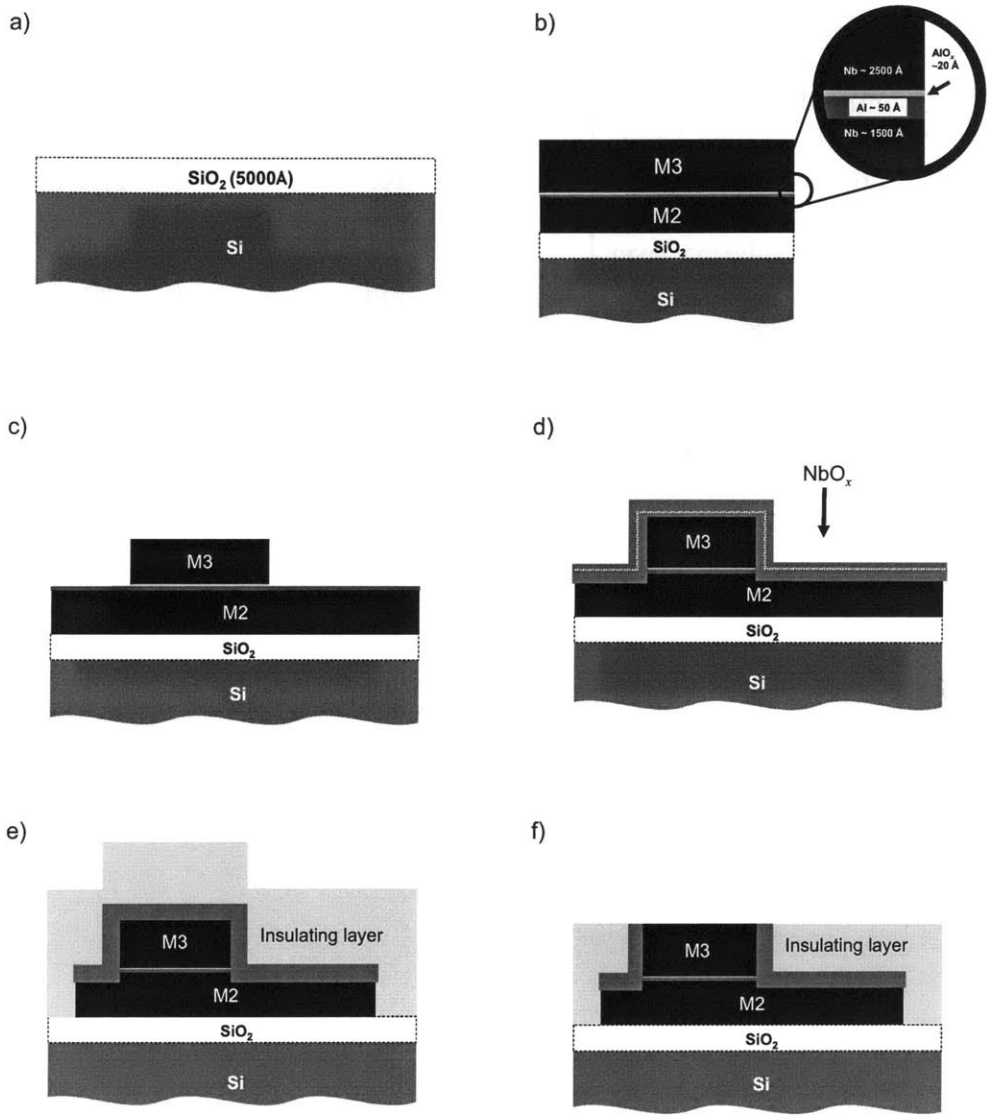

Figure A-2: a) First step is wet oxidation of prime silicon wafer. b) Nb trilayer deposited. Inset shows a closeup of the AlO_x tunnelling barrier region. c) Counter-electrode(M3) is reactive-ion etched. d) Junction is anodized, producing a protective NbO_x layer, effectively "sealing" the perimeter of the junction. Dotted white line indicates original surface. e) After the barrier is stripped and the base electrode(M2) etched, PECVD oxide(I2) is deposited. f) CMP of the oxide layer is used to achieve self-aligned contact to the counter-electrode(M3) and produces global planarity.

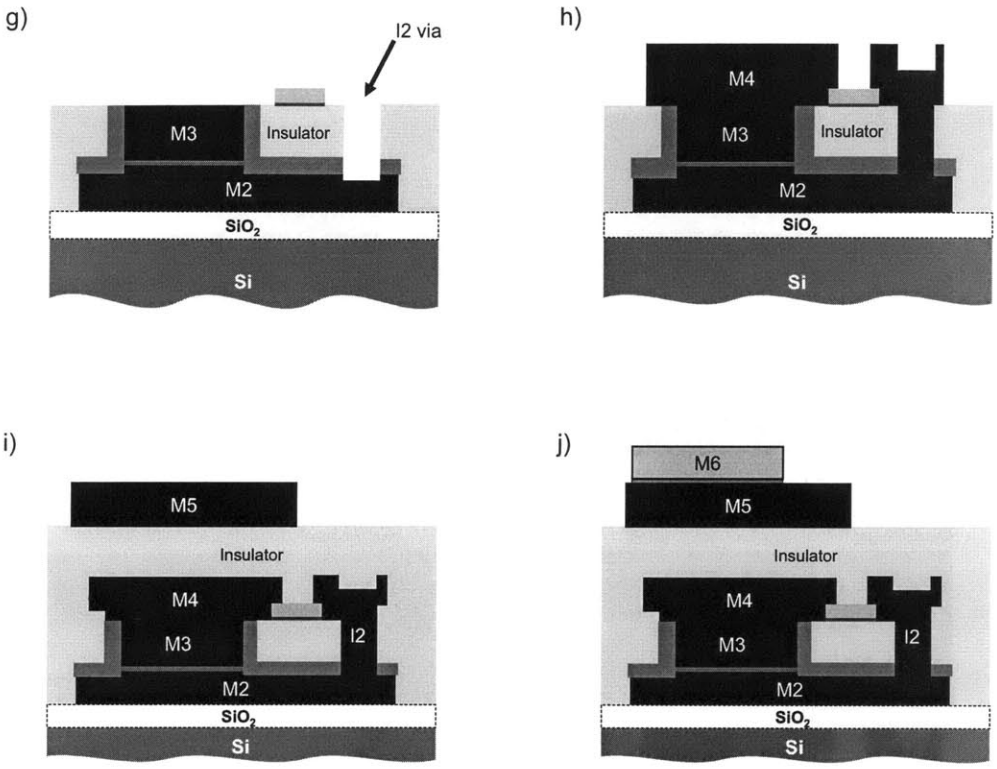

Figure A-3: g) Resistor layer(R1) is defined by liftoff technique. I2 vias are etched to gain electrical contact to the base-electrode(M2). h) Wiring layer(M4) is deposited, patterned and etched. i) Second PECVD oxide(I3) layer is deposited then planarized. Ground plane(M5) is deposited, patterned, then etched. j) Contact pads(M6) are deposited and defined using liftoff.

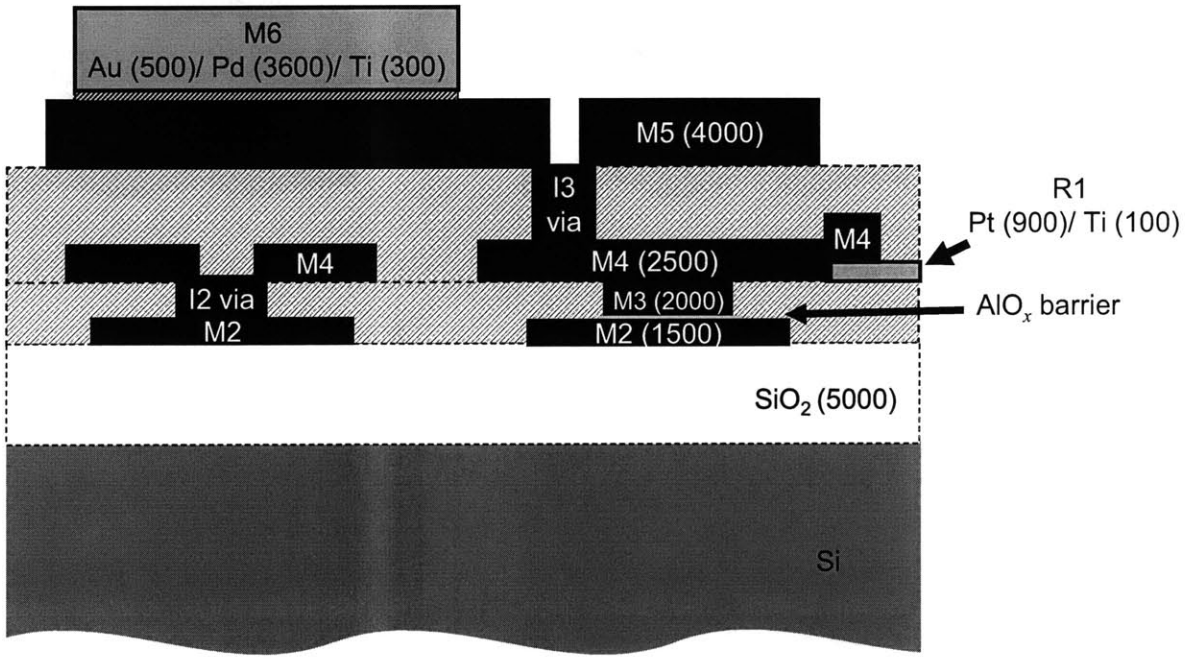

Figure A-4: Cross-section of completed Nb trilayer circuit. Numbers in parentheses indicate layer thickness values in Å.

Appendix B

Microwave Environment

The observation of driven coherent oscillations between macroscopic quantum levels will require careful qubit control and isolation from the environment. In order to create the proper microwave environment for the qubit, one requires: 1) the design of on-chip coplanar waveguide structures to provide high frequencies radiation ($\sim 1 - 10\,\mathrm{GHz}$) to the qubit sample and 2) engineer a microwave cavity to suppress resonant modes coupling to the SQUID bias and readout lines. The following section describes the effort taken to undergo a proper microwave environment for the PC qubit.

B.1 On-chip Coplanar Waveguide Considerations

We describe the on-chip coplanar waveguide (CPW) structure designed to guide microwaves near the qubit sample ($\sim 10 - 100\,\mu\mathrm{m}$ away). As shown in Fig. B-1, the coplanar waveguide consists of a center strip of width S with two ground planes connected parallel to and in the plane of the strip, a distance W away. The CPW is terminated with a large shunt inductor ($L \sim 300\,\mathrm{pH}$) used to couple microwaves inductively to the sample. The shunt inductance value L is calculated using FASTHENRY. At the characteristic microwave frequencies used ($\sim$ 1-10 GHz) to excite the qubit, we try to match the impedance of the waveguide to the load impedance. The characteristic impedance of the coplanar waveguide structure is calculated using

[46]

$$Z_{cpw} = \frac{30 \ln\left[2\frac{1+\sqrt{k}}{1-\sqrt{k}}\right]}{\sqrt{\epsilon_{re}}} \tag{B.1}$$

for $0 < k < 0.707$ where,

$$k = \frac{S}{S + 2W} \tag{B.2}$$

The effective dielectric constant ϵ_{re} is given by,

$$\epsilon_{re} = \frac{\epsilon_r + 1}{2}\left[\tanh\{1.785 \log(h/W) + 1.75\} + \frac{kW}{h}\{0.04 - 0.7k + 0.01(1 - 0.1\epsilon_r)(0.25 + k)\}\right] \tag{B.3}$$

where h is the height of the dielectric below the waveguide and W is the distance from the ground plane to the center strip.

The effective parameters for the CPW are given in Table B.1.

Table B.1: Parameters of the on-chip coplanar waveguide.

Parameter	Definition	Value
k	center strip width	2 μm
h	height of dielectric	0.5 μm
L	inductance of shunt inductor	300 pH
M	mutual inductance bet. inductor and PC loop	~0.1-1 pH
Z_L (@10 GHz)	load impedance	20 Ω
Z_{cpw}	impedance of CPW	50 Ω

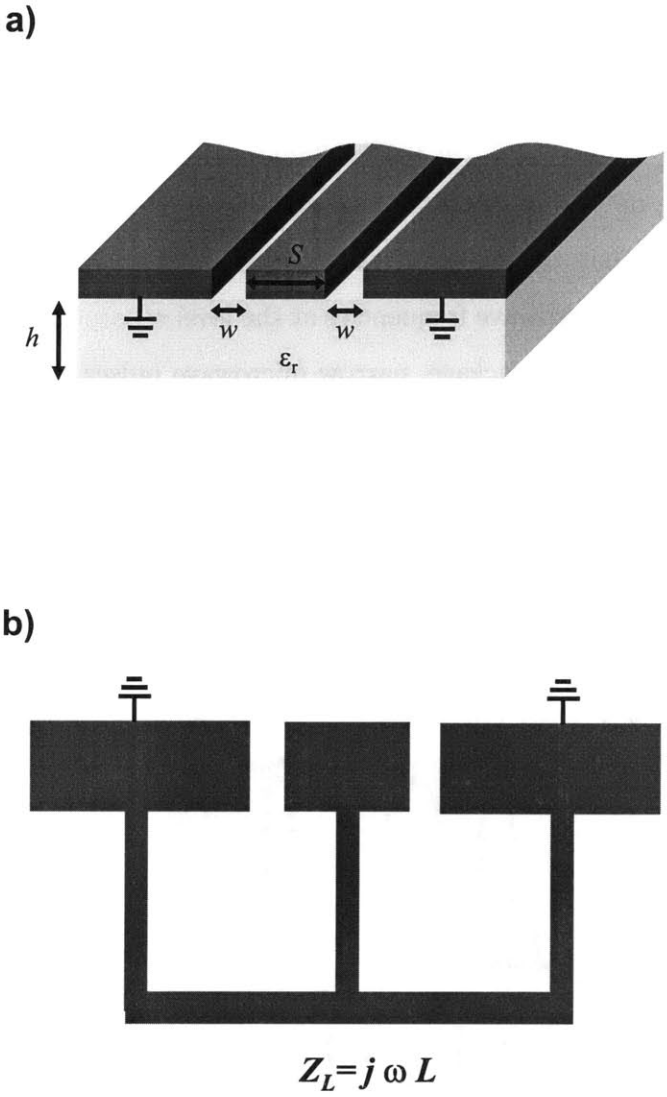

Figure B-1: Coplanar waveguide structure: a) the CPW consists of a center strip of width S with two ground planes connected parallel to and in the plane of the strip, a distance W away. The structure sits on a dielectric substrate ϵ_r of thickness h. b) The end of the CPW is terminated by a shunt inductor Z_L

B.2 Microwave Package Design Considerations

Spectroscopy measurements on the Nb PC qubit were performed in a ~ 1 in cylindrical copper sample space. From the switching current response of the SQUID readout device, it was determined that strong resonant coupling within this cavity occurred at frequencies near or at the qubit energy level separation of interest (Shown in Fig. 5-26). At a resonant frequency of the cavity, mode oscillations increase and damp away slowly. Therefore, operating the qubit in a microwave package, whose first resonance frequency is higher than the energy levels separation, will greatly improve microwave control. By applying microwave frequencies at the level separation of the qubit, below the cutoff frequency of the package, narrow microwave pulses ($\sim$ ns) can be applied. Ideally, the end result is a constant electromagnetic response of the switching current of the DC SQUID in the frequency range $1 - 10$ GHz.

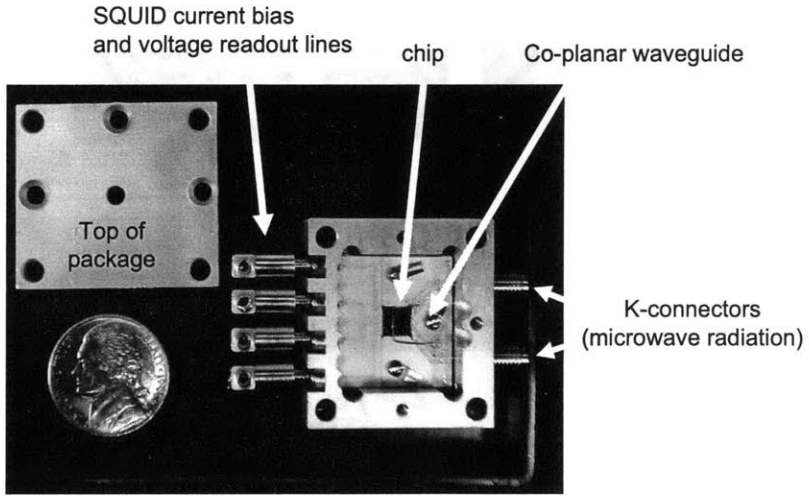

Figure B-2: MIT Lincoln Laboratory microwave package. The package consists of a gold-plated copper cavity containing an alumina substrate to guide signals to the device chip. Four microstrip lines lead from the ssmb connectors to the SQUID. A K-connector is used for microwave irradiation. The microwaves travel along a co-planar waveguide to an small loop inductor which couples the radiation to the qubit.

A copper microwave package has been designed to optimize experimental microwave control of the PC qubit. The microwave package designed by MIT Lincoln Laboratory is shown in Fig. B-2. The package is a gold-plated oxygen-free copper with inner dimensions of 0.80" and 0.90" and outer dimensions of 1.40" and 1.26" with an alumina substrate placed within the cavity. The 5×5 mm^2 chip is mounted directly on the gold-plated surface using a square block at the center of the alumina substrate. The alumina substrate is attached to the copper package using three screws which act as metallic vias. The DC SQUID lines from the outside are connected to the package using four ssmb panel mounts (50 Ω, 6 GHz nominal bandwidth). On the inside, small wires connect the panel mounts to microstrip lines on the alumina substrate. Microwave radiation used to drive the qubit transitions enters the package through a 40 GHz K-connector. The K-connector feedthrough is mounted directly to a co-planar waveguide using a dedicated soldering tool to achieve a good 50 Ω match. The co-planar waveguide (on the alumina substrate) to the circuit chip is also a 50 Ω design. The microwave radiation can then be applied using either an on-chip inductor or terminated with a small (∼ 1 cm) metallic loop. The microwave package lid holds a bobbin, which is used to mount a Nb-wire solenoid directly above the device. The coil is used to magnetic field bias the qubit and has a low bandwidth (∼kHz).

We can estimate the cavity modes of the rectangular cavity. We assume the copper package is a freespace cavity (μ_0, ϵ_0) with highly conducting walls. The lowest cavity-mode frequency is obtained along the longest internal dimension of the cavity, a=0.9in=2.3cm. A cavity mode is established when a number of N half-wavelengths can be accommodated. In terms of the cavity dimensions $a = 0.9\,\text{in} = 2.3\,\text{cm}$, $b = 0.8\,\text{in} = 2.0\,\text{cm}$, and $d = 0.22\,\text{in} = 0.55\,\text{cm}$, the resonant frequencies for the Transverse Electric (TE) and Transverse Magnetic (TM) cavity modes are found for an ideal cavity to be [85],

$$f_{lmn} = \frac{c}{2\sqrt{\epsilon_r}}\sqrt{\left(\frac{l}{a}\right)^2 + \left(\frac{m}{b}\right)^2 + \left(\frac{n}{d}\right)^2} \tag{B.4}$$

for integers $l, m, n = 0, 1, 2...$ and ϵ_r is the relative dielectric constant and $c = 3 \times$

10^8 m/s. We estimate $\epsilon_r \approx 1$. The five lowest cavity-mode frequencies are given in Table B.1. Since we are interested in frequencies ranging from 1-10 GHz, the lowest resonant mode f_{110} may couple strongly to the SQUID and qubit. A future effort will be made to reduce the size of the cavity such that the lowest resonant mode is much larger than the microwave frequencies of interest $f_{110} \gg \hbar\nu_{applied} \approx 10$ GHz.

Table B.2: Five Lowest Resonant Modes of Microwave Package.

Cavity mode	**Frequency (GHz)**
f_{110}	7.95
f_{210}	15.0
f_{120}	16.4
f_{101}	28.0
f_{011}	28.3

Appendix C

Selected Reprints

Page 175

D. Nakada, K.K. Berggren, E. Macedo, V. Liberman, and T.P. Orlando, "Improved Critical-Current-Density Uniformity by Using Anodization," *IEEE Trans. Appl. Superconductivity*, **13**, 111, 2003.

Page 179

D.S. Crankshaw, K. Segall, D. Nakada, T.P. Orlando, L.S. Levitov, S. Lloyd, S. Valenzuela, N. Markovic, M. Tinkham, and K.K. Berggren, "DC Measurements of Macroscopic Quantum Levels in a Superconducting Qubit Structure with a Time-Ordered Meter," *Phys. Rev. B*, **69**, 144518, 2004.

Page 188

Y. Yu, D. Nakada, J.C. Lee, B. Singh, D.S. Crankshaw, K.K. Berggren, T.P. Orlando, W.D. Oliver, "Energy Relaxation Time between Macroscopic Quantum Levels in a Superconducting Persistent-Current Qubit," *Phys. Rev. Lett.*, **92**, 117904, 2004.

Improved Critical-Current-Density Uniformity by Using Anodization

Daniel Nakada, Karl K. Berggren, Earle Macedo, Vladimir Liberman, and Terry P. Orlando

Abstract—**We discuss an anodization technique for a Nb superconductive-electronics-fabrication process that results in an improvement in critical-current-density J_c uniformity across a 150-mm-diameter wafer. We outline the anodization process and describe the metrology techniques used to determine the NbO_x thickness grown. In the work described, we performed critical current I_c measurements on Josephson junctions distributed across a wafer. We then compared the J_c uniformity of pairs of wafers, fabricated together, differing only in the presence or absence of the anodization step. The cross-wafer standard deviation of J_c was typically $\sim$ 5% for anodized wafers but $>$ 15% for unanodized wafers. This difference in J_c uniformity is suggestive of an in-process modification from an unknown cause that is blocked by the anodic oxide. It is interesting that small junctions do not see an improvement in I_c uniformity-apparently the anodization improves only the J_c uniformity and not the variation in junction size. Control of J_c is important for all applications of superconductive electronics including quantum computation and rapid single-flux quantum (RSFQ) circuitry.**

Index Terms—**Anodization, critical-current-density, Josephson junctions.**

I. Introduction

CONTROLLING the critical-current-density J_c uniformity across a wafer is a major challenge in the Nb Josephson junction fabrication process. Typically, the J_c variation across a 150-mm-diameter wafer is $>$ 15% for current densities ranging from 0.1–20 kA/cm^2. Highly uniform J_c is desired for producing low cross-chip J_c variation as well as producing a higher quantity of chips per wafer at a given critical-current-density. Past results suggested that anodization of the junction region improves J_c uniformity across a wafer but this suggestion has never been supported with direct comparisons [1]–[3]. In this paper, we address our efforts to incorporate anodization into our standard Nb process and we study its effects on J_c uniformity by directly comparing anodized wafers with unanodized wafers.

The Josephson junctions were fabricated in a class-10 cleanroom facility at MIT Lincoln Laboratory. We used our standard doubly planarized all-refractory technology for superconductive electronics process [DPARTS] [4]. The substrates were 150-mm-diameter prime silicon wafers, thermally oxidized to produce a 500-nm-thick SiO_2 layer. The Nb/Al/AlO_x/Nb trilayer was then deposited, followed by patterning of the Nb counter-electrode (C.E.) using optical projection lithography. Reactive ion etching (RIE) of the counter-electrode was performed in a load-locked chamber using SF_6 gas. Because we felt that after RIE the junction region could be vulnerable to chemical, plasma and/or other damage from subsequent processing steps (shown in Fig. 1(a), we anodized the wafer to form a 50-nm-thick protective metal-oxide layer around the junction perimeter. Fig. 1(b) shows that after anodization the junction region is "sealed" from the outside environment by

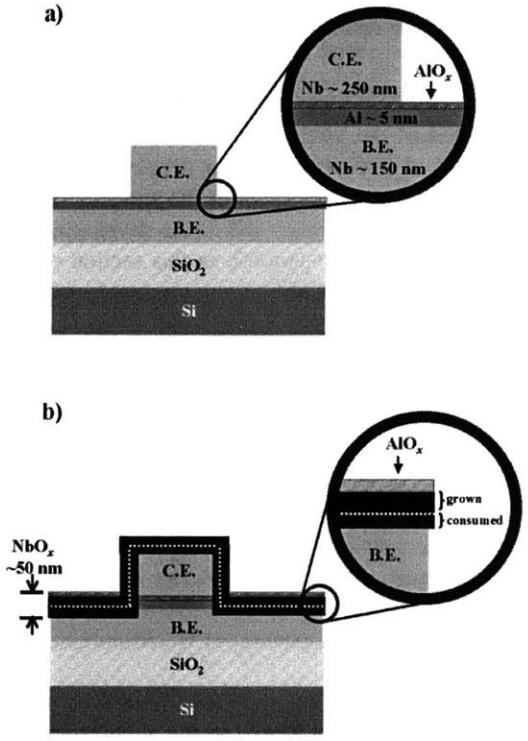

Fig. 1. a) Nb Josephson junction after counter-electrode (C.E.) etch but immediately prior to anodization. Inset shows the AlO_x tunneling barrier region. b) Junction region after anodization. The surface of the counter- and base-electrode (B.E.) is converted to a metal-oxide layer approximately 50 nm thick. The dotted line shows the original surface. Inset shows amount of anodic oxide grown and consumed. The anodic oxide causes the surface to swell up and out slightly during growth.

Manuscript received August 6, 2002. This work was supported in part by the Department of Defense under the Department of the Air Force Contract F19628-00-C-0002, in part by the Air Force Office of Scientific Research under Grant F49620-01-1-0457 under the DoD University Research Initiative on Nanotechnology (DURINT) program, and by ARDA. Opinions, interpretations, conclusions and recommendations are those of the authors and are not necessarily endorsed by the Department of Defense.

D. Nakada and T. P. Orlando are with the Department of Electrical Engineering, Massachusetts Institute of Technology, Cambridge, MA 02139 USA (e-mail: dnakada@mit.edu).

K. K. Berggren, E. Macedo, and V. Liberman are with Lincoln Laboratory, Lexington, MA 02173-9108 USA (e-mail: berggren@ll.mit.edu).

Digital Object Identifier 10.1109/TASC.2003.813658

a thick NbO_x layer. The remaining steps of the process were modified slightly to account for the presence of this layer, as described in Section II.

We first outline the anodization procedure and its incorporation into the standard Nb superconducting device fabrication process. We then discuss metrology methods used to determine the thickness of niobium oxide grown. We follow with a discussion of the effects of anodization on critical-current-density uniformity, presenting room-temperature normal-state resistance measurements of junctions. Finally we conclude with discussion and analysis of our results.

II. Anodization Process Description

The modification of the fabrication process to include anodization consisted of three steps: 1) the development of the anodization process; 2) the integration of the anodization step into the existing DPARTS process; and 3) the development of metrology methods for process control. In this section we describe work in each of these areas.

A. Anodization Process

Anodization is an electrolytic process in which a metal, in our case niobium, serves as the anode in a suitable electrolyte. When a current passes through the Nb film in the electrolytic solution, the surface of the Nb is converted to its oxide form. This oxidation progresses from the solution inward, toward the metal, with the final thickness determined by the applied voltage. The metal-oxide layer serves as a protective barrier to further ionic flow [5]. Anodization processes of this sort have been used extensively in the past for the fabrication of Nb Josephson junctions [1], [6]–[10].

For our process, anodization followed the RIE of the counter-electrode and stripping of photoresist, so the anodization was unmasked. Anodization was performed in an electrolytic solution of tartaric acid ($HOOC(CHOH)_2COOH$) and ammonium hydroxide (NH_4OH). 400 g of tartaric acid powder were added to a recirculating bath of an approximately 5L volume of deionized water. Then a 28–30% NH_4OH solution was added incrementally until the measured pH was 5.1 ± 0.1 (the total volume of NH_4OH solution added was $>$ 300 ml). The anodization process proceeded as follows: (1) A Pt wafer (cathode) in the electrolytic solution was grounded while the Nb device wafer (anode) was connected to a power supply. (2) The voltage output of the power supply was ramped, from 0 V to 20 V, maintaining an initial constant current of 0.225 A through the wafer. The overall ramp time was approximately 50 sec. (3) The voltage was then held constant at 20 V. During the voltage hold time, the current through the wafers dropped exponentially as the NbO_x layer densified. (4) When the current level reached 10% of its initial value, the power supply was abruptly switched off. The total immersion time was approximately 1.5 minutes. After anodization, the wafers were cleaned using deionized water in a dump-rinser and spin-rinser dryer.

B. Process Integration

Subsequent process steps were modified to account for the NbO_x layer. The NbO_x layer made it difficult to etch through the base-electrode and to gain contact through a via to the base- and counter-electrode. We modified the RIE etching process for the base-electrode slightly from that of the other Nb layers by performing it at a substrate temperature of 80°C (compared to 50°C for the other Nb layers). This elevated temperature was needed to etch through the 50 nm NbO_x layer. We also observed an etch undercut profile due to the anodic oxide (see Fig. 3(a)).

To achieve contact through the anodic layer at the base of the via (between the base-electrode/wiring layer and counter-electrode/wiring layer) we relied on the 25% over-etch of the PECVD deposited oxide and the pre-sputter of the wiring layer to promote adhesion between the base-electrode and wiring layer. To achieve contact to the counter-electrode, we used the polishing from chemical mechanical planarization (CMP) and the pre-sputter prior to wiring deposition to remove the NbO_x grown on the top of the counter-electrode.

TABLE I
Optical Constants of Nb and NbO_x. Index of Refraction n and Absorption Coefficient k Values vs. Wavelength for Nb Film and 95 nm Thick NbO_x Film

	Nb		NbO_x	
λ(nm)	n	k	n	k
400	2.644	3.144	2.565	2.785×10^{-3}
425	2.707	3.262	2.565	1.666×10^{-3}
450	2.788	3.362	2.479	0
475	2.871	3.439	2.454	0
500	2.943	3.500	2.433	0
525	3.000	3.550	2.416	0
550	3.038	3.596	2.401	0
575	3.059	3.643	2.388	0
600	3.065	3.697	2.376	0
625	3.058	3.760	2.365	0
650	3.041	3.834	2.354	0
675	3.018	3.920	2.345	0
700	2.992	4.018	2.336	0
725	-	-	2.327	0
750	-	-	2.32	0
775	-	-	2.313	0
800	-	-	2.306	0

C. Thickness Metrology

Determining NbO_x layer thickness is critical for both process control of anodization and for all subsequent dielectric metrology. In our process, film thicknesses are typically measured by using spectral reflectometry, for which the optical constants and thickness of all underlying films are required. Data available in the literature for bulk and thin-film Nb and NbO_x was found to be inadequate: it could not determine the anodic film thickness accurately from spectral reflectometry or ellipsometry. We therefore needed to determine the index of refraction n and absorption coefficient k of the underlying Nb and NbO_x as a function of wavelength.

To determine the optical constants of NbO_x we first needed an independent measure of the film thickness. We used scan-

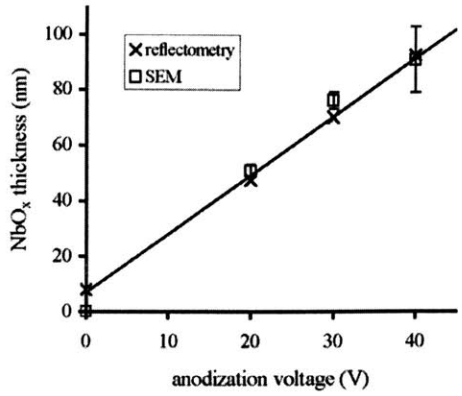

Fig. 2. NbO_x film thickness for given anodization voltage. Film thickness is determined both by reflectometry measurements and SEM images. The solid line represents the best-fit line to the reflectometry data.

ning electron microscopy (SEM) images to determine the film thickness. We then determined the optical properties of the Nb and NbO_x film using a Hitachi U-4000 spectrophotometer with a 12-degree absolute-reflectance attachment. The resulting reflectance data was used to extract the index of refraction n and absorption coefficients k as a function of wavelength for a Nb layer and 95-nm-thick NbO_x layer. The results are given in Table I. NbO_x data varied by a few percent depending on the thickness of the oxide; the range of Cauchy coefficients was from $A_n = 2.169$ to $A_n = 2.236$ and from $B_n = 0.047$ to $B_n = 0.05$ while A_k and B_k were zero (the range is too small to be important for our purposes therefore we simply used Cauchy coefficients of $A_n = 2.169$ and $B_n = 0.047$). For Nb the Cauchy coefficients were $A_n = 3.20$, $B_n = -0.086$ and $A_k = 4.625$ and $B_k = -0.25$. We then compared the film thicknesses extracted from fitting spectral reflectometry data to measurements from SEM images for a variety of anodization voltages and found agreement, as shown in Fig. 2. Finally, optical reflectometry and SEM data were compared to ellipsometric analysis at 632 nm and agreement was also obtained.

As mentioned previously, we used SEM images to estimate NbO_x thickness and transmission electron microscopy (TEM) images to inspect the anodic film. A SEM image of NbO_x grown on a Nb layer is shown in Fig. 3(a). We estimate the thickness of the NbO_x layer to be ~ 50 nm for an anodization voltage of 20 V. Sample preparation and TEM imaging of Josephson junctions was performed by MCNC and TEM Analysis Inc. Prior to imaging, the junctions were tested at liquid helium temperatures (4.2 K) and found to have good quality ($V_m > 50$ mV). TEM images of the anodized junction region is shown Fig. 3(b).

Comparing anodized/unanodized wafer pairs for wafers with 50 nm of NbO_x, we determined from step-height measurements that the thickness of anodized wafers was typically 30 nm greater than unanodized wafers. From this we conclude that approximately 20 nm of Nb was consumed in the growth process.

III. Effect of Anodization on Critical-Current-Density Uniformity

In order to determine the effect of anodization on the electrical characteristics of our junctions, we looked at their normal-state

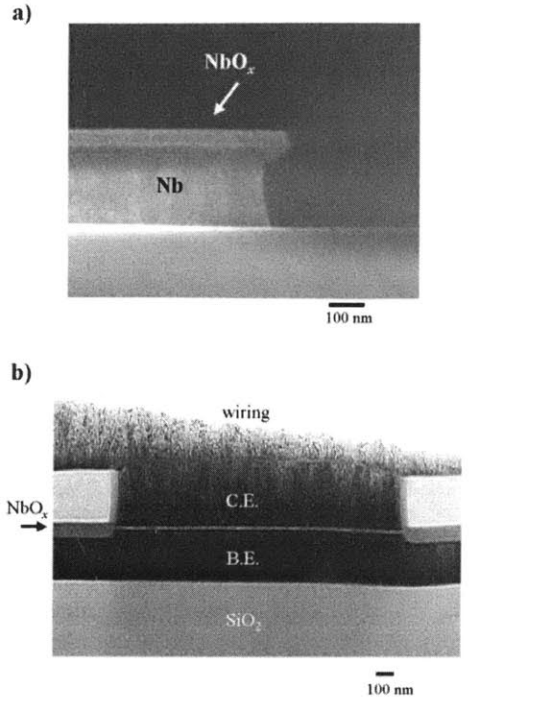

Fig. 3. a) SEM image of NbO_x grown on Nb layer. b) TEM image of an anodized junction showing clearly the sealing of the junction edge by NbO_x. Note the clean interface between the counter-electrode and wiring layer where the NbO_x has been removed by CMP.

resistance R_n at room temperature. We calculated the critical current I_c of a junction from the R_n measurements for a large quantity of junctions distributed across an entire wafer using an automatic probing station. From these measurements we determined critical-current-density uniformity for several anodized/unanodized wafer pairs where, for each pair, the trilayers were fabricated together.

A. Room Temperature Measurements

Room temperature measurements using specially designed test structures were used to determine the overall critical-current-density across the wafer. We employed four-point cross-bridge Kelvin resistor (CBKR) structures to determine the normal-state resistance R_n of the Josephson junction. Previous studies have shown that the critical current of a junction can be accurately determined from the room-temperature R_n measurements [11]. The room-temperature R_n was measured using an automated probing station (Ruckers and Kolls 683 A Semi-Automatic Wafer Prober). In order to prevent damaging our junctions, we took two precautions: First, to prevent electrostatic discharge (ESD) damage, the probing station pins were grounded before making contact to the junction pads. Second, we used the "make before break" method before applying current through the junction. This method consisted of introducing a resistive path parallel to the junction such that the current ran mainly through this resistor. This current path to the junction was then opened so current then flowed through the junction. This method prevented voltage from building up across the junction during the measurement.

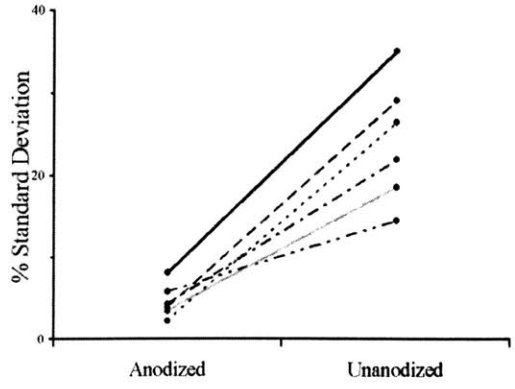

Fig. 4. Comparison of cross-wafer critical-current-density standard deviation of anodized/unanodized wafer pairs. The wafers shown have J_c values ranging between 10^2 A/cm^2 and 10^3 A/cm^2. Lines connect data points on wafers whose trilayers were deposited together.

From the R_n values obtained at room temperature, we determined the approximate value of the critical current I_c of the junction. From the known junction area (10×10 μm^2, we then extracted the J_c value. Fig. 4 shows the J_c percent standard deviation across a wafer for six wafer pairs. Each pair was fabricated together, the only difference being the presence or absence of anodization. The percent standard deviation of J_c was typically $\sim 5\%$ for anodized wafers but $> 15\%$ for unanodized wafers. Overall, unanodized wafers had a factor of ~ 3 higher standard deviation compared to anodized wafers. Error in room-temperature R_n measurements due to the finite lead resistance and sizing errors could not account for this difference in critical-current-density uniformity [11].

IV. Analysis and Discussion

Our results suggest that there exists in-process modification of J_c that is avoided or diminished by anodization. The wafer pairs we examined were simultaneously subjected to the same highly uniform oxidation process involved in producing the tunneling barrier, therefore making it unlikely for one wafer to differ significantly in J_c uniformity from the other. Isolating the cause of the modification remains difficult since many subsequent processing steps are required to produce useful junctions. Possible sources of damage or contamination of the junction barrier include: stress in the Nb film, plasma, and/or chemical sources (photoresist/developer, phosphoric acid, CMP slurry). Clearly, anodization reduces cross-wafer I_c spreads of large junctions ($> 2 \times 2$ μm^2) suggesting that the anodic oxide layer retards attack of the junction. However, from separate room temperature and low temperature measurements, we have determined that anodization does not improve cross-wafer spread of small junctions ($< 2 \times 2$ μm^2) since small junction I_c is mainly dominated by sizing variation rather than J_c variation and anodization does not appear to affect sizing variation.

V. Conclusion

Our central work involves the development and incorporation of an anodization process into an existing Nb superconducting fabrication process and demonstrating its effect on J_c uniformity. We initially developed the anodization procedure, then determined how to modify the existing standard process to include the anodization step. This work required thickness metrology development involving spectral reflectometry measurements, SEM/TEM imaging and step-height profile measurements. From the normal-state resistance measurements of junctions, we then determined the critical-current-density across anodized/unanodized wafer pairs. Our results show that anodization allows for higher J_c uniformity across anodized wafers than unanodized wafers. This enables us to produce the small ($< 1\%$) J_c cross-chip variation that is required for RSFQ circuits, and to increase the quantity of chips per wafer with the desired J_c.

Acknowledgment

The authors would like to thank the Lincoln Laboratory Analog Device Technology Group and X. Meng for helpful comments and discussion, T. Weir and G. Fitch for help with room temperature testing, and D. Baker and the Lincoln Laboratory Microelectronics Laboratory for help with fabrication.

References

[1] X. Meng, L. Zheng, A. Wong, and T. Van Duzer, "Micron and submicron Nb/Al-AlO$_x$/Nb tunnel junctions with high critical current densities," *IEEE Trans. Appl. Supercond.*, vol. 11, no. 1, pp. 365–8, March 2001.

[2] H. Nakagawa, G. Pepe, H. Akoh, L. Frunzio, R. Cristiano, E. Esposito, S. Pagano, G. Peluso, A. Barone, and S. Takada, "A new fabrication process of superconducting Nb tunnel junctions with ultralow leakage current for X-ray detection," *Jpn. J. Appl. Phys.*, pt. 1, vol. 32, no. 10, pp. 4535–7, October 1993.

[3] S. Morohashi and S. Hasuo, "Experimental investigations and analysis for high-quality Nb/Al-AlO$_x$/Nb Josephson junctions," *J. Appl. Phys.*, vol. 61, no. 10, pp. 4835–49, May 1987.

[4] K. K. Berggren, E. M. Macedo, D. A. Feld, and J. P. Sage, "Low T_c superconductive circuits fabricated on 150-mm-diameter wafers using a doubly planarized Nb/AlO$_x$/Nb process," *IEEE Trans. Appl. Supercond.*, vol. 9, no. 2, pp. 3271–4, June 1999.

[5] J. L. Vossen and W. Kern, *Thin Film Processes II.* Massachusetts: Academic Press Inc., 1991, pp. 251–5.

[6] X. Meng, A. Bhat, and T. Van Duzer, "Very small critical current spreads in Nb/Al-AlO$_x$/Nb integrated circuits using low-temperature and low-stress ECR PECVD silicon oxide films," *IEEE Trans. Appl. Supercond.*, vol. 9, no. 2, pp. 3208–11, June 1999.

[7] H. Kroger, L. N. Smith, and D. W. Jillie, "Selective niobium anodization process for fabricating Josephson tunnel junctions," *Appl. Phys. Lett.*, vol. 39, no. 3, pp. 280–2, 1981.

[8] M. Bhushan *et al.*, "Nb-AlO$_x$-Nb SNAP technology for 125 mm wafers developed in partnership with silicon technology," in *Superconductive Devices and Their Applications in Proc. SQUID '91 Conf.*, H. Koch and H. Luebbig, Eds., New York, 1992, pp. 265–70.

[9] M. Bhushan and E. M. Macedo, "Nb/AlO$_x$/Nb trilayer process for the fabrication of submicron Josephson junctions and low noise dc SQUID's," *Appl. Phys. Lett.*, vol. 58, no. 12, pp. 1323–5, 1991.

[10] T. Imamura and S. Hasuo, "Characterization of Nb/AlO$_x$-Al/Nb junction structures by anodization spectroscopy," *IEEE Trans. Magn.*, vol. 25, pp. 1131–4, 1989.

[11] K. K. Berggren, M. O'Hara, J. P. Sage, and A. H. Worsham, "Evaluation of critical current density of Nb/Al/AlO$_x$/Nb josephson junctions using test structures at 300 K," *IEEE Trans. Appl. Supercond.*, vol. 9, no. 2, pp. 3236–9, June 1999.

dc measurements of macroscopic quantum levels in a superconducting qubit structure with a time-ordered meter

D. S. Crankshaw, K. Segall, D. Nakada, and T. P. Orlando
Department of Electrical Engineering and Computer Science, Massachusetts Institute of Technology, Cambridge, Massachusetts 02139, USA

L. S. Levitov
Department of Physics, Massachusetts Institute of Technology, Cambridge, Massachusetts 02139, USA

S. Lloyd
Department of Mechanical Engineering, Massachusetts Institute of Technology, Cambridge, Massachusetts 02139, USA

S. O. Valenzuela, N. Markovic, and M. Tinkham
Department of Physics, Harvard University, Cambridge, Massachusetts 02138, USA

K. K. Berggren
Massachusetts Institute of Technology Lincoln Laboratory, Lexington, Massachusetts 02420, USA
(Received 1 October 2003; published 22 April 2004)

dc measurements are made in a superconducting, persistent current qubit structure with a time-ordered meter. The persistent-current qubit has a double-well potential, with the two minima corresponding to magnetization states of opposite sign. Macroscopic resonant tunneling between the two wells is observed at values of energy bias that correspond to the positions of the calculated quantum levels. The magnetometer, a superconducting quantum interference device, detects the state of the qubit in a time-ordered fashion, measuring one state before the other. This results in a different meter output depending on the initial state, providing different signatures of the energy levels for each tunneling direction.

DOI: 10.1103/PhysRevB.69.144518 PACS number(s): 74.50.+r

I. INTRODUCTION

The study of mesoscopic quantum effects in superconductors is motivated both by interest in the extension of quantum mechanics to the macroscopic world[1] and by the possibility of constructing a quantum information processor.[2] Macroscopic quantum effects, such as resonant tunneling,[3] quantum superposition states,[4,5] and time-dependent coherent oscillations,[4–8] have recently been observed. In these experiments, measurements were made on flux,[4,5] charge,[6] and current.[7,8]

One particular superconducting system that has been under study is the persistent-current qubit (PC qubit), a superconducting ring interrupted by three Josephson junctions.[9] When an external magnetic flux bias near one-half of a flux quantum ($\Phi_0 = h/2e$) is applied, the PC qubit has two stable classical states of electrical current circulating in one direction or the other, resulting in measurable opposing magnetizations. It can be modeled as a double-well potential in a three-dimensional potential landscape (one dimension for each junction's phase variable, or three other variables which span the space), where the minimum of each well corresponds to one of these two magnetization states. Depending on the parameters, the system may have multiple quantum energy levels in one of the two wells, where each level has approximately the same magnetization. Energy levels in a similar system, the radio-frequency superconducting quantum interference device (rf SQUID), have been measured by studying resonant tunneling between the two wells.[3] Experiments on an rf SQUID have used a separate, damped SQUID magnetometer as the meter. This approach gives a continuous readout of the magnetization, but also couples unwanted dissipation into the system.

In a recent paper, we showed how coupling an underdamped dc SQUID magnetometer to a PC qubit resulted in time-ordered measurements of the two states, where one state is observed before the other.[10] In those experiments, we studied the classical, thermally driven regime of operation. In the present paper, we detail the effects of a time-ordered meter on the dc measurements of the PC qubit in the quantum regime. The quantum levels are detected by observing resonant tunneling between the two wells. The positions of the energy levels agree well with calculations of the qubit energy band structure, and the energy bias of level repulsions indicates where tunneling occurs between the two wells. While the PC qubit has inherent symmetry between the two states, the time ordering of the measurements causes an asymmetry in the meter output. We demonstrate this asymmetry, and also show how the meter shifts the positions of the energy levels as a function of the SQUID current bias. Finally, by measuring the width and height of the tunneling peaks as a function of the SQUID ramp rate, we find a fitted value of the intrawell relaxation of order microseconds.

II. QUBIT PARAMETERS AND MEASUREMENT PROCESS

The qubit and dc SQUID are both fabricated at Lincoln Laboratory in a niobium trilayer process.[11] The circuit dia-

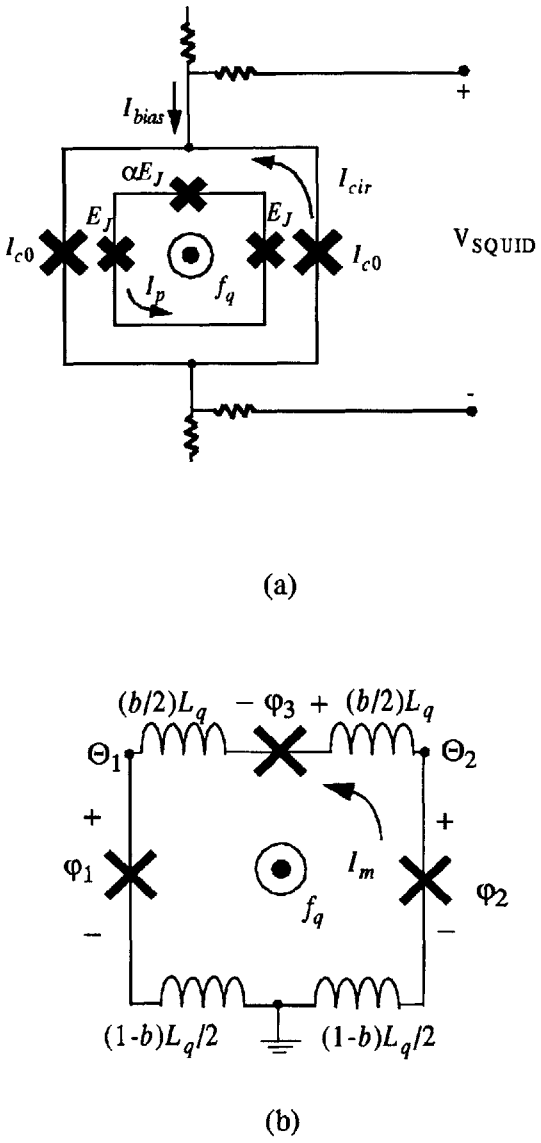

FIG. 1. (a) A circuit diagram of the qubit structure, a three-junction loop, and the two-junction SQUID. (b) The circuit diagram used to derive the quantum-mechanical model of the qubit. The inductance is distributed among the branches, the inductance on the branch of the smallest junction having a value of bL_q (symmetrically split on either side of the junction), while the inductances on the other two branches each have a value of $(1-b)L_q/2$. The node phases Θ_1 and Θ_2 are shown in the figure.

gram is shown in Fig. 1. The qubit consists of a superconducting ring interrupted by three Josephson junctions, two of which are designed to have the same critical current, I_c, and the third of which has a critical current of αI_c, where α is less than 1. The meter is a dc SQUID magnetometer which surrounds the qubit. It has two equal Josephson junctions with critical currents of I_{c0}, where $I_{c0}>I_c$. The PC qubit loop is $16\times16\ \mu m^2$ in area, and the dc SQUID is $20\times20\ \mu m^2$ in area, with self-inductances of about $L_q=30$ pH and $L_s=60$ pH, respectively. They have a mutual inductance of approximately $M=25$ pH. These inductances are calculated using FASTHENRY,[12] then refined through experimental measurements of the SQUID's response to magnetic field, as explained in the Appendix. The critical current density of the junctions is 370 A/cm^2 and the critical current of the SQUID junctions is measured to be $I_{c0}=5.3\ \mu$A, consistent with an area of 1.4 μm^2. I_c and α can be determined experimentally from our previous thermal activation studies, which give $\alpha=0.63$ and $I_c=1.2\ \mu$A.[10] These values are within the range of estimated values from the process parameters.

By changing the magnetic flux through the PC qubit, the depth of each well of the double-well potential changes, with one becoming deeper as the other becomes shallower. The energy bias (ε) is the energy difference between the minima of the two wells. (We will also use it to indicate the difference between energy levels in opposite wells, using a subscript to indicate which energy levels we are measuring the difference between.) It is periodic with frustration, f_q, which is the magnetic flux bias of the qubit in units of flux quanta. At $f_q=0.5$, the depths of the two wells are equal, and near this value the energy bias varies almost linearly with frustration, such that ε is approximately $4\pi\alpha E_J(f_q-0.5)$, where $E_J=I_c\Phi_0/2\pi$ is the Josephson energy of each of the two larger junctions of the qubit.

In our previous experiments,[10] we observed the rate of thermal activation of the qubit's phase particle (the term for the wave function of the qubit's phase) above the barrier between the two wells. At low temperatures, thermal activation is insufficient to overcome this barrier within the measurement time scale when $f_q=0.5$. In this case, hysteresis is observed, where the PC qubit remains in the state in which it is prepared until it is measured, even though this state is no longer the minimum energy state. During the measurement, the SQUID goes to its voltage state, where it oscillates, and since its oscillations are strongly coupled to the qubit, the qubit is effectively randomized. Thus the hysteresis is not observable without preparing the qubit prior to each measurement. The qubit can be prepared in a state by changing its magnetic flux bias to a value where the system has a single well and allowing the qubit to relax to its ground state, then bringing it back to the magnetic flux bias where it is measured. The qubit will remain in the state where it was prepared, either the left well (the **0** state) or the right well (the **1** state), until either thermal activation or quantum tunneling provides the opportunity to escape to the opposite well.

III. ENERGY LEVEL STRUCTURE CALCULATIONS

The full Hamiltonian for the qubit in Fig. 1(a) is given in Eq. (1),

$$H=\frac{1}{2}C_j\left(\frac{\Phi_0}{2\pi}\right)^2\dot{\varphi}_1^2+\frac{1}{2}C_j\left(\frac{\Phi_0}{2\pi}\right)^2\dot{\varphi}_2^2+\frac{1}{2}\alpha C_j\left(\frac{\Phi_0}{2\pi}\right)^2\dot{\varphi}_3^2$$
$$+E_J(1-\cos\varphi_1)+E_J(1-\cos\varphi_2)+\alpha E_J(1-\cos\varphi_3)$$
$$+\left(\frac{\Phi_0}{2\pi}\right)^2\frac{(\varphi_1-\varphi_2+\varphi_3+2\pi f_q)^2}{2L_q}. \quad (1)$$

Here C_j is the junction capacitance of each of the larger junctions, and φ_i is the phase difference across junction i. If the inductance of the qubit is small enough, the phase of the three junctions is highly confined by flux quantization, and only two independent variables are necessary to describe the Hamiltonian. The requirement for this approximation is that $\beta_L = L_q/L_J < 0.01$,[13] where L_q is the inductance of the qubit loop and L_J is the Josephson inductance of each of the larger junctions. This is not the case in our sample, where $\beta_L = 0.1$. In order to correctly solve the Hamiltonian of our device, we need to include the inductance and solve for the three-dimensional Hamiltonian. We start by making a change of variables from the phases of the three junctions to Θ_1 and Θ_2, which are node phases, and I_m, which is the current around the PC qubit loop (we later use the variable I_p to denote the persistent current in the qubit, but I_p is technically the expectation variable in each state, while I_m is the quantum variable, thus $I_p = \langle I_m \rangle$). These variables are shown in Fig. 1(b). This gives us the equalities in Eq. (2) for converting the phase variables of the junctions into Θ_1, Θ_2, and I_m,

$$\varphi_1 = \Theta_1 - \left(\frac{1-b}{2}\right) 2\pi \left(\frac{L_q I_m}{\Phi_0} + f_q\right),$$

$$\varphi_2 = \Theta_2 + \left(\frac{1-b}{2}\right) 2\pi \left(\frac{L_q I_m}{\Phi_0} + f_q\right),$$

$$\varphi_3 = \Theta_2 - \Theta_1 - (b) 2\pi \left(\frac{L_q I_m}{\Phi_0} + f_q\right). \tag{2}$$

The variable b, which describes how the self-inductance of the qubit is divided among its branches, is arbitrary so long as it is less than 1. We can define its value as $1/(1+2\alpha)$ so that it eliminates any product terms of the time derivative of I_m and the time derivative of either Θ_1 or Θ_2 in the Hamiltonian. By changing variables again, this time to $\Theta_+ = (\Theta_1 + \Theta_2)/2$ and $\Theta_- = (\Theta_1 - \Theta_2)/2$, while defining the effective masses associated with these two variables as $M_+ = 2(\Phi_0/2\pi)2C_j$ and $M_- = (2+4\alpha)(\Phi_0/2\pi)2C_j$, we get the Hamiltonian in Eq. (3),

$$H = \frac{1}{2} M_+ \dot{\Theta}_+^2 + \frac{1}{2} M_- \dot{\Theta}_-^2 + \frac{\alpha}{2+4\alpha} C_j L_q^2 \dot{I}_m^2 + E_J \Bigg\{ 2 + \alpha - 2\cos\Theta_+ \times \cos\left[\Theta_- - \left(\frac{1-b}{2}\right) 2\pi \left(\frac{L_q I_m}{\Phi_0} + f_q\right)\right] - \alpha \cos\left[-2\Theta_- - (b) 2\pi \left(\frac{L_q I_m}{\Phi_0} + f_q\right)\right]\Bigg\}. \tag{3}$$

While complex, this is numerically solvable by discretizing the variables Θ_+, Θ_-, and I_m into Θ_{+_i}, Θ_{-_j}, and I_{m_k},

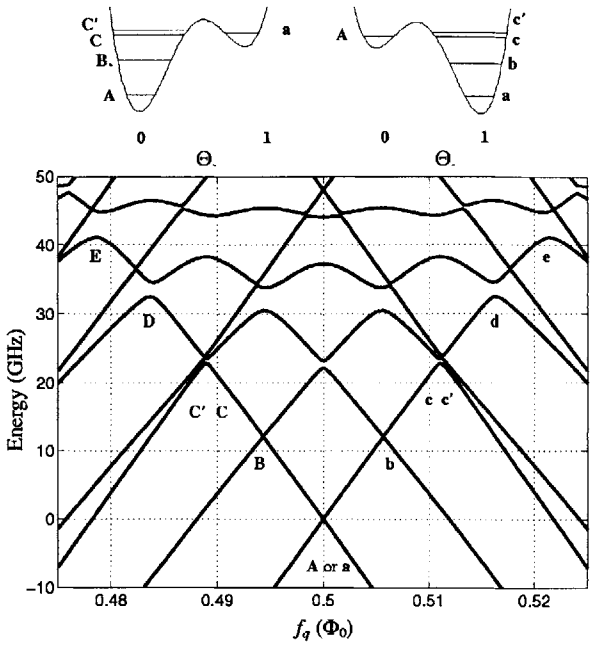

FIG. 2. An energy band diagram of the PC qubit with the parameters described in the text, with the magnetic flux bias of the qubit in units of flux quanta (f_q) as the horizontal axis. The transitions between the **0** and **1** states occur at the avoided level crossings. These are at $f_q = 0.478$, 0.483, 0.487, 0.488, 0.494, and 0.500 on the left side, labeled **E**, **D**, **C′**, **C**, **B**, and **A**, respectively. On the right side, these are at $f_q = 0.500$, 0.506, 0.512, 0.513, 0.517, and 0.522, labeled **a**, **b**, **c**, **c′**, **d**, and **e**. The energy levels in the double-well potential above the energy band diagram are likewise labeled. **C** in the energy band diagram comes from the alignment of **a** (in the right well) and **C** (in the left well), while **c** in the energy band diagram comes from the alignment of energy levels **A** and **c**. Since all the alignments are between a higher energy level in the deeper well and the lowest level in the shallow well, the avoided level crossings are designated by the label of the energy level in the deeper well.

respectively, and creating a Hamiltonian matrix whose elements are $H_{\mathbf{pq}} = \langle \Theta_{+_i} \Theta_{-_j} I_{m_k} | \hat{H} | \Theta_{+_r} \Theta_{-_s} I_{m_t} \rangle$, where **p** and **q** are indices that map onto all the permutations of **i**, **j**, **k** and **r**, **s**, **t**, respectively. $\boldsymbol{H}$ is a square matrix where each side has a length equal to the product of the number of discretized elements of Θ_+, Θ_-, and I_m. The matrix must be kept sparse in order to solve on a computer due to memory limitations, and the band structure in Fig. 2 shows the eigenvalues of this Hamiltonian matrix as the external magnetic flux bias is changed. The inclusion of self-inductance changes the energy band diagram, most significantly by reducing the level repulsion, since the barrier between the two wells is greater due to the need to overcome the qubit's self-inductance. The junction capacitance (C_j) is the most roughly estimated of the qubit's parameters, and thus serves as the sole fitting parameter for the level crossing locations. A value of 28 fF for C_j gives a good fit. The first six avoided crossings, counting outward from $f_q = 0.5$, are labeled, using **a**, **b**, **c**, **c′**, **d**, and **e** for the level crossings when f_q is greater than 0.5, and using **A**, **B**, **C**, **C′**, **D**, and **E** when f_q is less

than 0.5. **C** and **C′** (and their equivalents in the other direction, **c** and **c′**) are difficult to discern due to their proximity. Although the energy scales are such that some of the avoided level crossings appear to actually cross in this figure, there is a small amount of energy level repulsion even at $f_q=0.5$. There are multiple energy levels in each well, and each labeled level crossing corresponds to the alignment of the lowest level in one well and one of the energy levels in the other well, as is shown in the double well potentials in Fig. 2. This results in two eigenstates—a symmetric state and an antisymmetric state—spanning both wells, with an energy difference equal to the level splitting shown in the energy band diagram, allowing the classical state of the qubit to change as the phase particle oscillates between wells.

IV. RESULTS AND DISCUSSION

To determine the state of the PC qubit, we ramp the electrical current in the dc SQUID until it switches to the voltage state. The measuring dc SQUID remains in the zero-voltage state as long as the current through it is below the switching current, which is determined by the total magnetic flux through the SQUID; when it passes this current it develops a finite voltage. The nominal value of the switching current is $I_{sw0}=2I_{c0}|\cos(\pi f_S')|$, where I_{c0} is the critical current of each of the two SQUID junctions and f_S' is the total magnetic flux through the SQUID in units of flux quanta, although the SQUID may switch early due to thermal excitation or quantum tunneling of the SQUID phase particle. Since the qubit's two states have different magnetizations, the two states induce different switching currents in the SQUID: I_0 for state **0** and I_1 for state **1**. The stochastic process that describes the switching of the SQUID has a variance that is measurable but significantly smaller than the signal we are measuring (the difference between I_0 and I_1). The ramp rate is typically 4 μA/ms and the difference between I_0 and I_1 is 0.5 μA, which gives a delay of 125 μs between the polling of the **0** state and the **1** state. If the qubit is in the **0** state, the SQUID switches as soon as it arrives at I_0. If it is in the **1** state and remains there, the SQUID does not switch until it reaches I_1.

Figure 3 illustrates the observed hysteresis of the qubit. Part (a) of this figure shows the probability of measuring the qubit in each state by plotting P_1-P_0, where P_1 is the probability of finding it in state **1** and P_0 is the probability of finding it in state **0**. It also shows one-dimensional cuts of the double-well potential at different magnetic fields. The solid curve is P_1-P_0 when the system is prepared in the **1** state, while the dashed curve shows this measurement when it is prepared in the **0** state. This measurement occurs at ~20 mK bath temperature, where the thermal energy is $k_BT \approx 1.7$ μeV. Part (b) of this figure shows how the difference between the 50% point of the two curves shown in (a) (marked by the line labeled *w*) varies with temperature. We call this difference the "hysteresis width." The width is constant up to $T=200$ mK, then decreases linearly as temperature increases. The hysteresis width should not vary with temperature as long as $k_BT<\hbar\omega_0$, where ω_0 is the resonant frequency of the qubit, which is equal to 28 GHz. This gives

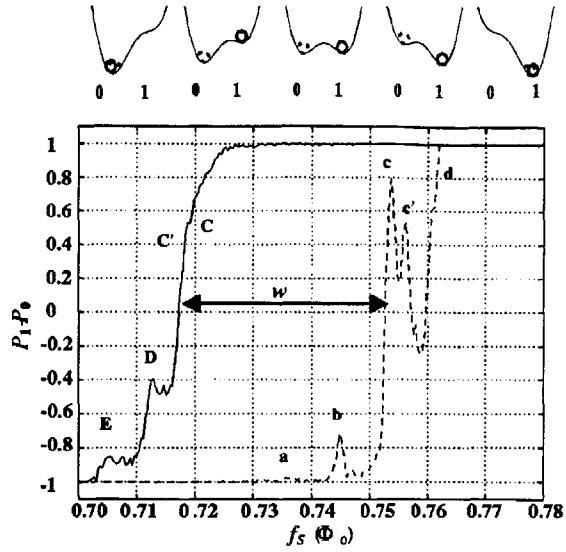

FIG. 3. (a) The hysteresis measurement at 20 mK bath temperature. Above the figure are one-dimensional cuts of the potential that show the shape of the double-well potential at the various frustrations. The plot shows the proportion of switching events where the qubit is measured in the **1** state minus the proportion where it is found in the **0** state (P_1-P_0) against the magnetic flux bias of the dc SQUID in units of flux quanta (f_S). The solid line is for a qubit prepared in the **1** state, represented in the double-well diagrams as a solid circle. The dashed line shows the measured qubit state when it is prepared in the **0** state, corresponding to the dashed circle in the double-well potential diagrams. The dashed line shows numerous peaks and dips, while the solid line's structure is less pronounced. Multiple scans over the same region produce the same results. The width of the hysteresis is labeled in this figure with a *w*. (b) As the temperature increases, the hysteresis loop closes. The points on this graph show the width of the hysteresis loop (*w*) vs temperature. It is nearly constant for low temperatures and nearly linear for higher temperatures. The line serves as a guide for the eyes.

a turnover point of 210 mK, consistent with the measurement. Thermal activation causes the qubit to change state once the barrier is on the order of k_BT, and the barrier height

changes linearly with magnetic flux bias. The hysteresis width intercepts zero at 550 mK, or 47 μeV.

The hysteresis loop closes as the temperature increases. The hysteresis width corresponds to the points where the probability of escape from the shallow well is approximately 50%, or $P_{esc}=1-e^{-\Gamma_{th}t}=0.5$. Since the ramp time is on the order of 1 ms, we can calculate Γ_{th} to be approximately 700. Thermal activation gives an escape rate of $\Gamma_{th}=(7.2\Delta U\omega_0/2\pi Qk_BT)\exp(-\Delta U/k_BT)$. Calculations of the potential energy, confirmed by previous experiments, show how the barrier between the two states, ΔU, varies with the magnetic flux bias of the qubit.[10] Near $f_q=0.5$, the barrier for the qubit to make the transition from the **1** to the **0** state can be written as $\Delta U_{10}(f_q)\approx\Delta U(0.5)+2\pi\alpha E_J(f_q-0.5)$, where $2\pi\alpha E_J=9500$ μeV. $\Delta U(f_q=0.5)$ is $2\pi\alpha E_J\{2\cos^{-1}[2\sqrt{(1-\alpha)^2/3}]-\cos^{-1}[\sqrt{(1-\alpha)^2/3\alpha^2}]\}$, or about 210 μeV,[10] or 2.4 K. $\Delta U_{01}(f_q)\approx\Delta U(0.5)-2\pi\alpha E_J(f_q-0.5)$ is the barrier for the transition from **0** and **1** at the same flux bias. $\Delta U(f_q)/k_BT$, which appears in both the exponent and the prefactor, is the dominant term in Γ_{th}. The other terms in the prefactor are ω_0, the simple harmonic-oscillator frequency of the well (equal to 28 GHz), and the quality factor Q, which is 3×10^5 as calculated in Ref. 10. The value of $\Delta U(f_q)/k_BT$, which would give a Γ_{th} of 700, is 9. Referring to part (b) of Fig. 3, we can apply the values of the temperature and the barrier of the shallow well, $\Delta U(f_q)$, to the slope of the line to find the constant value of $\Delta U(f_q)/k_BT$, which is found to be 7.3, about 20% off from the theoretical value of 9.

Figure 4 shows the number of switching events at various values of current and magnetic flux bias. The horizontal axis represents the externally applied magnetic flux to the SQUID in terms of frustration, while the vertical axis corresponds to the current bias of the SQUID. The coloring indicates the number of switching events that occur at each point in the external flux bias and current bias coordinates. In the experiment, 10^3 measurements are taken at each value of external flux bias, so each vertical slice represents a histogram of these measurements. Over most of the parameter space, this figure shows that two preferred states exist, corresponding to the **1** and **0** states of the qubit. These states create two "lines" across the figure, reminiscent of the results in Ref. 14.

However, the detailed signatures of the switching events when the qubit is prepared in the **1** state [Fig. 4(a)] differ from when it is prepared in the **0** state [Fig. 4(b)], even though the energy biases are mirror images of each other around $f_q=0.5$, as shown by the double-well potentials drawn above Fig. 3(a). Figure 4(a) shows stripes in the region in between the two lines of switching currents, whereas Fig. 4(b) has no switching events in this in-between region. The two lines of switching currents in Fig. 4(b) shows islandlike regions, whereas Fig. 4(a) does not. The plots in Fig. 3, which are derived from the same data, also reflect this asymmetry. Although Figs. 4(a) and 4(b) show a range of flux bias where both states can be measured, an important difference between the two plots is the path followed by the SQUID in bias current and external magnetic field, which is illustrated by the dashed line in the two figures. Rather than

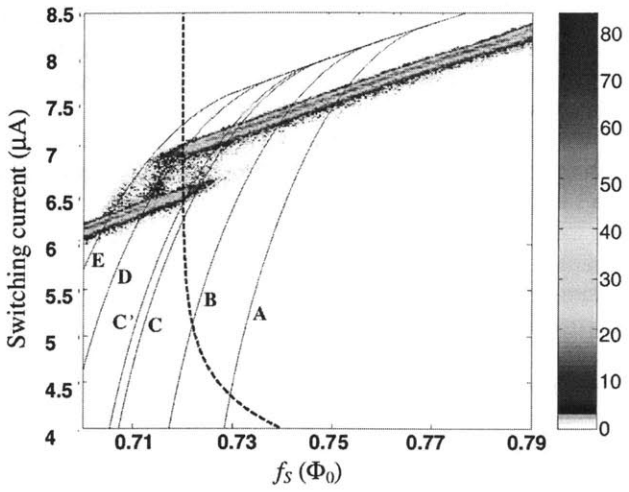

FIG. 4. (Color) (a) A plot of the switching events at various external flux biases when the qubit is prepared in the **1** state, taken at 20 mK bath temperature. Each vertical slice is a histogram of an ensemble of switching measurements taken at a fixed external flux bias, where the colors represent the number of switching events at each current bias. The horizontal axis is the external flux bias of the SQUID, f_S. The solid lines are lines of constant f_q that correspond to level crossings in the qubit labeled according to the convention in Fig. 2. The path followed when the current bias of the SQUID is ramped is not a straight vertical line, since the external flux bias is also changing due to the state preparation. The path for a representative measurement, where $f_S=0.72$, is shown by the dashed line. (b) The switching events when the qubit is prepared in the **0** state, also at 20 mK. Note that the dashed line is briefly tangential with one of the solid lines. The dashed line represents $f_S=0.753$.

being completely vertical, indicating a ramp in SQUID current while the external magnetic field is held constant, the external magnetic field also changes during the current ramp due to the preparation of the qubit state. The total magnetic

field seen by the qubit also changes due to coupling from the SQUID's circulating current. These, along with the influence of the time-ordered measurements, result in differences in the data due to macroscopic quantum tunneling.

We first consider the data in Fig. 4(a), where the system is initially prepared in the **1** state. When the qubit is prepared in the **1** state, it will remain there as long as the bias is such that the local minimum exists, unless it has some mechanism to escape this local minimum, such as thermal activation or macroscopic quantum tunneling. At 20 mK bath temperature, thermal activation is effectively frozen out, and macroscopic quantum tunneling is the dominant process; therefore, one expects to see tunneling at the locations of the energy level crossings on the left side of the band diagram in Fig. 2. The probability that the state will make a transition from **1** to **0** depends on the tunneling rate and the time that the system remains in the level-crossing region. Note that if the qubit makes the transition to the **0** state before the SQUID bias current reaches I_1 but after the current is past I_0, the SQUID switches immediately, and we record a switching event in the region between I_0 and I_1. One might expect vertical stripes to appear between I_0 and I_1 at the external flux biases corresponding to the level crossings. The observed stripes are instead curved because the total flux bias of the qubit, f_q, depends on the flux coupled from the readout SQUID as well as the externally applied flux, f_q^{ext}. The total flux biasing the qubit is $f_q = f_q^{\text{ext}} + MI_{\text{cir}}/\Phi_0$, where f_q^{ext} is the externally applied flux bias, M is the mutual inductance between the dc SQUID and the qubit, and I_{cir} is the circulating current in the SQUID. The circulating current in the dc SQUID decreases as the bias current increases. The circulating current is calculated from the Josephson equations of a SQUID with a finite self-inductance to be $I_{\text{cir}} = I_{c0}\sin(\pi f_S')\sqrt{1 - I_{\text{bias}}^2/[2I_{c0}\cos(\pi f_S')]^2}$, where f_S' is the effective flux bias of the SQUID, which follows the equation $f_S' = f_S + MI_p/\Phi_0 + L_S I_{\text{cir}}/\Phi_0$. Here f_S is the externally applied flux bias to the dc SQUID and L_S is the self-inductance of the SQUID. I_p is the persistent current in the qubit, which is nearly constant at $\alpha I_c = 760$ nA, and whose sign depends on the state in which the qubit is prepared. The appearance of I_{cir} in f_S' requires that the circulating current be solved self-consistently. This calculation shows that the qubit's effective flux bias approaches the externally applied flux as it moves closer to the switching current. Figure 5 shows how f_q changes as the current is ramped. Lines of constant effective flux bias are drawn in Fig. 4(a) and the stripes in the switching events match up with these lines of constant f_q. Furthermore, the lines of f_q that match up to the stripes indicate the effective flux biases where the level crossings occur in the qubit, and these stripes compare well to the calculated level crossings of the qubit (shown in Fig. 2) based on the parameters we obtained from thermal activation experiments.[15] By ramping the bias current more slowly, the system spends more time near the level crossings that have a smaller tunneling rate and they show up more clearly; in this way, all the level crossings have been mapped out and show all the expected energy levels.[16] The effect of the ramp rate is discussed further below.

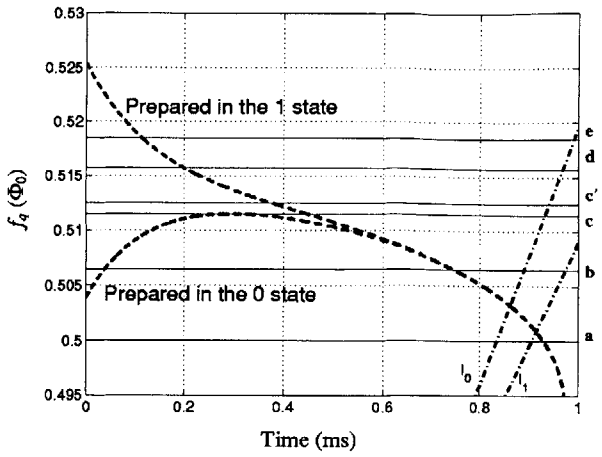

FIG. 5. The trajectory followed by f_q during the SQUID bias current ramp when $f_S = 0.753$ ($f_S = 0.753$ would correspond to $f_q = 0.469$ if the qubit were not influenced by the circulating current in the SQUID). The solid lines are level crossings of the qubit (labeled according to the convention in Fig. 2), while the dashed lines are the paths followed when the qubit is prepared in the **0** state and in the **1** state. The plateau that occurs when the qubit is prepared in the **0** state causes sharp peaks in the data due to the time during which the qubit flux bias lingers at a level crossing. The dashed-dotted lines are the times at which the switching currents for states **0** and **1** are reached for each value of f_q.

We now consider the data in Fig. 4(b), where the qubit is initially prepared in the **0** state. If the qubit remains in the **0** state, then the SQUID switches to the voltage state at I_0. The qubit cannot change from the **0** state to the **1** state after I_0, since by that point the SQUID will already have switched. If there is a transition from **0** to **1**, this must happen before the qubit reaches I_0. There are no observed switching events when the current bias is between I_0 and I_1, indicating that once it makes the transition from **0** to **1** it does not return. This is expected if after tunneling into one of the higher energy levels of the deeper well, it relaxes to a lower energy state where it is no longer in alignment with the energy level of the shallow well. Figure 6(a) shows the same data as Fig. 4(b), but simplified to the probability of finding the qubit in each state, $P_1 - P_0$. The large population shift in Fig. 4(b) at $f_S = 0.755$ is represented in Fig. 6(a) by the peak labeled **c**. Slowing down the measurement has a noticeable effect when the qubit is prepared in the **0** state, shown by how the peaks grow larger from part (a) to (b) while maintaining their position, indicating that the probability of transition grows due to the slowing of the SQUID ramp rate. This suggests that the tunneling rate from the **0** to **1** state is comparable to the time over which the levels are near alignment in the SQUID ramp. If the rate were much faster, then all the population would tunnel to the **1** state. If it were much slower, then none of the population would tunnel.

Recall that the flux bias of the qubit is $f_q = f_q^{\text{ext}} + MI_{\text{cir}}/\Phi_0$. Since I_{cir} changes as the SQUID is ramped, and f_q^{ext} is pulsed when the qubit is prepared, f_q is a function of time. In the qubit's preparation, the external magnetic field is pulsed in either the positive direction (to prepare it in the **1**

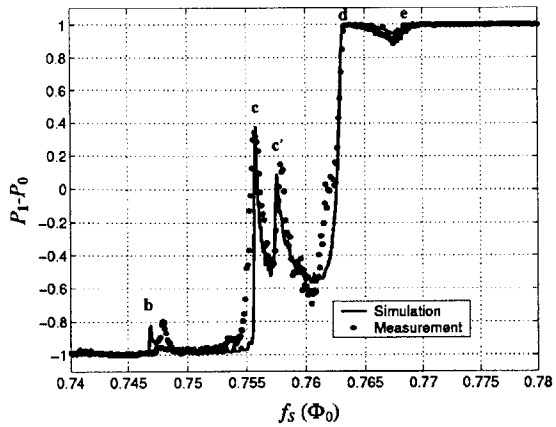

FIG. 6. The qubit state when the SQUID is ramped at a rate of (a) 4 μA/ms and (b) 0.8 μA/ms. The solid lines correspond to the theoretical model, while the solid circles are actual data points. The two show reasonably good agreement. The slower ramp rate results in a higher probability that the qubit will move to the **1** state, as is made clear by the growing peaks. The oscillations in (b) between $f_S = 0.748$ and 0.755 are artifacts of the numerical simulation. They decrease as resolution is increased, but resolution is limited by computer memory constraints. The peak labels correspond to the avoided crossings indicated in Fig. 2.

well) or the negative direction (to prepare it in the **0** well). It returns from the preparation while the SQUID's bias current is ramping. The change in I_{cir} during the SQUID ramp is the same regardless of the well in which the qubit is prepared. Thus, when the qubit is prepared in the **1** state, the two factors sum, while preparation in the **0** state causes the two factors to oppose one another. In the case of preparation in the **0** state, the state preparation and the MI_{cir} magnetic fields balance for roughly 50 μs, where the flux bias of the qubit is nearly constant. This is seen in Fig. 5. When prepared in the **1** state, the curve shows a continuous change in f_q, while f_q plateaus briefly when the qubit is prepared in the **0** state. If this plateau corresponds to an energy bias where there is a high rate of quantum tunneling between the wells, this results in a strong probability of tunneling which gives a sharp peak in the measured data ($P_1 - P_0$).

V. SIMULATIONS OF TRANSITIONS

To simulate the effect of the SQUID current bias ramp on the state of the qubit, an equation for the tunneling rate is needed. These measurements resemble those taken in Ref. 3 and described theoretically in Ref. 17 to give an equation for the rate of transition from the lowest energy level in one well to a high energy level in the other,

$$\tau_i^{-1} = \frac{\Delta_i^2 \Gamma_i}{2\Delta_i^2 + \Gamma_i^2 + 4\varepsilon_i^2}, \tag{4}$$

where τ_i^{-1} is the transition rate for level crossing i, Δ_i and ε_i are the tunnel splitting and energy bias of the specific level crossing, respectively, and Γ_i is the rate at which the qubit relaxes from the high energy level in the deeper well to one of the lower energy levels. The transition is not considered complete without this decay, which prevents the phase particle from returning to the original state. Δ_i is a function of the quantum model of the qubit, and can be calculated from the parameters that we already know. ε_i, the energy bias, is the energy difference between the energy levels in either well. This is equal to $4\pi\alpha E_J(f_q - f_i)$, where f_i is the position, in magnetic flux bias, of the individual level crossing we are considering. We will approximate Γ_i to be a constant for each level crossing. This relaxation to the lower energy levels is the fitting parameter, with the guideline that the higher the energy level, the more quickly it should relax. Running a simulation of the transition probability as f_q changes during the SQUID current bias ramp gives Figs. 6(a) and 6(b), showing a match between the theoretical model and the experiment at two different ramp rates. Using this model with theoretically calculated numbers for Δ_i, the fitted values for Γ_i are $(13\ \mu s)^{-1}$ for the first excited state, $(15\ \mu s)^{-1}$ for the second, $(75\ \mu s)^{-1}$ for the third [which corresponds to a transverse mode of the oscillator and is weakly coupled to the other energy levels], $(1\ \mu s)^{-1}$ for the fourth, and $(1\ \mu s)^{-1}$ for the fifth. These are long decay times for intrawell relaxation. Recent spectroscopy data also suggest an intrawell relaxation time on the other of tens of microseconds.[18] It should be noted that the theory allows some trade-off between Δ_i and Γ_i, so that a smaller Δ would correspond to a faster relaxation time. Environmental fluctuations may effectively decrease Δ_i while increasing Γ_i, implementing this trade-off. While we modeled this reduction in Δ_i using Wilhelm's formulation,[19] the exact amount is necessarily uncertain since it depends on the total environment of the qubit, which we cannot directly observe.

There are several strong peaks in these data, including two that are right next to each other. In the quantum model of the qubit, the only point that would give two level crossings so close together would be due to a transverse mode of the three-dimensional well, which produces an energy level of the first excited state in the Θ_+ direction near the energy level as the second excited state in the Θ_- direction. We presume that we are able to observe this mode only because of an asymmetry in the two larger junctions, due to fabrication variances, since perfectly symmetric junctions would

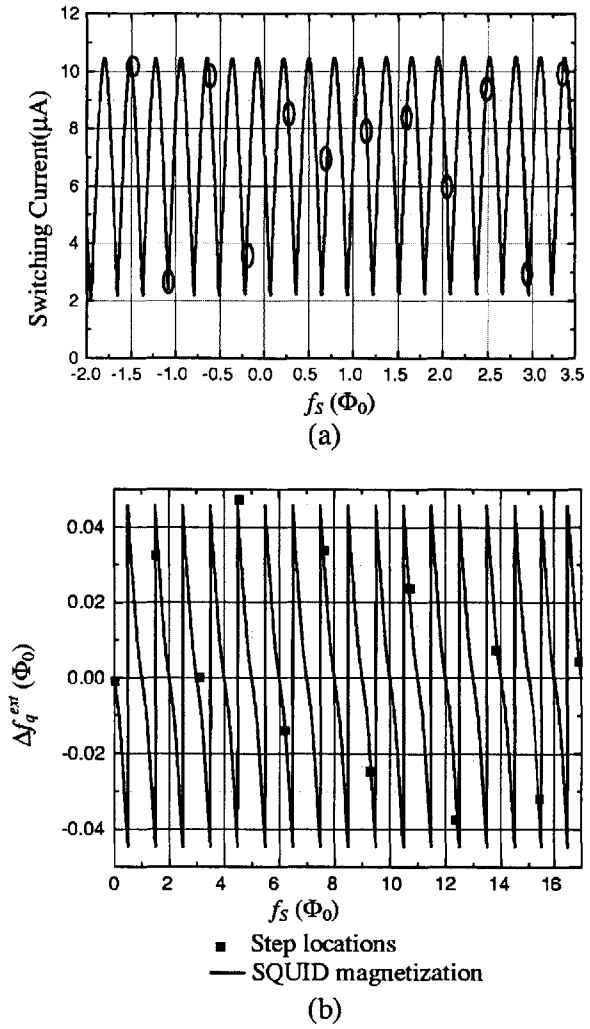

FIG. 7. (a) This is the dc SQUID switching current curve, which approximately follows $I_{sw0}=2I_{c0}|\cos(\pi f_S')|$. The locations of the qubit steps are circled. The dc SQUID switching current is periodic with magnetic field, while the qubit step is nearly periodic. (b) The solid squares represent the deviations of the measured qubit step locations from a perfect periodicity of 1.53 SQUID periods per qubit period, while the solid line shows the magnetic field from the SQUID's circulating current which couples to the qubit. This is periodic with the SQUID's frustration, and accounts for the deviations from perfect periodicity.

not produce a coupling between the transverse mode energy level in the deep well and the lowest state in the shallow well.

Using data from preparation in both states, we have observed energy levels within each well, which are separated from the ground state by frequencies of 28, 53, 60, and 72 GHz. This is measured from the location of the stripes when prepared in the **1** state and the location of the peaks when prepared in the **0** state, using the estimation that $\varepsilon \approx 4\pi\alpha E_J(f_q-0.5)$. The locations of these level crossings agree well with the energy band diagram in Fig. 2, which is calculated by numerically finding the eigenstates of the Hamiltonian.

VI. SUMMARY

In summary, we have observed macroscopic quantum tunneling in a persistent current qubit. The observed stripes when the qubit is prepared in the **1** state, even more than the distinct variations in the state populations when it is prepared in the **0** state, indicate quantum level crossings of states in the qubit's wells. We used these observed stripes and variations to determine E_C, our only unknown parameter after the results in Ref. 10, so that the quantum simulation gives the same crossings as those measurements. Once the location of the level crossings was determined, the probability of tunneling led to an estimate of the intrawell relaxation times in the tens of microseconds. Experiments are underway to observe coherent oscillations between the states.

ACKNOWLEDGMENTS

The authors would like to thank B. Singh, J. Lee, J. Sage, E. Macedo, and T. Weir for experimental help, and L. Tian and W. D. Oliver for useful discussions. The authors would also like to thank the staff of the MIT Lincoln Laboratory Microelectronics Laboratory for their assistance in sample fabrication. This work is supported in part by the AFOSR Grant No. F49620-01-1-0457 under the DOD University Research Initiative on Nanotechnology (DURINT) and by ARDA. The work at Lincoln Laboratory was sponsored by the Department of Defense under the Department of the Air Force Contract No. F19628-00-C-0002. Opinions, interpretations, conclusions, and recommendations are those of the authors and not necessarily endorsed by the Department of Defense.

APPENDIX:

Calculating the mutual inductance between the dc SQUID and the qubit is straightforward. The self-inductance of the SQUID can be determined from the transfer function of magnetic flux to switching current. From these values, we can calculate the circulating current in the SQUID as it varies with frustration. The shape of this curve, especially its minimum and any bimodal features due to multiple wells in its potential, tells us the value of $\beta_{L,S}=L_S/L_{J,S}$, the ratio of the SQUID's self-inductance to its Josephson inductance. Figure 7(a) shows the periodicity with which the qubit step appears in the SQUID transfer function. Since the SQUID is 1.53 times the size of the qubit, the step should appear at every 1.53 periods in the SQUID curve. This periodicity arises because, while both the SQUID and the qubit have a periodicity of Φ_0, the SQUID receives more flux due to its larger size. However, the qubit is not perfectly periodic, as is shown in Fig. 7(b), where the points mark Δf_q^{ext}, the difference between the qubit step's position and where it would appear if it occurred with perfect periodicity. This deviation indicates that there are sources of magnetic field other than that applied by the external magnet, the strongest of which is the field coupled to the qubit by the circulating current in the dc SQUID. (The SQUID is also influenced by the circulating current in the qubit, but since this is only one-seventh of the value of the circulating current in the SQUID, it can be

safely neglected.) The total field seen by the qubit is $f_q = f_S/1.53 + MI_{cir}/\Phi_0$, where f_S is the frustration of the SQUID from the externally applied field and I_{cir} is the circulating current in the SQUID. Thus $\Delta f_q^{ext} = f_q - f_S/1.53 = MI_{cir}/\Phi_0$. If we use a least-squares fit to find a value of M that causes MI_{cir}/Φ_0 to intersect the Δf_q^{ext} data points, we can solve for M, which we find to be about 25 pH. This produces the curve in Fig. 7(b) that intersects the data points.

[1] A. J. Leggett and A. Garg, Phys. Rev. Lett. **54**, 857 (1985).

[2] S. Lloyd, Science **261**, 1569 (1993).

[3] R. Rouse, S. Han, and J. E. Lukens, Phys. Rev. Lett. **75**, 1614 (1995).

[4] J. R. Friedman, V. Patel, W. Chen, S. K. Tolpygo, and J. E. Lukens, Nature (London) **406**, 43 (2000).

[5] C. H. van der Wal, A. C. J. ter Haar, F. K. Wilhelm, R. N. Schouten, C. J. P. M. Harmans, T. P. Orlando, S. Lloyd, and J. E. Mooij, Science **290**, 773 (2000).

[6] Y. Nakamura, Y. A. Pashkin, and J. S. Tsai, Nature (London) **398**, 786 (1999).

[7] J. M. Martinis, S. Nam, J. Aumentado, and C. Urbina, Phys. Rev. Lett. **89**, 117901 (2002).

[8] Y. Yu, S. Han, X. Chu, S. Chu, and Z. Wang, Science **296**, 889 (2002).

[9] J. E. Mooij, T. P. Orlando, L. Levitov, L. Tian, C. H. van der Wal, and S. Lloyd, Science **285**, 1036 (1999).

[10] K. Segall, D. Crankshaw, D. Nakada, T. P. Orlando, L. S. Levitov, S. Lloyd, N. Markovic, S. O. Valenzuela, M. Tinkham, and K. K. Berggren, Phys. Rev. B **67**, 220506 (2003).

[11] K. K. Berggren, E. M. Macedo, E. M. Feld, and J. P. Sage, IEEE Trans. Appl. Supercond. **9**, 3271 (1999).

[12] M. Kamon, M. J. Tsuk, and J. K. White, IEEE Trans. Microwave Theory Tech. **42**, 1750 (1994).

[13] D. S. Crankshaw and T. P. Orlando, IEEE Trans. Appl. Supercond. **11**, 1006 (2000).

[14] H. Takayanagi, H. Tanaka, S. Saito, and H. Nakano, Phys. Scr., T **T102**, 95 (2002).

[15] While Ref. 10 accurately gave us the values of E_J, α, and Q, the value of E_C was not as well determined. These measurements show us the location of the level crossings in Fig. 4(a). We can determine the value of E_C that gives these energy biases for the level crossings, which we find to be 3 μeV, also giving us C_j as 28 fF.

[16] D. S. Crankshaw, Ph.D. thesis, MIT (2003).

[17] D. V. Averin, J. R. Friedman, and J. E. Lukens, Phys. Rev. B **62**, 11 802 (2000).

[18] Y. Yu, D. Nakada, Janice C.Lee, Bhuwan Singh, D. S. Crankshaw, T. P. Orlando, K. K. Berggren, and W. D. Oliver, Phys. Rev. Lett. **92**, 117904 (2004).

[19] F. K. Wilhelm, Phys. Rev. B **68**, 060503 (2003).

Energy Relaxation Time between Macroscopic Quantum Levels in a Superconducting Persistent-Current Qubit

Yang Yu, D. Nakada, Janice C. Lee, Bhuwan Singh, D. S. Crankshaw, T. P. Orlando, and Karl K. Berggren
Massachusetts Institute of Technology, Cambridge, Massachusetts 02139, USA

William D. Oliver
MIT Lincoln Laboratory, Lexington, Massachusetts 02420, USA
(Received 28 October 2003; published 18 March 2004)

We measured the intrawell energy relaxation time $\tau_d \simeq 24$ μs between macroscopic quantum levels in the double well potential of a Nb persistent-current qubit. Interwell population transitions were generated by irradiating the qubit with microwaves. Zero population in the initial well was then observed due to a multilevel decay process in which the initial population relaxed to lower energy levels during the driven transitions. The decoherence time, estimated from τ_d within the spin-boson model, is about 20 μs for this configuration with a Nb superconducting qubit.

DOI: 10.1103/PhysRevLett.92.117904 PACS numbers: 03.67.Pp, 03.65.Yz, 85.25.Cp, 85.25.Dq

Recent successes with superconducting qubits (SQs) have enhanced the feasibility of implementing quantum computing (QC) with Josephson devices [1–9]. Rabi oscillations, which are a preliminary requirement of QC, have been reported in charge, phase, and flux qubits [3–8]. However, the systematic experimental investigation of decoherence, which is a key issue for SQs, is sparse so far due to the challenge of the time resolution of the measurement. Although long decoherence times have been demonstrated in some special configurations [4,5,8,10], the limiting source of decoherence in the SQs remains unidentified. On the other hand, the decoherence time for SQs, including energy and phase relaxation times, is predicted to be proportional to the level of dissipation, which results from the coupling between the qubits and the environment [11,12]. Therefore, quantifying the dissipation is extremely useful in the design of qubits from various new materials, because it indicates whether the dissipation is at least low enough to make error-tolerant QC feasible. Previous methods to determine the dissipation of devices are either applicable at relatively high temperatures [10] or rely on indirect measurements of switching probabilities [13]. In addition, all long decoherence times (~1 μs) reported have been obtained in NbN and Al SQs [4,5,8,10]. It is important to know whether a promising decoherence time can be achieved in Nb-based SQs, which has a more mature fabrication capability. In this Letter, we present time-resolved measurements of the intrawell relaxation time τ_d in a Nb persistent-current (PC) qubit. We found that $\tau_d \simeq 24$ μs. The corresponding phase-decoherence time within a spin-boson model (SBM) is inferred to be longer than 20 μs. These long decoherence times indicate a strong potential for QC employing Nb-based SQs.

A PC qubit is a superconducting loop broken by three underdamped Josephson junctions (JJs) [Fig. 1(a)]. Two JJs are designed to have the same critical current, and the third one is designed to be α times smaller. For $0.5 < \alpha < 1$ and with an externally applied magnetic field close to a half-flux quantum $\Phi_0/2$, the system is analogous to a particle in a two-dimensional potential well with eigenenergies calculated in Ref. [14]. However, the lowest relevant states effectively reflect a particle in a one-dimensional double-well potential with quantized energy levels shown in Fig. 1(b), and whose classical states in each well correspond to macroscopic persistent currents of opposite sign [15]. The potential shown in Fig. 1(b) can be tilted by changing the frustration f_q, the magnetic flux threading the loop in units of Φ_0. The two classical states are coupled via quantum tunneling through the barrier between the wells. In addition, the system can interact with a monochromatic electromagnetic (microwave) field, and microwaves with frequency matching the energy level spacing can generate transitions between the two macroscopic quantum states, namely, photon-induced transitions (PITs) [2,8].

The samples used in this study were fabricated at MIT Lincoln Laboratory in a Nb trilayer process [16]. The critical current density is $J_c \sim 370$ A/cm^2. The critical currents of the large and small JJs in the qubit, determined from thermal activation studies [17], are $I_c \simeq 1.2$ and 0.75 μA, respectively ($\alpha \simeq 0.63$). The qubit energy

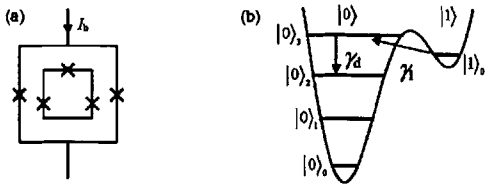

FIG. 1. (a) Schematic of the PC qubit surrounded by a readout dc SQUID. (b) Schematic of the qubit's double-well potential with energy levels for an applied frustration close to $0.485\Phi_0$. Microwaves pump the qubit from the lowest level of $|1\rangle$ ($|1\rangle_0$) to the third excited level of $|0\rangle$ ($|0\rangle_3$), then decay to the second excited level of $|0\rangle$ ($|0\rangle_2$) with a rate γ_d.

level structure calculated using qubit parameters is shown in Fig. 2 of Ref. [14]. The persistent current in the qubit loop can be read out by a dc SQUID which surrounds the qubit. For our device parameters [14,17], the persistent current will generate an additional magnetic flux of $\sim 3\ \mathrm{m}\Phi_0$ in the SQUID, resulting in a 0.3 μA change in the switching current I_{sw} of the SQUID that can be easily detected at $T < 50$ mK. The sample was mounted on a chip carrier that was enclosed in an oxygen-free-copper sample cell and thermally anchored to the mixing chamber (MC) of a dilution refrigerator. The devices were magnetically shielded by four cryoperm-10 cylinders surrounding the inner vacuum can. All electrical leads that connected the SQUID to room temperature electronics were carefully filtered by electromagnetic interference filters (at 300 K), RC filters (at 1.6 K), and copper powder filters (at 15 mK). Microwaves were injected to the qubit via a separate semirigid cryogenic coaxial cable with 20 dB attenuators at the 1 K pot and the MC. Battery-powered low-noise preamplifiers were used for all measurements. The diagnostic tests performed on JJs indicated that there was no significant extrinsic noise in our system.

Spectroscopy of the qubit energy levels was achieved using microwave pulses to produce PITs. For each measurement trial (Fig. 2), we first prepared the qubit in state $|1\rangle$ by tilting the potential (i.e., applying frustration) to a regime where the system has a single well and then waiting a sufficiently long time. After the qubit had relaxed to its ground state, the potential was tilted back to the frustration where it was to be measured. At low temperatures, the qubit will have a finite probability of remaining in $|1\rangle$, which is effectively metastable on the time scales considered in this Letter. We then applied microwaves with duration time t_{pul}, inducing transitions between states $|1\rangle$ and $|0\rangle$. After the microwaves were shut off, the bias current of the SQUID was ramped through values slightly higher than its critical current I_{c0}. The qubit state ($|0\rangle$ or $|1\rangle$) was then read out from the current at which the SQUID switched to a finite voltage state [**0** or **1** in Fig. 2(d)]. For a fixed frustration, this procedure was repeated more than 10^3 times to minimize the statistical error. A histogram of I_{sw} clearly shows the probability distribution of the qubit state occupation. Shown in Fig. 3 are contour plots of the switching-current histograms obtained by scanning the frustration at $T = 15$ mK. Each vertical slice is a histogram of I_{sw}, and the color represents the number of switching events (proportional to the switching probability). A bimodal structure in the switching-current distribution, caused by the opposite persistent current of the qubit, was observed at $f_q \sim 0.485\Phi_0$. The lower branch represents the qubit in the $|0\rangle$ state, and the upper branch represents the qubit in the $|1\rangle$ state. The substantial population in state $|1\rangle$ demonstrates that we had successfully prepared the qubit in $|1\rangle$, because, near $f_q \sim 0.485\Phi_0$, the qubit had a much higher single-well ground-state energy in $|1\rangle$ than that in $|0\rangle$.

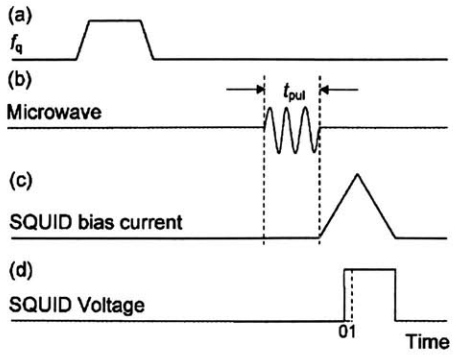

FIG. 2. Time profiles of (a) bias frustration, (b) microwave amplitude, (c) SQUID bias current, and (d) SQUID voltage for one measurement trial. **0** and **1** indicate that the qubit states ($|0\rangle$ or $|1\rangle$) result in different I_{sw}.

However, the energy barrier height and width relative to the lowest energy level of state $|1\rangle$, denoted as $|1\rangle_0$, were small enough so that the qubit had a large probability of tunneling to $|0\rangle$. The leftmost tip of the higher branch marked a fixed frustration point $f_q \approx 0.484\Phi_0$, below which it was impossible for the qubit to stay in $|1\rangle$, because the potential becomes essentially a single-well $|0\rangle$ state. Microwaves, with frequencies matching the energy difference between $|1\rangle_0$ and one of the levels of $|0\rangle$, were used to generate transitions between states $|1\rangle$

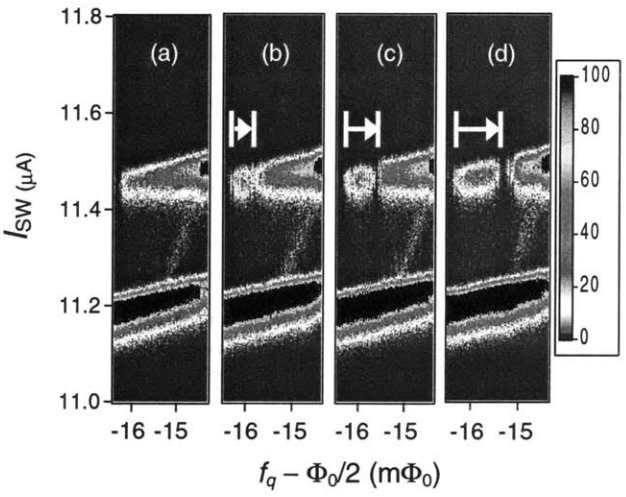

FIG. 3 (color). Contour plots of the switching current distribution (a) without microwaves and with microwaves at (b) $\nu = 6.77$, (c) 7.9, and (d) 9.66 GHz. In each plot, the leftmost tip of the upper branch corresponds to a fixed frustration point $f_q \approx 0.484\Phi_0$. Without microwave irradiation, the population in the upper branch (state $|1\rangle$) decreased continuously to zero as the frustration decreased from $\Phi_0/2$. Microwaves pumped the population from state $|1\rangle$ to state $|0\rangle$ at the resonant frustration, the bias point at which the microwave frequency matched the energy level spacing between two states. The white arrows indicate that the resonant frustration moves toward $\Phi_0/2$ with increasing microwave frequency, in agreement with the qubit energy structure [Ref. [14]].

and $|0\rangle$. The most striking feature of the contour plots is that a population "gap" (i.e., zero population region) in the $|1\rangle$ branch was created by the microwaves [Figs. 3(b)–3(d)]. With increasing microwave frequency, the gap moved away from the tip, as expected from the energy level structure [Ref. [14]]. The quantitative agreement between the gap position and the energy level structure confirmed that the gap resulted from the microwave PIT between the two macroscopic quantum states $|1\rangle_0$ and $|0\rangle_3$ (the third excited energy level of the state $|0\rangle$). We believe that the PIT here was an incoherent process, because the microwave pulse duration was 600 μs, much longer than the estimated decoherence time (0.1–100 μs) [2,8,15]. Additionally, no periodic variation of population with varying pulse duration (for long pulses) was observed. In a simple two-level system, observing such a gap would be unexpected for an incoherent transition, since the population in the lower level ($|1\rangle_0$) should always be larger than 0.5 in that case [18]. In order to address this gap phenomenon in our multilevel system, a multilevel pump-decaying model is introduced.

For simplicity we considered only three levels, the initial state $|1\rangle_0$, the $|0\rangle_3$ state to which radiation induces a transition, and the state $|0\rangle_2$ to which the population of $|0\rangle_3$ decays. More accurately, the state $|0\rangle_3$ decays to $|0\rangle_2$, $|0\rangle_1$, and $|0\rangle_0$, but, for ease of calculation, we collectively label these states as $|0\rangle_2$ with an overall effective intrawell decay rate $\gamma_d \equiv 1/\tau_d$. The temporal evolution of the three-level system under microwave irradiation is thereby described by the following three coupled rate equations:

$$\frac{dP_{10}}{dt} = -\gamma_1 P_{10} + (\gamma_1 + \gamma_2)P_{03}, \quad (1)$$

$$\frac{dP_{03}}{dt} = \gamma_1 P_{10} - (\gamma_1 + \gamma_2)P_{03} - \gamma_d P_{03}, \quad (2)$$

$$\frac{dP_{02}}{dt} = \gamma_d P_{03}, \quad (3)$$

in which P_{10}, P_{03}, and P_{02} are the occupation probabilities of levels $|1\rangle_0$, $|0\rangle_3$, and $|0\rangle_2$, respectively. γ_1 is the stimulated transition rate between $|1\rangle_0$ and $|0\rangle_3$, and γ_2 is the spontaneous relaxation rate from $|0\rangle_3$ to $|1\rangle_0$. Generally, for a given system, γ_1 is proportional to the microwave power $P_{\rm rf}$, and γ_2 can be considered to be a constant [18]. For the initial condition $P_{10}(0) = 1$, with $P_{03}(0) = P_{02}(0) = 0$, Eqs. (1)–(3) can be solved analytically. For $\gamma_1 \gtrsim \gamma_d$, which is satisfied in our experiment, the probability of finding the qubit remaining in the state $|1\rangle_0$ at $t > 1/(2\gamma_1 + \gamma_2 + \gamma_d)$ is given by

$$P_{10}(t) \approx a_1 e^{-t/\tau'}, \quad (4)$$

where a_1 depends weakly on the microwave power and can be considered as a constant in the relevant time scale,

$$\tau' \simeq (2 + \gamma_2/\gamma_1)\tau_d = (2 + \gamma_2/AP_{\rm rf})\tau_d, \quad (5)$$

and A is the coupling constant between the microwave source and the qubit. The physical picture of the three-level pump-decaying process is that microwaves populate the highest level with a population $P_{03} \propto 1/(2 + \gamma_2/\gamma_1)$, which decays to the lowest level with a rate γ_d. Therefore, the effective decay rate of the population of the initial state is given by Eq. (5), and with t sufficiently long, $P_{10}(t) \to 0$; this agrees with the experimental observations.

A significant impact of Eqs. (4) and (5) is that τ_d can be determined by measuring $P_{10}(t)$. Because $I_{\rm sw}$ of $|0\rangle$ is smaller than that of $|1\rangle$, pumping the system from state $|1\rangle$ to state $|0\rangle$ will generate a dip in the $I_{\rm sw}$ average as a function of frustration, and the dip amplitude is proportional to $1 - P_{10}$. Figure 4 shows the dip amplitude as a function of the microwave irradiation time $t_{\rm pul}$. The nominal power of the microwave source was $P_{\rm rf} = 31.3$ μW. The time constant τ', obtained from a best fit, is 130 ± 20 μs. We emphasize that τ' is not equal to τ_d, but, rather, it depends on γ_2/γ_1. For large $P_{\rm rf}$ (i.e., $\gamma_1 \gg \gamma_2$), τ' will saturate to $2\tau_d$. For $\gamma_1 \sim \gamma_2$, we are able to determine τ_d by measuring the $P_{\rm rf}$ dependence of τ'. Shown in Fig. 5 is τ' measured at various $P_{\rm rf}$. τ' saturates at about 50 μs for $P_{\rm rf} > 0.2$ mW. By adjusting γ_2/A and τ_d as fitting parameters, we obtained $\tau_d \simeq 24.3 \pm 2.7$ μs from a best fit to Eq. (5), which is consistent with dc tunneling spectroscopy measurements [14]. This long intrawell energy relaxation time is of the same order of magnitude as the reported energy relaxation times in NbN and Al-based qubits [4,5,8,10]. Note that γ_2 is another important parameter which determines interwell energy relaxation. Unfortunately, we could not directly extract γ_2 from the fitting, because we do not know the coupling constant A. Future experiments in which microwave coupling is independently characterized should allow the extraction of γ_2.

The primary effect of the environmental dissipation on the intrawell dynamics of the PC qubits is that, at low temperature ($k_B T \ll$ level spacing), the width of an excited level with energy E_n is given approximately by $\gamma_d \simeq E_n/Q$, where Q is the quality factor of the classical small

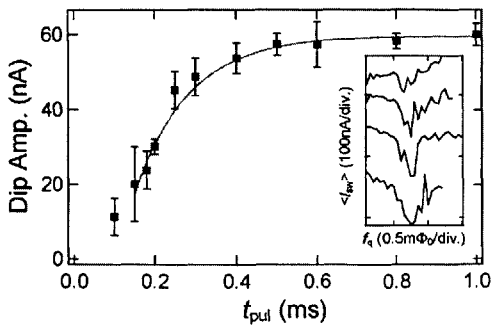

FIG. 4 (color online). The amplitude of the microwave resonant dip as a function of microwave duration $t_{\rm pul}$. The microwave frequency $\nu = 9.66$ GHz and nominal power $P_{\rm rf} = 31.3$ μW. The solid squares are experimental data and the line is a best fit to an exponential decay. The inset shows the resonant dips at $t_{\rm pul} = 0.2$, 0.5, 0.8, and 1 ms, from top to bottom.

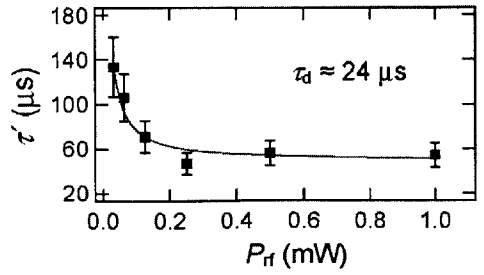

FIG. 5 (color online). τ' vs microwave power for $\nu = 9.66$ GHz. The solid line is a best fit to Eq. (5).

oscillation in the potential well [19]. From τ_d we determined $Q \sim 5 \times 10^5$, close to the value obtained from thermal activation measurements at intermediate temperatures 0.3–1.2 K [17]. Note that Q is proportional to the subgap resistance, which ideally depends on the temperature as $\sim e^{\Delta_s/k_BT}$ [20], where Δ_s is the superconducting gap voltage. The temperature independence of Q suggests the presence of additional environmental sources of dissipation [15].

This long intrawell relaxation time is important for experiments in QC in two ways. First, the lower two energy levels in the left well, $|0\rangle_0$ and $|0\rangle_1$, could themselves be used as the two qubits states, with a third state $|0\rangle_3$ used as the readout state. Because our PC qubit had no leads directly connected to it and the magnetic coupling circuit is optimally designed to lessen the effects of the electromagnetic environment, the PC qubit is much less influenced by this environment than are other similar single-junction schemes [5,6,9]. Second, if we assume that the environment can be modeled as an Ohmic bath, as in the SBM, then we can estimate the decoherence times of a PC qubit in which the qubit states are those of opposite circulating current [2,8,15]. The energy relaxation and phase-decoherence times are given in the SBM for an Ohmic environment by [11]

$$\tau_{\text{relax}}^{-1} \simeq \pi\alpha_L \sin^2\eta \Delta E/\hbar, \tag{6}$$

$$\tau_\varphi^{-1} = \tau_{\text{relax}}^{-1}/2 + 2\pi\alpha_L k_B T \cos^2\eta/\hbar, \tag{7}$$

where ΔE is the energy difference between levels in opposite wells, $\eta \approx \text{tg}^{-1}(\Delta/\Delta E)$ is the mixing angle, Δ is the tunneling amplitude between the wells, and $\alpha_L \sim 1/Q$ is the quantum damping parameter [19] which we estimate using our measured Q value. For our Nb PC qubit operating with opposite circulating currents states (for instance, biased near $f_q \approx 0.485\Phi_0$, where $\Delta \approx 2$ GHz and $\Delta E \approx 4$ GHz), a conservative estimate gives $\tau_{\text{relax}} \gtrsim 30$ μs and $\tau_\varphi \gtrsim 20$ μs at 15 mK. We emphasize that an Ohmic environment model may not adequately describe all sources of decoherence; these times must be viewed as estimates pending experimental verification. Nonetheless, for a typical Rabi frequency $\Omega = 1$ GHz, we obtained a quantum quality factor $> 10^4$, larger than the oft-quoted basic requirement for error-tolerant QC. Considering the attractiveness of Nb-based SQs from the point of view of robust and well-developed fabrication methods, these times indicate that they are a promising candidate for realizing a scalable quantum computer.

In summary, we directly measured the intrawell relaxation time of a Nb-based PC qubit by generating PITs between macroscopically distinct quantum states. A multilevel decay process was observed with an intrawell relaxation time of about 24 μs and a Q factor of greater than 10^5, indicating that these intrawell levels are well isolated from the environment and are themselves a good qubit candidate. Likewise, these measurements suggest that the flux qubits operating between wells could also have sufficient decoherence times, demonstrating good prospects for well-fabricated Nb junctions, with their more mature technology, to be used as SQs.

We thank K. Segall, B. Cord, D. Berns, and A. Clough for technical assistance and S. Valenzuela, M. Tinkham, L. Levitov, and M. Vavilov for helpful discussions. This work was supported by AFOSR Grant No. F49620-01-1-0457 under the DURINT program and by ARDA. The work at Lincoln Laboratory was sponsored by the U.S. DOD under the Air Force, Contract No. F19628-00-C-0002.

[1] J. R. Friedman *et al.*, Nature (London) **406**, 43 (2000).
[2] C. H. van der Wal *et al.*, Science **290**, 773 (2000).
[3] Y. Nakamura, Y. A. Pushkin, and J. S. Tsai, Nature (London) **398**, 786 (1999).
[4] D. Vion *et al.*, Science **296**, 886 (2002).
[5] Y. Yu *et al.*, Science **296**, 889 (2002).
[6] J. M. Martinis *et al.*, Phys. Rev. Lett. **89**, 117901 (2002).
[7] Y. A. Pashkin *et al.*, Nature (London) **421**, 823 (2003).
[8] I. Chiorescu *et al.*, Science **299**, 1869 (2003).
[9] A. J. Berkley *et al.*, Science **300**, 1548 (2003).
[10] S. Han *et al.*, Science **293**, 1457 (2001).
[11] A. J. Leggett *et al.*, Rev. Mod. Phys. **59**, 1 (1987); Y. Makhlin, G. Schön, and A. Shnirman, Rev. Mod. Phys. **73**, 357 (2001).
[12] W. H. Zurek, Phys. Today **44**, No. 10, 36 (1991).
[13] C. Cosmelli *et al.*, Phys. Rev. Lett. **82**, 5357 (1999); S. Han and R. Rouse, Phys. Rev. Lett. **86**, 4191 (2001).
[14] D. S. Crankshaw *et al.*, Phys. Rev. B (to be published).
[15] T. P. Orlando *et al.*, Phys. Rev. B **60**, 15 398 (1999).
[16] K. K. Berggren *et al.*, IEEE Trans. Appl. Supercond. **9**, 3271 (1999).
[17] K. Segall *et al.*, Phys. Rev. B **67**, 220506 (2003).
[18] D. J. Griffiths, *Introduction to Quantum Mechanics* (Prentice-Hall, Englewood Cliffs, NJ, 1995), p. 311.
[19] J. M. Schmidt, A. N. Cleland, and J. Clarke, Phys. Rev. B **43**, 229 (1991); W. Bialek, S. Chakravarty, and S. Kivelson, Phys. Rev. B **35**, 120 (1987).
[20] P. Silvestrini *et al.*, Phys. Rev. Lett. **60**, 844 (1988).

Bibliography

[1] P. Shor, "Algorithms for Quantum Computation: Discrete Log and Factoring," in *Proceedings of the 35th Annual Symposium on Foundations of Computer Science*, S. Goldwasser, Ed., IEEE Computer Society, Los Alamitos, CA, 124-34, 1994.

[2] L. Grover, "Quantum Mechanics Helps in Search for a Needle in a Haystack," *Phys. Rev. Lett.*, **79**, 325, 1997.

[3] M.A. Nielsen and I.L. Chuang, *Quantum Computation and Quantum Information.* Cambridge University Press., New York, 2000.

[4] G.P. Berman, G. D. Doolen, R. Mainieri, V. I. Tsifrinovich, "Introduction to Quantum Computers," in *Proceedings of the 35th Annual Symposium on Foundations of Computer Science*, S. Goldwasser, Ed., IEEE Computer Society, Los Alamitos, CA, 124-34, 1994.

[5] D.P. DiVincenzo, "The Physical Implementation of Quantum Computation," *Fotchr Phys*, **48**, 771, 2000.

[6] D.P. DiVincenzo, "Quantum Computation," *Science*, **270**, 255, 1995.

[7] M. Bocko, A. M. Herr, and M. Feldman, "Prospects for Quantum Coherent Computation using Supeconducting Electronics," *IEEE Trans. Appl. Superconductivity*, **7**, 3638-41, 1997.

[8] Y. Makhlin, G. Schön, and A. Shnirman, "Quantum-state engineering with Josephson-junction devices," *Reviews of Modern Physics*, **73**, 357-400, 2001.

[9] R.V. Voss and R.A. Webb, "Macroscopic Quantum Tunneling in 1-μm Nb Josephson Junctions," *Phys. Rev. Lett.*, **47**, 265-8, 1981.

[10] M.H. Devoret, J.M. Martinis, and J. Clarke, "Measurements of Macroscopic Quantum Tunneling out of the Zero-Voltage State of a Current-Biased Josephson Junction," *Phys. Rev. Lett.*, **55**, 1908, 1985.

[11] J.M. Martinis, M.H. Devoret, and J. Clarke, "Energy-Level Quantization in the Zero-Voltage State of a Current-Biased Josephson Junction," *Phys. Rev. Lett.*, **55**, 1543, 1985.

[12] R. Rouse, S. Han, and J.E. Lukens, "Observation of Resonant Tunneling between Macroscopically Distinct Quantum Levels," *Phys. Rev. Lett.*, **75**, 1614-7, 1996.

[13] J.R. Friedman, V. Patel, W. Chen, S.K. Tolpygo, and J.E. Lukens, "Quantum Superposition of Distinct Macroscopic States," *Nature*, **406**, 43-6, 2000.

[14] C.H. van der Wal, A.C.J. ter Haar, F.K. Wilhelm, R.N. Schouten, C.J.P.M. Harmans, T.P. Orlando, S. Lloyd, and J.E. Mooij, "Quantum Superposition of Macroscopic Persistent-Current States," *Science*, **290**, 773-7, 2000.

[15] Y. Nakamura, Y.A. Pashkin, and J.S. Tsai, "Coherent Control of Macroscopic Quantum States in a Single-Cooper pair Box," *Nature*, **398**, 786, 1999.

[16] Y. Nakamura, Y.A. Pashkin, and J.S. Tsai, "Rabi Oscillations in a Josephson-Junction Charge Two-Level System," *Phys. Rev. Lett.*, **87**, 246601, 2001.

[17] Y. Yu, S. Han, X. Chu, S. Chu, and Z. Wang, "Coherent Temporal Oscillations of Macroscopic Quantum States in a Josephson Junction," *Science,* **296**, 889-92, 2002.

[18] D. Vion, A. Aassime, A. Cottet, P. Joyez, H. Pothier, C. Urbina, D . Esteve, and M.H. Devoret, "Manipulating the Quantum State of an Electrical Circuit," *Science*, **296**, 886-9, 2002.

[19] J. M. Martinis, S. Nam, J. Aumentado, and C. Urbina, "Rabi Oscillations in a Large Josephson-Junction Circuit," *Phys. Rev. Lett.*, **89**, 117901-1-4, 2002.

[20] I. Chiorescu, Y. Nakamura, C. J. P. M. Harmans and J. E. Mooij, "Coherent Quantum Dynamics of a Superconducting Flux Qubit," *Science*, **299**, 1869-71, 2003.

[21] A.J. Berkley, H. Xu, R.C. Ramos, M.A. Gubrud, F.W. Strauch, P.R. Johnson, J.R. Anderson, A.J. Dragt, C.J. Lobb, and F.C. Wellstood, "Entangled Macroscopic Quantum States in Two Superconducting Qubits," *Science*, **300**, 1548-50, 2003.

[22] T. Yamamoto, Y.A. Pashkin, O. Astafiev, Y. Nakamura, and J.S. Tsai, "Demonstration of Conditional Gate Operation Using Superconducting Charge Qubits," *Nature*, **425**, 941-4, 2003.

[23] K. Berggren, E. Macedo, D. Feld, and J. Sage, "Low T_c Superconductive Circuits Fabricated on 150mm-Diameter Wafers Using a Doubly Planarized Nb/AlO_x/Nb Process," *IEEE Trans. Appl. Superconductivity*, **9**, 3271-4, 1999.

[24] K.K. Likharev and V.K. Semenov, "RSFQ Logic/Memory Family: A New Josephson-Junction Technology for Sub-Terahertz-Clock Frequency Digital Systems," *IEEE Trans. Appl. Superconductivity*, **1**, 1, 1990.

[25] J.E. Mooij, T.P. Orlando, L. Levitov, L. Tian, C. van der Wal, and S. Lloyd, "Josephson Persistent-Current Qubit," *Science,* **285**, 1036-9, 1999.

[26] T.P. Orlando, J.E. Mooij, L. Tian, C.H. van der Wal, L.S. Levitov, S. Lloyd, and J.J. Mazo, "Superconducting Persistent-Current Qubit," *Phys. Rev. B,* **60**, 15398, 1999.

[27] A. Ferendeci, *Solid State and Electron Devices.* McGraw-Hill, Inc., New York, pp.363-385, 1991.

[28] S. Campbell, *The Science and Engineering of Microelectronic Fabrication.* Oxford University Press, New York, 1996.

[29] M. Gurvitch, M.A. Washington, and H.A. Huggins, "High quality Refractory Josepshon Junctions Utilizing Thin Aluminum Layers," *Appl.Phys. Lett.*, **42**, 472, 1983.

[30] M.B. Ketchen, D. Pearson, A.W. Kleinsasser, C.K. Hu, M. Smyth, J. Logan, K. Stawiasz, E. Baran, M. Jaso, T. Ross, K. Petrillo, M. Manny, S. Basavaiah, S. Brodsky, S.B. Kaplan, W.J. Gallagher, and M. Bhushan, "Submicron, Planarized, Nb/AlO_x/Nb Josephson Process for 125 mm Wafers Developed in Partnership with Si Technology," *Appl. Phy. Lett.*, **59**, 2609-11, 1991.

[31] F. Tay, *Microfluidics and BioMEMS Applications.* Kluwer Academic Publishers, Boston, 2002.

[32] W.H. Mallison, R.E. Miller, and A.W. Kleinsasser, "Effect of Growth Conditions on the Electrical Properties Nb/AlO_x/Nb Tunnel Junctions," *IEEE Trans. Appl. Superconductivity*, **5**, 2330-3, 1995.

[33] K. Kuroda and M. Yuda, "Niobium Stress Influence on Nb/AlO_x/Nb Josephson Junctions," *J. Appl. Phys.*, **63**, 2352-7, 1988.

[34] I. Brodie and J.J. Murray, *The Physics of Micro/Nano-Fabrication.* Plenum Press, New York, 1992.

[35] Photronics Inc., 1061 East Indiantown Road, Jupiter, Florida 33477.

[36] H.I. Smith, *Lecture Notes 6.781 Submicron and Nanometer Structures Technology.* MIT Dept. of Electrical Engineering.

[37] J.L. Vossen and W. Kern, *Thin Film Processes II.* Academic Press Inc., Massachusetts, 251-5, 1991.

[38] X. Meng, L. Zheng, A. Wong, and T. Van Duzer, "Micron and Submicron Nb/Al-AlO_x/Nb Tunnel Junctions with High Critical Current Densities," *IEEE Trans. Appl. Superconductivity*, **11**, 365-8, 2001.

[39] X. Meng, A. Bhat, and T. Van Duzer, "Very Small Critical Current Spreads in Nb/Al-AlO_x/Nb Integrated Circuits Using Low-Temperature and Low-Stress ECR PECVD Silicon Oxide Films," *IEEE Trans. Appl. Superconductivity*, **9**, 3208-11, 1999.

[40] H. Kroger, L.N. Smith, and D.W. Jillie, "Selective Niobium Anodization Process for Fabricating Josephson Tunnel Junctions," *Appl. Phys. Lett.*, **39**, 280-2, 1981.

[41] M. Bhushan, M.B. Ketchen, C.K. Hu, "Nb-AlO_x-Nb SNAP Technology for 125 mm Wafers Developed in Partnership with Silicon Technology," *Superconductive Devices and Their Applications*. 265-70. Springer-Verlag. New York 1992.

[42] M. Bhushan and E.M. Macedo, "Nb/AlO_x/Nb Trilayer Process for the Fabrication of Submicron Josephson Junctions and Low Noise dc SQUIDs," *Appl. Phys. Lett.*, **58**, 1323-5, 1991.

[43] T. Imamura and S. Hasuo, "Characterization of Nb/AlO_x-Al/Nb Junction Structures By Anodization Spectroscopy," *IEEE Trans. Magn.*, **25**, 1131-4, 1989.

[44] Microelectronics Center of North Carolina, P.O. Box 13910, 3021 Cornwallis Road, Research Triangle Park, NC 27709-3910.

[45] J.E. Sauvageau, C.J. Burroughs, P.A.A. Booi, M.W. Cromar, S.P. Benz, and J.A. Koch, "Superconducting Integrated Circuit Fabrication With Low Temperature ECR-Based PECVD SiO_2 Dielectric Films," *IEEE Trans. Appl. Superconductivity*, **5**, 2303-9, 1995.

[46] Z.Bao, M. Bhushan, S. Han, and J.E. Lukens, "Fabrication of High Quality, Deep-Submicron Nb/AlO_x/Nb Josephson Junctions Using Chemical Mechanical Polishing," *IEEE Trans. Appl. Superconductivity*, **5**, 2731-4, 1995.

[47] Measurements of Ti/Pt resistors, made in the MIT Lincoln Laboratory process, have been performed by N. Markovic at $T \simeq 10\,mK$ and were shown to have resistivity $\sim 0.6\Omega/SQ$.

[48] K. Berggren, E. Macedo, D.A. Feld, and J.P. Sage, "Model of Resistor Fabrication in a Low Temperature Superconductive Electronics Process", *Lincoln Laboratory Solid State Research Quarterly Technical Report*, **4**, 35-40, 1997.

[49] K.K. Berggren, M. O'Hara, J.P. Sage, and A.H. Worsham, "Evaluation of critical current density of Nb/Al/AlO_x/Nb Josephson Junctions Using Test Structures at 300 K," *IEEE Trans. Appl. Supercond.*, **9**, 3236-9, 1999.

[50] H. Nakagawa, G. Pepe, H. Akoh, L. Frunzio, R. Cristiano, E. Esposito, S. Pagano, G. Peluso, A. Barone, and S. Takada, "A New Fabrication Process of Superconducting Nb Tunnel Junctions with Ultralow Leakage Current for X-Ray Detection," *Jpn. J. Appl. Phys.*, **32**, 4535-7, 1993.

[51] S. Morohashi and S. Hasuo, "Experimental investigations and analysis for high-quality Nb/Al-AlO_x/Nb Josephson junctions," *J. Appl. Phys.*, **61**, 4835-49, 1987.

[52] D. Nakada, K.K. Berggren, E. Macedo, V. Liberman, and T.P. Orlando, "Improved Critical-Current-Density Uniformity by Using Anodization," *IEEE Trans. Appl. Superconductivity*, **13**, 111-4, 2003.

[53] T.P. Orlando and K.A. Delin, *Foundations of Applied Superconductivity.* Addison-Wesley Co., Massachusetts, 1991.

[54] R.P Feynman, *The Feynman Lectures on Physics.* Addison-Wesley Publishing Co., Massachusetts, 1965.

[55] J.H. Hinken, *Superconductor Electronics: Fundamentals and Microwave Applications.* Springer-Verlag, Berlin, 1988.

[56] A.M. Kadin, *Introduction to Superconducting Circuits.* John-Wiley and Sons Inc., New York, 1999.

[57] S.T. Ruggiero, D.A. Rudman, *Superconducting Devices.* Academic Press. Inc., New York, 1990.

[58] T. van Duzer, C.W. Turner, *Superconductive Devices and Circuits 2nd edition.* Prentice Hall, Inc., New Jersey, 1999.

[59] T.A. Fulton, L.N. Dunkelberger, "Lifetime of the Zer-Voltage State in Josephson Tunnel Junctions," *Phys. Rev. B.*, **9**, 4760-7, 1974.

[60] M.H. Devoret, *Les Houches Session LXIII : Quantum Fluctuations.* Elsevier., New York, 1997.

[61] M. Tinkham, *Introduction to Superconductivity.* McGraw-Hill Co. Inc., New York, 1996.

[62] H. Grabert and M.H. Devoret, *Single Charge Tunneling.* Plenum Press., New York, 1992.

[63] D.S. Crankshaw, and T.P. Orlando, "Inductance Effects in the Persistent-Current Qubit," *IEEE Trans. Appl. Superconductivity*, **11**, 1006, 2001.

[64] C. van der Wal, *Quantum Superpositions of Persistent Josephson Currents*, Doctoral Thesis, Delft University of Technology, 2001.

[65] G. Blatter, "Scrodinger's Cat is Now Fat," *Nature*, **406**, 25-6, 2000.

[66] A. J. Leggett, S. Chakravarty, A.T. Dorsey, M.P.A. Fisher, A. Garg, and W. Zwerger, "Dynamics of the Dissipative Two-State System," *Rev. Mod. Phys.*, **59**, 1, 1987.

[67] L. Tian, *A Superconducting Flux Qubit: Measurement, Noise, and Control*, Doctoral Thesis, Massachusetts Institute of Technology, 2002.

[68] L. Tian, S. Lloyd, and T.P. Orlando, "Decoherence and Relaxation of a Superconducting Quantum Bit During Measurement," *Phys. Rev. B*, **65**, 144516, 2002.

[69] T.P. Orlando, L. Tian, , D.S. Crankshaw, S. Lloyd, C.H. van der Wal, J.E. Mooij, and F. Wilhelm, "Engineering the Quantum Measurement Process for the Persistent-Current Qubit," *Physica C,* **368**, 294-9, 2002.

[70] S. Han, Y. Yu, X. Chu, S. Chu, and Z. Wang, "Time-Resolved Measurement of Dissipation-Induced Decoherence in a Josephson Junction," *Science,* **293**, 1457, 2001.

[71] C. Cosmelli, P. Carelli, M. G. Castellano, F. Chiarello, G. D. Palazzi, R. Leoni, and G. Torrioli, "Measurement of the Intrinsic Dissipation of a Macroscopic System in the Quantum Regime," *Phys. Rev. Lett.*, **82**, 5357, 1999.

[72] S. Han and R. Rouse, "Comment on 'Measurement of the Intrinsic Dissipation of a Macroscopic System in the Quantum Regime'," *Phys. Rev. Lett.*, **86**, 4191, 2001.

[73] Y. Yu, D. Nakada, J.C. Lee, B. Singh, D.S. Crankshaw, K.K. Berggren, T.P. Orlando, W.D. Oliver, "Energy Relaxation Time between Macroscopic Quantum Levels in a Superconducting Persistent-Current Qubit", *Phys. Rev. Lett.*, **92**, 117904, 2004.

[74] K. Segall, D.S. Crankshaw, D. Nakada, B. Singh, J. Lee, T.P. Orlando, K.K. Berggren, N. Markovic, S.O. Valenzuela, and M. Tinkham, "Experimental Characterization of the Two Current States in a Nb Persistent-Current Qubit," *IEEE Transactions On Applied Superconductivity*, **13**, 1009-12, 2003.

[75] K. Segall, D.S. Crankshaw, D. Nakada, T.P. Orlando, L.S. Levitov, S. Lloyd, M. Tinkham, N. Markovic, S. Valenzuela, and K.K. Berggren, "Impact of Time-Ordered Measurements of the Two States in a Niobium Superconducting Qubit Structure," *Phys. Rev. B Rapid Communications*, **67**, 220506-1-4, 2003.

[76] D.S. Crankshaw, K. Segall, D. Nakada, T.P. Orlando, L.S. Levitov, S. Lloyd, S. Valenzuela, N. Markovic, M. Tinkham, and K.K. Berggren, "DC Measurements

of Macroscopic Quantum Levels in a Superconducting Qubit Structure with a Time-Ordered Meter," *Phys. Rev. B*, **69**, 144518, 2004.

[77] D.S. Crankshaw, *Measurement and On-chip Control of a Niobium Persistent Current Qubit*, Doctoral Thesis, Massachusetts Institute of Technology, May 2003.

[78] D.V. Averin, J.R. Friedman, and J.E. Lukens, "Macroscopic Resonant Tunnelling of Magnetic Flux," *Phys. Rev. B*, **62**, 11802, 2000.

[79] M. Kamon, M.J. Tsuk, and J. White, "FASTHENRY: A Multipole-Accelerated 3-D Inductance Extraction Program," *IEEE Trans. on Microwave Theory and Tech.*, 1994.

[80] J. M. Schmidt, A. N. Cleland, and J. Clarke, "Resonant Tunneling in Small Current-Biased Josephson Junctions," *Phys. Rev. B*, **43**, 229, 1991.

[81] W. Bialek, S. Chakravarty, and S. Kivelson, "Tunneling spectroscopy of a macroscopic variable," *Phys. Rev. B*, **35**, 120, 1987.

[82] P. Silvestrini, S. Pagano, R. Cristiano, O. Liengme, and K.E. Gray, "Effect of Dissipation on Thermal Activation in an Underdamped Josephson Junction: First Evidence of a Transition between Different Damping Regimes," *Phys. Rev. Lett.*, **60**, 844, 1988.

[83] W. H. Zurek, "Decoherence and the Transition from Quantum to Classical," *Phys. Today*, **44**, 36, 1991.

[84] K.C. Gupta, R. Garg, I.J. Bahl. *Microstrip Lines and Slotlines.* Artech House Inc., Massachusetts, pp.257-301, 1979.

[85] J.A. Kong, *Electromagnetic Wave Theory.* EMW Publishing, Massachusetts, 1999.